KOBELCO TECHNOLOGY REVIEW

No. 30 DEC. 2011

Feature-Ⅰ: Material Processing Technologies
Feature-Ⅱ: Steel Wire Rod and Bar
Feature-Ⅲ: Steel Plate and Sheet

Contents

Feature-Ⅰ Material Processing Technologies

Feature-Ⅱ Steel Wire Rod and Bar

Feature-Ⅲ Steel Plate and Sheet

Published by

Secretariat & Publicity Dept.
Kobe Steel, Ltd.

10-26, Wakinohamacho 2-chome, Chuo-ku, Kobe, HYOGO 651-8585, JAPAN
http://www.kobelco.co.jp

Editorial Office: **Shinko Research Co., Ltd.**
5-5, Takatsukadai 1-chome,
Nishi-ku, Kobe, HYOGO 651-2271, JAPAN
Fax: +81-78-992-9790
E-mail: rd-office@kobelco.com

High-quality Work Roll Manufacturing Technology Using New Electro Slag Remelting (ESR)

Jun SATO[*1], Kouji IWANAGA[*1], Atsushi TOMIOKA[*1], Katsushige NISHIGUCHI[*1], Hiroki NAKASHIMA[*2], Hitoshi ISHIDA[*3]
[*1] Steel Making & Casting Department, Steel Casting & Forging Plant, Steel Casting & Forging Division, Iron & Steel Business, [*2] Technical Development Department, Steel Casting & Forging Division, Iron & Steel Business, [*3] Materials Research Laboratory, Technical Development Group

Because cold rolling requires work rolls of high quality in their surfaces and interiors, the rolls are generally made from electro-slag-remelting (ESR) ingots which ensure a stable outcome. In order to produce rolls with excellent dendrite pattern, a fine and uniform dendrite structure with no flow pattern is required. Segregation lines, which may appear as "freckles" on the roll surface, are sometimes generated in the ingots. Such segregation lines should not exist within the use depth of the rolls. In recent years, Kobe Steel has upgraded its ESR apparatus and achieved a significant improvement in the quality of the surface and interior.

Introduction

Work rolls are used for cold-rolling steel plates into thin sheets and have to meet demanding standards for their surface and interior quality. Thus, they are typically made from steel ingots produced by electro slag re-melting (ESR), ingots which can consistently provide the desired quality. To ensure high resistance to surface deterioration, the surfaces must have fine and homogeneous dendrite structures without flow patterns. Some ingots may have internal segregation lines, which can appear as "freckles" on their surfaces, depending on the type of steel. Such segregation lines must not exist in the effective use depth of the rolls. To meet such demanding quality requirements, Kobe Steel renewed its ESR apparatus in 2007 and has significantly improved the surface and interior qualities, as reported in this paper.

1. Method for making work rolls for cold rolling and characteristics required for rolls

The work rolls for cold rolling (hereinafter simply referred to as "work rolls") are made according to the following steps:

Melting by electric furnace (EF) → Refining in ladle furnace (LF) → Bottom teeming & Ingot making → ESR → Forging & Heat treatment → Machining

ESR is a type of re-melting technique which involves a target metal used as a consumable electrode, and a water-cooled mould holding a layer of molten slag, in which the slag layer conducts a large electric current and generates resistance heat to melt the electrode. The droplet of molten steel passes through the slag layer and sequentially solidifies into a steel ingot. The steel ingot thus obtained has a superior cleanliness and is used for high-value-added products such as work rolls and aircraft members.

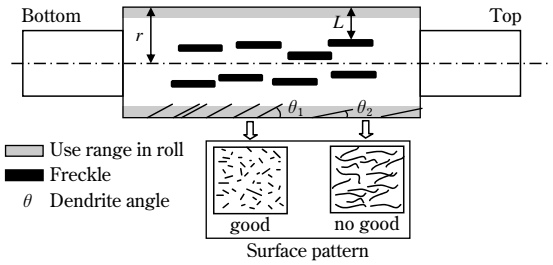

Fig. 1 Necessary quality for roll material

The quality of work rolls is largely affected by the quality of the steel ingots made by the ESR process. Here, the dendrite structure of the ingot surface must be fine and homogeneous, and, to prevent freckles, there should be no positive segregation of the additives in the steel within the use range (depth). Depending on the intended applications, the rolls have differing quality requirements. Tinplate roll for beverage cans especially requires fine and homogeneous dendrite structures on the rolls' surfaces. In addition to the stringent quality requirement for the surface, some such rolls are reworked for reclamation after use and must be free from freckles even after twice as deep a layer is removed from the surface, compared with other types of rolls.

In order to refine the structure of surface dendrite, a large enough angle must be retained between the mould wall and the dendrite growth direction in a steel ingot (the angle hereinafter referred to as "dendrite angle"). This dendrite angle enables the evaluation of the surface structure of rolls. The present paper uses dendrite angle θ as the evaluation index of the surface quality and depth of the freckled region (hereinafter referred to as freckled depth, L/r (L; the distance between the ingot circumference and the depth where freckles appear: r; steel ingot radius) as the evaluation indices of interior quality (**Fig. 1**). The following describes the improvement of these indices.

2. Relationship between dendrite angle and freckled depth

Dendrites grow vertically from the solidification interface in the pool of molten steel[1), 2)]. Thus, in order

to increase the dendrite angle, the lateral face of the molten steel pool must be kept parallel to the mould surface as much as possible. In general, the higher the melting rate, the deeper the molten steel pool becomes, which increases the dendrite angle. Freckles, on the other hand, are caused by condensed molten steel floating up and being trapped in the solidified layer. Thus, the shallower the molten steel pool, the less likely they are to appear [3), 4)]. To maintain the pool of molten steel shallow enough, the melting rate must be kept low. In other words, there is a trade-off relationship between the dendrite angle and freckled depth: i.e., a higher melting rate results in a larger dendrite angle θ and shallower L/r, and vice versa (**Fig. 2**). **Fig. 3** shows the relationship between the dendrite angle θ and freckled depth (L/r). Here, the dendrite angle is defined by the average of the angles measured at the depth of 30mm from the steel ingot surface (assuming that the measured points will lie on the outer surface at the time of shipment) and the angle measured at the depth of 90mm (assuming that the points will lie on the outer surface at the time of disposal). This figure also indicates that controlling the melting rate alone cannot improve the dendrite angle and freckled depth at a time.

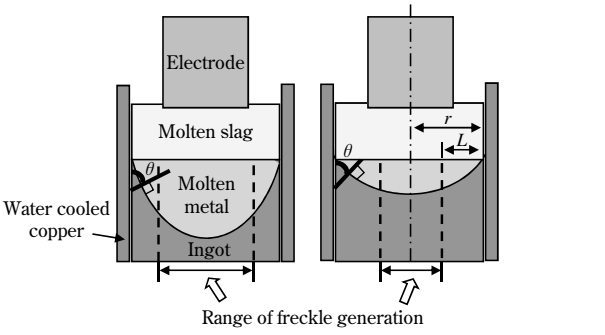

Melting rate	High	Low
Molten metal depth	Deep	Shallow
Dendrite angle (θ)	Big(good)	Small(no good)
Depth of freckled region (L/r)	Small(no good)	Big(good)

Fig. 2 Relationship between melting rate, molten metal depth, dendrite angle (θ), and depth of freckled region (L/r)

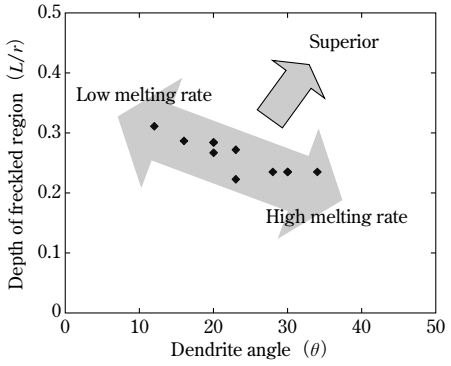

Fig. 3 Relationship between dedrite angle and depth of freckled region (L/r)

3. Decreasing thickness of slag skin

In addition to the melting rate, various other melting conditions can affect the quality of steel ingots made by ESR; e.g., flux composition, the amount of flux, electric current, voltage, cooling capacity of the mould and fill ratio. Aiming at improving both the dendrite angle and freckled depth simultaneously, Kobe Steel focused on the heat transfer of the slag skin formed between the ingot and water-cooled copper mould. A method was devised for thinning the slag skin to increase the cooling rate of the steel ingot and for making the lateral face of the pool of molten steel almost parallel to the mould surface to decrease the overall depth of the pool (**Fig. 4**).

The thickness of the slag skin is largely affected by the slag composition and immersion volume of the electrode. Thus, for thinning the slag skin, it is effective to use flux with a low melting point and/or to decrease the immersion volume of the electrode. Such a flux can be found in a CaO-Al_2O_3-CaF_2 series with high CaF_2 content. However, when used in an insulated system in which the mould and steel ingot are insulated from each other, the flux can result in arcing caused by the potential difference between the mould and steel ingot. Thus such flux cannot be used for the conventional apparatus. To enable the use of flux with such a low melting-point, the mould and steel ingot must have the same electrical potential (**Fig. 5**). The new ESR adopts a live mould which allows electrical conduction and enables the use of flux with a low melting point (1,290℃).

Immersing a large volume of electrode into the slag layer increases the amount of heat extracted by the electrode, which lowers the temperature of the slag layer and increases the thickness of the slag skin. Thus it is preferable to keep the immersion volume of

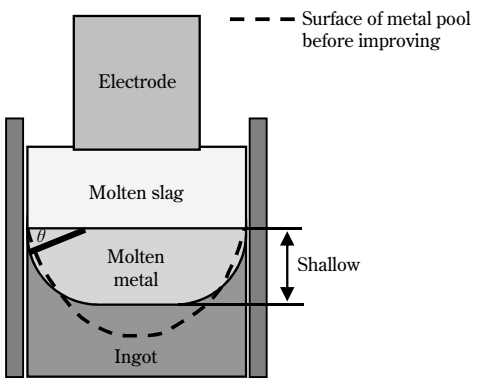

Fig. 4 Ideal shape of molten metal

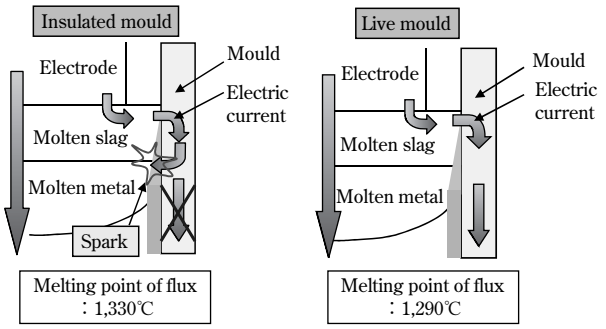

Fig. 5 Pattern diagrams of insulated mould and live mould in ESR melting

the electrode as small as possible. This was difficult to achieve in the conventional apparatus, in which the electrode was suspended by a wire with poor responsivity, making it difficult to precisely control the electrode position. In addition, the conventional electrode positioning system, involving voltage swing, suffered from difficulties caused by slag composition, electrical conductivity and slag volume, all of which change during the process. In addition, the changing lengths of electrode and ingot accompany changes in the impedance and voltage, causing difficulties. To avoid this, a resistance swing method was employed for the new electrode positioning (**Table 1**). **Fig. 6** summarizes these and other features of the ESR apparatus before and after the renewal.

Table 1 Electrode positoning control

	Conventional ESR	New ESR
Electrode positioning control	Voltage swing	Resistance swing
Electrode positioned by	Winch hoisting	Ball screw
Amount of immersion	10mm	1～3mm

4. Quality of steel ingots produced by new ESR

The following evaluates the quality of steel ingots produced by conventional and new ESR apparatuses and discusses the optimum operating conditions.

4.1 Experimental method

A steel ingot having an extra portion 500mm in length at the top was prepared by the new ESR. Specimens, as shown in **Fig. 7**, were prepared for macroscopic observation: i) a $\phi 810 \times 30$mm transverse cross-section specimen; and ii) a $810 \times 470 \times 30$mm longitudinal section specimen.

Among the segregation spots observed on the transverse cross-section specimen, spots having average diameters greater than 2mm were determined to be freckles, and their locations were recorded. The angles of dendrite growth directions were determined on the longitudinal section.

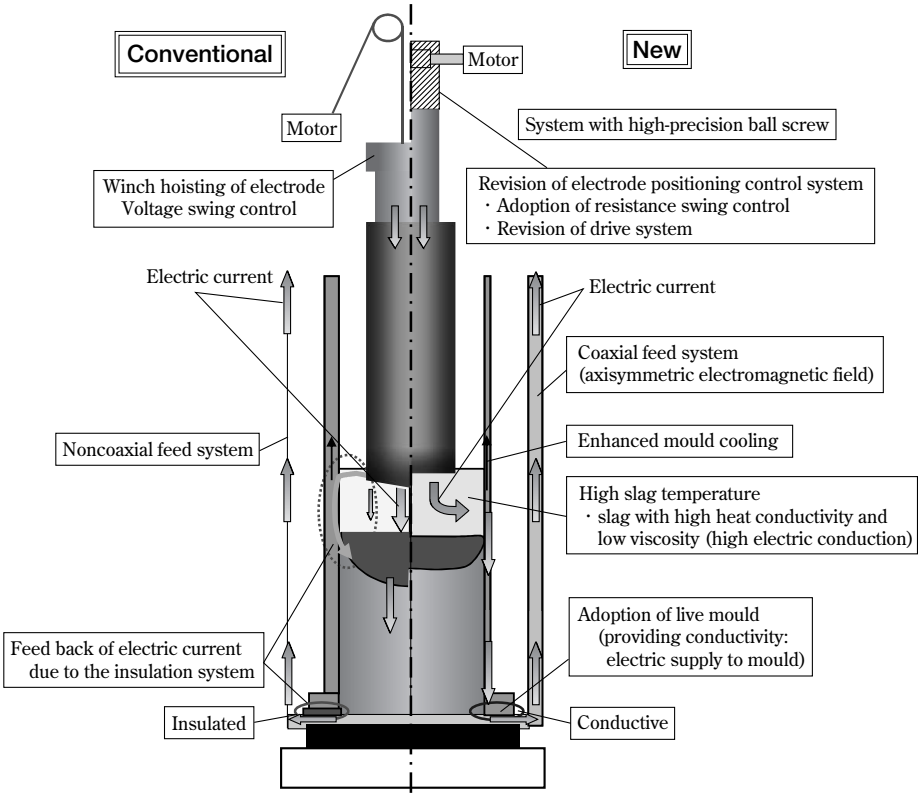

Fig. 6 Features of conventional and new ESR

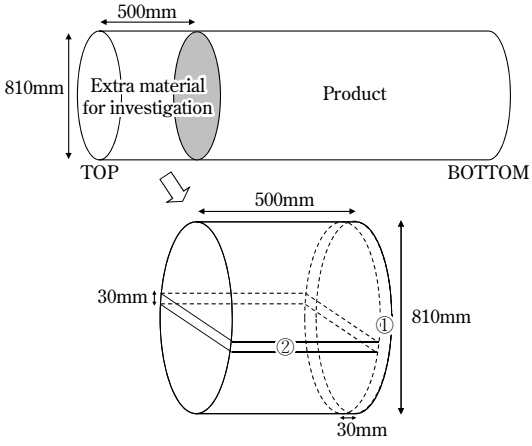

Fig. 7 Specimens for investigation of ESR

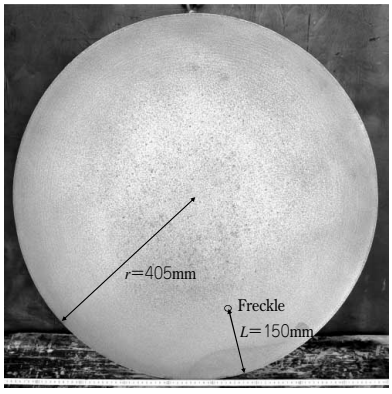

Fig. 8 Photograph of typical cross-sectional macro structure 〔Freckled region:150mm deep from the surface (L/r=0.370)〕

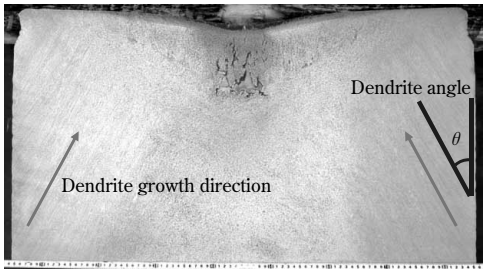

Fig. 9 Photograph of typical longitudinal sectional macro structure

4.2 Results

Fig. 8 and **9** show typical macroscopic structures observed on transverse and longitudinal cross-sections, respectively. **Fig.10** shows the relationships between the dendrite angle and freckled depth in the ingots prepared by the new and conventional ESR apparatuses, respectively. It should be noted that the new system has improved both the dendrite angle and freckle depth significantly compared with the conventional system.

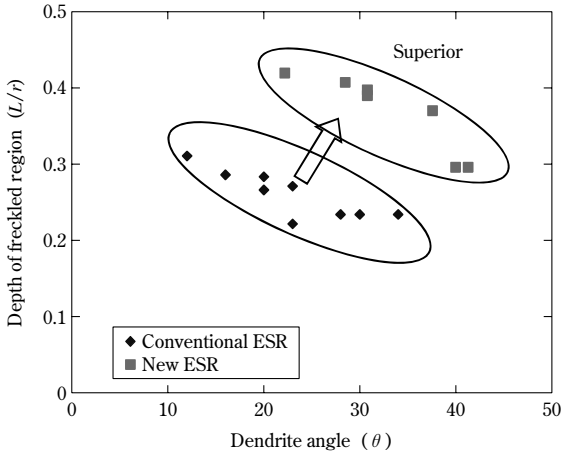

Fig.10 Relationship between dendrite angle (θ) and depth of freckled region (L/r) in the ingot produced by New ESR

5. Theoretical verification of improvement in internal quality of steel ingots

The present modification of the ESR apparatus has changed the conventional casting conditions, such as control method, slag composition, slag temperature, molten steel temperature, slag skin thickness and mould structure. Thus it is envisaged that the solidification profile has also been changed. To theoretically verify the quality improvement of the steel ingot achieved thanks to this modification, a numerical analysis (heat-transfer calculation) was conducted to determine the shape of the molten steel pool (i.e., dendrite angle). The calculation result was compared to the results for the steel ingot quality described in section 4.

An FEM program for solidification analysis, "Casting Analysis System" (CASTEM), developed by Kobe Steel[5], was used for calculating the advancement of the solidification interface and the shape of the molten steel pool in the ESR. The CASTEM allows resolving thermal conduction equations in non-steady state, taking into account the release of latent heat during solidification, as follows:

$$\rho C\frac{\partial T}{\partial t}-\rho L\frac{\partial f_s}{\partial t}=\frac{\partial}{\partial x}\left(\lambda\frac{\partial T}{\partial x}\right)+\frac{\partial}{\partial y}\left(\lambda\frac{\partial T}{\partial y}\right)+\frac{\partial}{\partial z}\left(\lambda\frac{\partial T}{\partial z}\right)$$

wherein T represents temperature, t represents time, C represents specific heat, ρ represents density, L represents latent heat, f_s represents solid phase ratio and λ represents thermal conductivity.

Table 2 shows the physical properties used for the heat-transfer analysis. The melting rates were set to three conditions, i.e., 600kg/h, 700kg/h and 920kg/h. Since there is no measurement data for the melt temperature T (℃) at the surface of the molten steel pool, the melt temperature was calculated according to Formula (1). A slag temperature measured for a different type of steel produced by the

Table 2 Physical properties and experimental conditions used in heat transfer analysis

Liquid steel physical properties	Liquidus temperature	1,450℃		
	Solidus temperature	1,344℃		
	Heat conductivity	3.8×10^{-2}cal/(mm²·s·℃)		
	Specific heat	0.17cal/g/K		
	Density	7.6×10^{-3}g/mm³		
	Latent heat of solidification	65cal/g		
Coefficient of heat transfer	Ingot bottom	1.4×10^{-3}cal/(mm²·s·℃)		
	Ingot side surface	2.7×10^{-4}cal/(mm²·s·℃)		
Melting speed		600kg/h	700kg/h	920kg/h
Molten metal temperature		1,604℃+α	1,628℃+α	1,681℃+α

conventional ESR was used for the calculation. Here, α represents a fitting parameter.

$$T\,(℃) = 0.24 \times (\text{melting rate kg/h}) + 1460 + \alpha \cdots (1)$$

The overall heat transfer coefficient h between the lateral face of the steel ingot and the water-cooled copper mould was calculated using Formula (2) below.

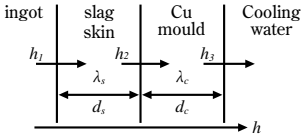

$$\frac{1}{h}=\frac{1}{h_1}+\frac{1}{\lambda_s/d_s}+\frac{1}{h_2}+\frac{1}{\lambda_c/d_c}+\frac{1}{h_3} \cdots\cdots\cdots\cdots (2)$$

Fig.11 shows the relationship between the slag skin thickness and overall heat transfer coefficient calculated under the above conditions. It appears that the slag skin thickness for the conventional ESR is approximately 3mm, while that for the new ESR is approximately 1mm, and the overall heat transfer coefficient is considered to have increased by approximately 2.5 times (**Table 3**).

Fig.12 shows examples of the metal pool shapes calculated. The calculation is based on a two dimensional axial symmetry model with the left side representing the ingot center and the right side representing the ingot surface. Each diagram includes metal pool shapes, which are determined by the temperature profiles of liquidus line and solidus line at given times.

Dendrite growth directions were calculated at the depth positions of 30mm and 90mm from the ingot surface, in the direction vertical to the molten metal pool determined by the profiles of the liquidus line. Dendrite angles are defined by the crossing angles between the dendrite growth directions and the ingot surface. The dendrite angles were determined by the average of angles obtained from the depth positions of 30mm and 90mm.

Fig.13 compares the calculated and measured

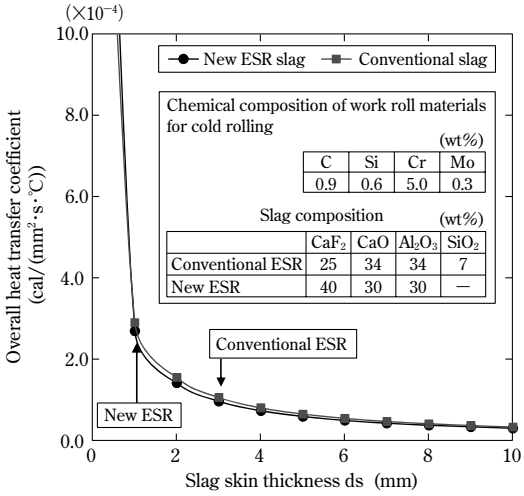

Fig.11 Slag skin thickness and overall heat transfer coefficient

Table 3 Slag skin thickness and overall heat transfer coefficient

	Slag skin thickness (mm)	Overall heat transfer coefficient ($\times10^{-4}$cal/(mm²·s·℃))
Conventional ESR	3	1.05
New ESR	1	2.68

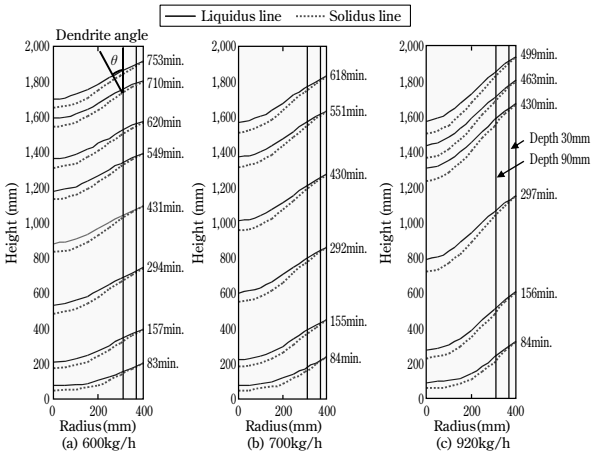

Fig.12 Metal pool shapes at each melting speed (α=50℃)

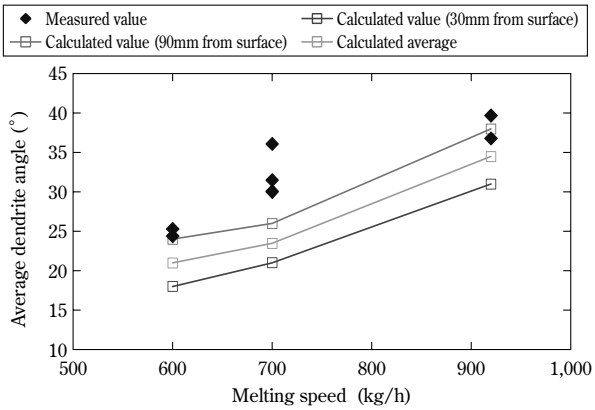

Fig.13 Calculated (Molten metal temperature α=0℃) and measured values of average dendrite angle

values of average dendrite angles. The figure indicates the difference between the calculated and measured values. It should be noted that the values in Fig.13 were calculated using the slag temperature measured for the conventional apparatus. The new apparatus is thought to have achieved a higher slag layer temperature (= molten metal temperature) as a result of the present renewal including the modification of electrode positioning control (employing a resistance swing control and a new electrode drive method), which decreased the immersion volume of the electrode.

Thus, the fitting parameter α in Formula (1) was set to 0℃, 50℃ and 100℃ to determine the molten metal temperature T (℃) at the pool surface for each condition. The dendrite angles were averaged for each condition and were compared to measured values as shown in **Fig.14** and **15** respectively.

The comparison with measured values indicates that, by setting α to a value in the range from 50~100℃, the calculated values for dendrite angles turn out to agree well with the measured values.

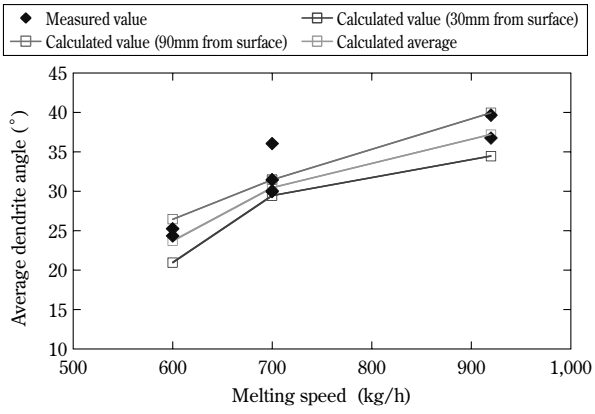

Fig.14 Calculated (Molten metal temperature α=50℃) and measured values of average dendrite angle

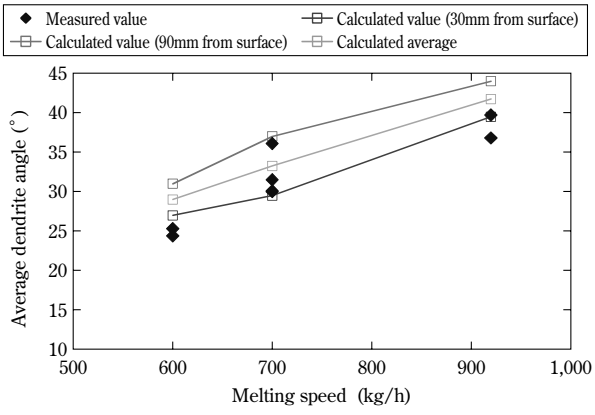

Fig.15 Calculated (Molten metal temperature α=100℃) and measured values of average dendrite angle

The above discussion indicates that the new ESR apparatus maintains the slag temperature 50~100℃ higher than the conventional apparatus. This produces a slag skin 1mm thick, which is less than the slag skin thickness of 3mm produced by the conventional apparatus. The thinner slag skin increases the cooling rate at the lateral face of the ingot, which improves the shape of the molten steel pool (Figure 4) and produces a steel ingot with a large dendrite angle and fewer freckle defects.

6. Summary

An ESR apparatus was renewed so as to produce high-quality rolls. The new apparatus was subjected to a study of the relationship between the melting conditions and the quality of the steel ingot interior. The following results were obtained:

(1) Significant improvements were obtained for the dendrite angle and depth of the freckled region in the new ESR, compared with the conventional one;
(2) the new ESR yielded a thinner slag skin of 1mm, as against the 3mm thick slag skin in the conventional ESR, and increased the overall coefficient of heat conduction by approximately 2.5 times; and
(3) the results of the studies on the quality of the ingot interior and solidification analysis indicate that the new ESR increased the slag temperature by 50~100℃, compared with the conventional ESR. It is contemplated that the higher slag temperature has enabled the thinning of the slag skin.

Conclusions

The quality evaluation and its results on the roll material produced by a new ESR apparatus have been outlined. The new apparatus further comprises an automatic melt control system which decreases the operator dependence of the outcome, enabling consistent production of high quality roll materials.

References

1) A. Suzuki et al., *Physical Chemistry of Electro Slag Remelting and Its Technical Issues* (1979), pp.132-133.
2) A. Masui et al., *Physical Chemistry of Electro Slag Remelting and Its Technical Issues*, pp.149-151.
3) H. Yamada et al., *Tetsu-to-Hagane*, No. 1 (1989), pp.97-104.
4) H. Yamada et al., *Tetsu-to-Hagane*, No. 1 (1989), pp.105-112.
5) T. So et al., *R&D KOBE STEEL ENGINEERING REPORTS*, Vol. 37, No. 4 (1987), pp.99-100.

Predicting Effect of Cold Rolling on Fatigue Strength under Combined Loading

Mariko MATSUDA[*1], Eiji OOTSUKI[*2], Shuhei KAJIHARA[*3], Yoji HANAWA[*4], Takeshi HAMADA[*5]
[*1] Technical Development Department, Steel Casting & Forging Division, Iron & Steel Business
[*2] Forging Department, Steel Casting & Forging Plant, Steel Casting & Forging Division, Iron & Steel Business
[*3] Mitsui Engineering & Shipbuilding Co., Ltd.
[*4] Mechanical Engineering Research Laboratory, Technical Development Group
[*5] Mechanical Engineering Research Laboratory, Technical Development Group (currently with KOBELCO CRANES CO., LTD.)

The cold rolling method is adopted to improve the fatigue strength of crankpin fillet for marine diesel engines. Under working conditions, combined bending and torsional loading occurs in crankpin fillet; therefore, combined axial and torsional fatigue tests under tensile or compressive mean stress were conducted to distinguish among the three methods of fatigue strength evaluation. Modified IACS and Findley criteria were confirmed to be methods that are on the safe side. By evaluating fatigue strength by these criteria, it was confirmed that compressive residual stresses from the cold rolling method improve fatigue strength on the pin fillet surface of semi-built crankshafts under working conditions.

Introduction

Kobe Steel manufactures crankshafts for vessel diesel engines as one of the company's flagship products. In crankshafts, the fillets are subjected to maximum stress. Aiming at improving the fatigue strength of these parts, Kobe Steel developed a cold rolling technique. Not involving heating, this technique does not cause thermal deformation and is superior in dimensional accuracy and productivity. It was first adopted for a semi-built-up crankshaft made of cast steel in 1970 and has been adopted for some solid crankshafts since 1995. Nowadays, this technique has become one of the technologies making this company stand out among others.

Cold rolling is a method for improving the fatigue strength of the fillets by the combined effect of increased hardness caused by work hardening and compressive residual stress applied by cold rolling. Because hardness correlates well with fatigue strength, the effect of hardness increase can be predicted with relative ease. On the other hand, the effect of the compressive residual stress depends on the stress conditions of the fillets. The crankpin fillets are under a combined load of bending and torsion. Thus, in order to precisely evaluate the effect that the compressive residual stress applied by cold rolling has on the improvement of the fatigue strength, a new evaluation method must be developed, taking the combined loading into consideration.

The purpose of the present study is to make predictable the improvement in fatigue strength that is an effect of the compressive residual stress applied by cold rolling. Fatigue tests were conducted under combined load conditions with mean stress. Three methodologies were selected from among the various conventional approaches that have been proposed for evaluating fatigue strength under combined loading. The three methodologies were evaluated for their validity. Furthermore, a new method for evaluating fatigue strength under combined load was adopted for the pin fillet of a semi-built-up crankshaft made of cast steel solely to estimate the effect of the compressive residual stress, applied by cold rolling, on fatigue strength.

1. Summary of conventional results

1.1 Evaluation by small-scale cold rolling test [1)]

Fig. 1 depicts a small-scale cold-rolling test. Each specimen is made of a steel, "Throw Grade 3", which is one of the typical cast steel materials Kobe Steel uses for semi-built-up crankshafts. **Table 1** shows the chemical composition and **Table 2** shows the mechanical properties of the steel. A U-notched portion is provided on the ϕ10mm specimen, and cold rolling was applied to the notched portion. The cold-rolled specimen was subjected to a rotary bending fatigue test. The results are shown in **Fig. 2**. In this figure, the horizontal axis represents "mean stress," while the vertical axis represents "fatigue strength."

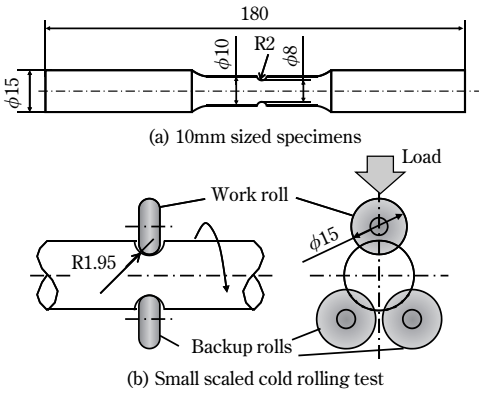

Fig. 1 Outline of small scaled cold rolling test using ϕ10mm sized specimens

Table 1 Chemical composition of "Throw Grade3"

	C%	Si%	Mn%	Cr%	Mo%	Ni%	V%
Spec. "Throw Grade3"	0.25*	0.35*	1.0*	≤ 0.50	≤ 0.30	≤ 0.50	0.08*

*nominal

Table 2 Material property of "Throw Grade3"

Specimen	Tensile strength (MPa)	Yield point (MPa)	Elongation (%)	Reduction of area (%)
Spec. "Throw Grade3"	≧530	≧310	≧20	≧45

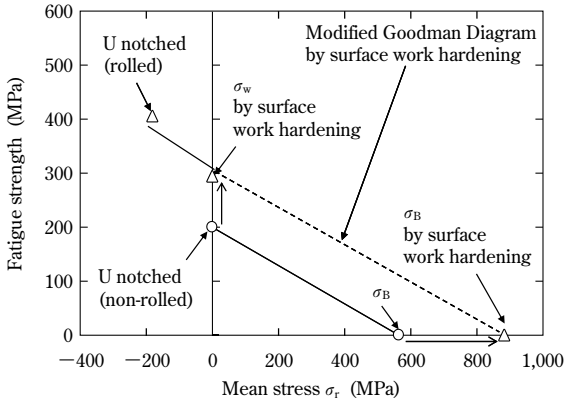

Fig. 2 Effects of surface work hardening and residual stress on fatigue strength of ϕ 10mm sized specimens after cold rolling

Also included in the figure is a Modified Goodman Diagram based on the fatigue strength, σ_w, and tensile strength, σ_B, which reflects an increase in hardness. The result indicates that, by regarding the compressive residual stress as the mean stress, the fatigue strength of the cold rolled specimen matches well with the Modified Goodman Diagram that accounts for the increase in hardness. It is concluded from the above that the main factors improving the fatigue strength of the steel, "Throw Grade 3", after cold rolling, are an increase in hardness caused by work hardening and compressive residual stress applied by cold rolling. It should also be noted that the compressive residual stress can be regarded as the mean stress.

1.2 Residual stress distribution in actual crankshafts [2)]

Kobe Steel produces large semi-built-up crankshafts, including K98MC with a cylinder diameter of 980mm. A real-scale throw was prepared using Throw Grade 3 steel, and residual stress was measured after cold rolling. **Fig. 3** depicts the K98MC throw. The measurement points for residual stress are shown in **Fig. 4** and the measurement results are shown in **Fig. 5**. As shown in Fig. 5, a compressive residual stress of about 400MPa is applied on the pin fillet surface in both the radial and circumferential directions.

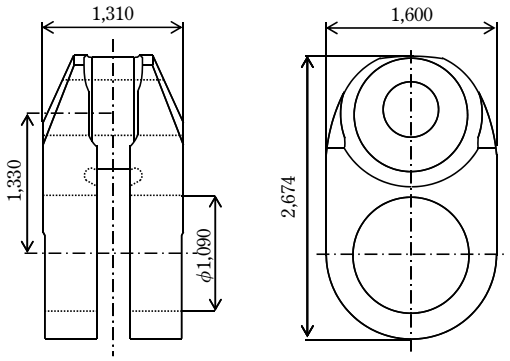

Fig. 3 Dimensions of K98MC throw

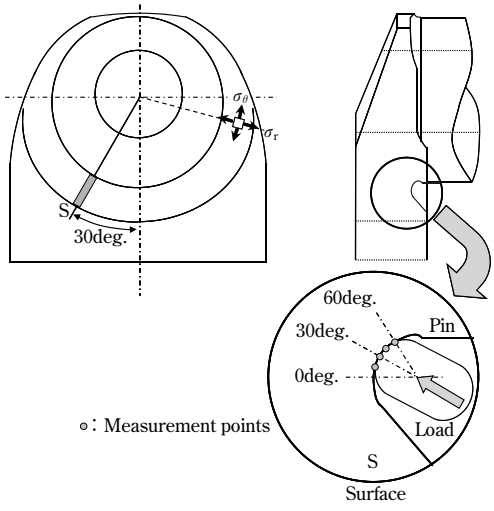

Fig. 4 Residual stress measurement points

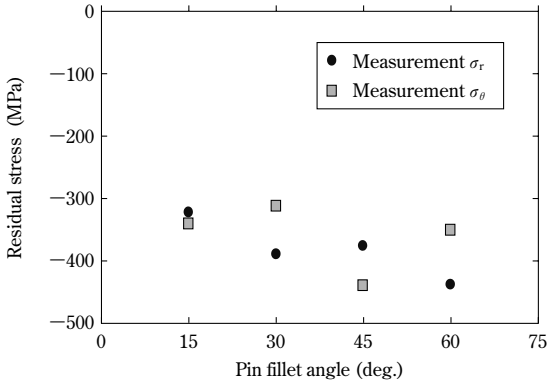

Fig. 5 Measured residual stresses on pin fillet surface

1.3 Methodologies for predicting fatigue strength considering combined loading

A unified rule of the International Association of Classification Societies for crankshafts for diesel engines (IACS UR M53, hereinafter simply referred to as "IACS rule") [3)] adopts an evaluation formula that takes both bending and torsional stresses into account. However, it should be noted that the IACS

rule focuses only on the stress amplitude of varying stress and disregards the effect of mean stress. To resolve this issue, the present study adopts a method of modifying bending stress amplitude according to the modified Goodman diagram formula, as previously reported.[2] Formula (1) is the modified Goodman diagram formula, while Formula (2) is an evaluation formula including a partial modification of the IACS rule. The effect of mean stress on torsional stress is known to be negligible and thus is ignored.

$$\sigma'_{ra}=\sigma_{ra}\Big/\left(1-\frac{\sigma_{rm}}{\sigma_B}\right) \quad \cdots\cdots (1)$$

$$\sqrt{\sigma'^2_{ra}+3\tau_a^2}=\sigma_w \quad \cdots\cdots (2)$$

wherein

σ_{ra} is the amplitude of bending stress working on the fillet surface

σ_{rm} is the mean stress working on the fillet surface

τ_a is the amplitude of torsional stress working on the fillet surface

σ_B is the tensile strength of the material, and

σ_w is the axial load, or the rotary bending fatigue strength of the material

As a method for evaluating the fatigue strength under combined loading with a mean stress, Sines proposed Formula [4] based on Formula (3) introduced from the octahedral shear stress criterion,

$$\left.\begin{aligned}&\frac{1}{\sqrt{2}}\sqrt{(\sigma_{ax}-\sigma_{ay})^2+(\sigma_{ay}-\sigma_{az})^2+(\sigma_{az}-\sigma_{ax})^2+6(\tau^2_{axy}+\tau^2_{ayz}+\tau^2_{axz})}\\&=A-B(\sigma_{mx}+\sigma_{my}+\sigma_{mz})\\&A=\sigma_{w,R=-1},\ B=\frac{\sigma_{w,R=-1}}{\sigma_{w,R=0}}-1\end{aligned}\right\} \quad (3)$$

wherein

$\sigma_{ai}\,(i=x,\ y,\ z)$ is the stress amplitude in x, y, z directions, respectively;

$\sigma_{mi}\,(i=x,\ y,\ z)$ is the mean stress in x, y, z directions, respectively;

$\tau_{aij}\,(i,\ j=x,\ y,\ z)$ is the shear stress amplitude on x, y, z surfaces, respectively;

$\sigma_{w,R=-1}$ represents axial load fatigue strength under alternating load condition; and

$\sigma_{w,R=0}$ represents axial load fatigue strength under pulsating load condition.

As one of the methods for evaluating fatigue strength under conditions where phase differences exist in the combined loading, Findley used a critical plane approach to propose (Formula (4))[5]. He postulates that fatigue life is controlled by a combination of alternating shear stress and maximum normal stress on a critical plane at an angle θ, which is determined by the condition that maximizes the left-hand side of Formula (4).

$$(\tau_\theta+k\sigma_\theta)_{max}=f \quad \cdots\cdots (4)$$

wherein

τ_θ is the shear stress amplitude in the plane inclined at an angle θ; and

σ_θ is the normal stress amplitude in the plane inclined at an angle θ. It is to be noted that k, f are constants determined by the material and can be obtained from two fatigue strengths under different loads. The present study adopts Formula (5), which comprises fatigue strengths under alternating and pulsating axial loads.

$$\frac{\sigma_{w,R=0}}{\sigma_{w,R=-1}}=\frac{k+\sqrt{1+k^2}}{2k+\sqrt{1+4k^2}},\ f=\frac{k+\sqrt{1+k^2}}{2}\sigma_{w,R=-1} \quad \cdots\cdots (5)$$

This paper takes up the above three methods for evaluating fatigue strength under combined loading. These methods were adopted for the fatigue test results and used for evaluating an actual crankpin fillet. Hereafter, the evaluation method using Formula (1) and Formula (2) is referred to as "Modified IACS", the method using formula (3) is referred to as "Sines", and the one using Formula (4) and Formula (5) is referred to as "Findley".

2. Validity of methods for predicting fatigue strength based on fatigue test

2.1 Material and specimen

Axial load and torsional load were simultaneously applied in coordinate phase to each specimen made of "Throw Grade 3 steel" during the fatigue tests. Meanwhile, the material constants of three methods for evaluating fatigue strength were determined from fatigue strengths independently obtained with either an axial or torsional load respectively. **Fig. 6** depicts the shape of the specimen used for the test.

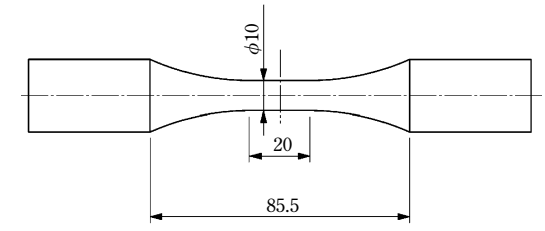

(a) Axial fatigue test

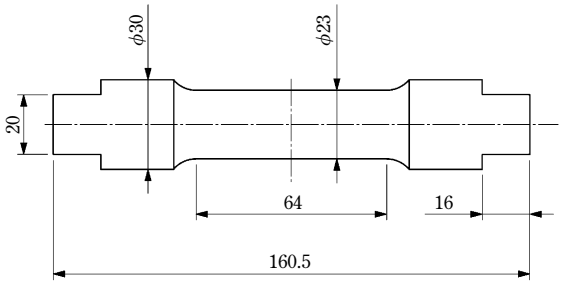

(b) Torsional or combined loading fatigue test

Fig. 6 Dimensions of fatigue test specimen

2.2 Testing conditions and results

Due to the limitation in the number of specimens, each fatigue test was started with a low load, and the load was increased step-by-step until failure. The number of cycles for a given loading condition was set to 3×10^6 cycles for fatigue tests under axial loading, and 1×10^6 cycles for the fatigue tests under torsional and combined loading.

In order to assess the effect of mean stress, axial load fatigue tests were conducted under two conditions of alternating and pulsating loading. The effect of mean stress on the torsional fatigue strength was regarded as negligible and, thus, the condition under which each torsional fatigue test was conducted did not include mean stress. The results of the axial loading and torsional fatigue tests are shown in **Fig. 7**. The axial load fatigue strengths for reversed and pulsating stresses agree well with the modified Goodman diagram.

The fatigue tests under combined loads were conducted under six conditions, as shown in **Table 3**. In each test, both axial-stress and torsional stress were applied simultaneously under three different levels of mean stress, i.e., "without mean stress (zero mean stress)," "with tensile mean stress" and "with compressive mean stress." The axial stress was applied in an alternating manner, while the torsional stress was applied in a pulsating manner. In the condition with a compressive mean stress, a constant mean stress of -200MPa was applied axially to simulate the compressive residual stress applied by cold rolling. The results are summarized in Table 3.

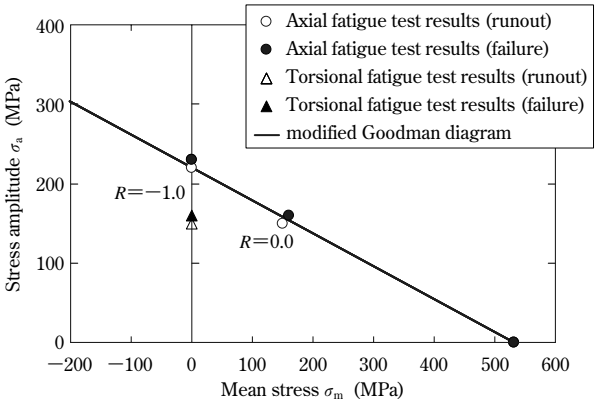

Fig. 7 Results of Axial and torsional fatigue test

2.3 Comparing methods for evaluating fatigue strength

The above three methods for fatigue strength evaluation were used to evaluate the results of the fatigue tests conducted under combined loading. **Fig. 8** compares the evaluation results obtained by these methods. Each vertical axis represents the quotient of the value on the right-hand side divided by the value on the left, for the respective evaluation formulas. The value of the right-hand side was calculated using the stress amplitude for the fatigue test results in the uniaxial direction shown in Fig. 7. The right-hand value is intrinsic to the material, and the fatigue limit is provided by the condition where the value of the left-hand side matches that of the right.

An accurate fatigue strength evaluation requires the vertical axis value of Fig. 8 to be smaller than 1.0, at least for the case in which failure occurs. If the value of the vertical axis becomes smaller than 1.0 for a non-failure (run out) condition, the evaluation is regarded to be on the safe side. According to Fig. 8, all the methods yielded evaluation on the safe side

Table 3 Fatigue test results under combined loading

Axial-torsion fatigue tests	Axial stress		Torsional stress		Result
	Amplitude	Mean	Amplitude	Mean	
without mean stress	143.8	0.0	115.0	0.0	runout
	149.9	0.0	120.0	0.0	failure
with tensile mean stress	130.0	130.0	65.0	65.0	runout
	140.0	140.0	70.0	70.0	failure
with compressive mean stress	200.0	−200.0	100.0	100.0	runout
	210.0	−200.0	105.0	105.0	failure

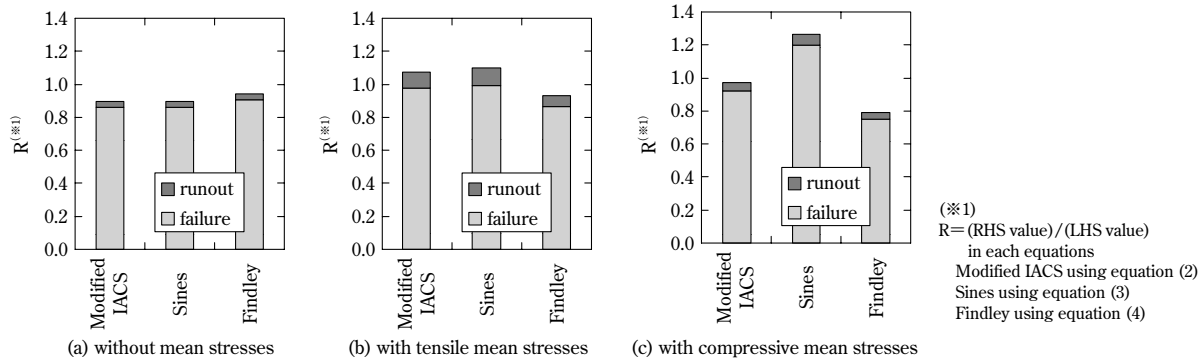

(a) without mean stresses (b) with tensile mean stresses (c) with compressive mean stresses

Fig. 8 Comparison of criterions under combined loading

for conditions of alternating and pulsating loading; however, for the conditions with compressive mean stress, "Sines" evaluation yielded a result significantly on the unsafe side. The "Modified IACS" and "Findley" methods yielded evaluations on the safe side regardless of the mean stress condition. The "Modified IACS" method yielded the most accurate result among the three.

3. Predicting effect of cold rolling on fillets

In a manner similar to that previously reported,[2] a MITSUI-MAN B&W 8K98MC-C engine was used for operational stress analysis to determine the stress generated on its pin fillet under working conditions. **Table 4** summarizes the data for the engine. **Fig. 9** shows the stress history of a pin-fillet with a fillet angle of 30 degrees (the angle as defined in Fig. 4). The pin-fillet was selected from the No.8 cylinder, since it is subjected to the maximum stress among all the fillets. The figure indicates that there is substantially no difference in the phase among the three stress components; and the stress, σ_θ, in the circumferential direction of the pin is smaller, in terms of both the stress amplitude and mean stress, compared with either the radial direction stress, σ_r, or the shear stress, τ.

The "Modified IACS" and "Findley" methods both yielded safe-side results as shown in Fig. 8 and were adopted for the evaluation of the stress generated on the pin fillet surface of the No.8 cylinder under working conditions. **Fig.10** shows the evaluation results for the fatigue strength of the pin fillet surface under combined loading. The effect of cold rolling has not been taken into account in this figure. The "Modified IACS" method cannot account for the stress, σ_θ, in the circumferential direction of the pin. Because of this, the "Findley" method was used to confirm the effect of the stress in the circumferential direction of the pin, and it was confirmed that the effect is negligible. Both the evaluations indicate that the stress currently generated is no greater than the fatigue limit. The "Findley" method yielded a result significantly more on the safe side than did the "Modified IACS."

Also confirmed was the effect of the compressive residual stress applied by cold rolling on the fatigue strength of the pin fillet surface. Either in Formula (2) of the "Modified IACS", or in Formula (4) of the "Findley," the permissible stress is determined by making the value of the right-hand side equal to that of the left-hand side, on the assumption that the stress conditions on the pin fillet surface were fixed. In this paper the stress condition on the pin fillet surface was set to a pulsating stress, and the ratio between the bending stress and torsion stress was fixed at 1/2, which is same as in the case of the ratio of maximum stress under the working conditions shown in Fig. 9. The compressive residual stress applied by cold rolling was obtained from the actual measurements shown in Fig. 5. **Fig. 11** shows the permissible stresses for the pin fillet surface determined by the "Modified IACS" and "Findley" evaluations, as well as the way in which the permissible stresses were affected by the compressive residual stresses applied by cold rolling. This figure indicates that Findley's evaluation yields results

Table 4 Particular of studied engine

Type		MITSUI-MAN B&W 8K98MC-C
Output	kW	45,680 (62,080HP)
MCR	rpm	104.0
Cylinder number		8
Cylinder bore	mm	980
Stroke	mm	2,400
Firing order		1-8-3-4-7-2-5-6
Throw material		Grade 3 (Cast steel)

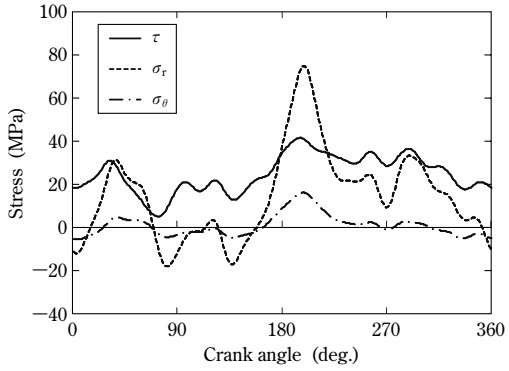

Fig. 9 Surface stress history of pin fillet （No.8cyl. pin fillet angle＝30deg.）

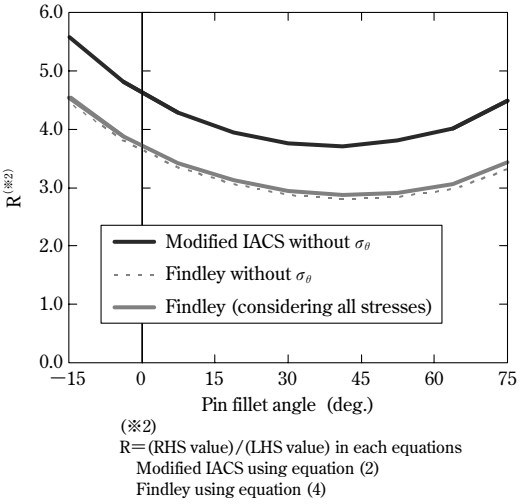

Fig.10 Evaluation of fatigue strength under combined loading of pin fillet (No.8cyl.)

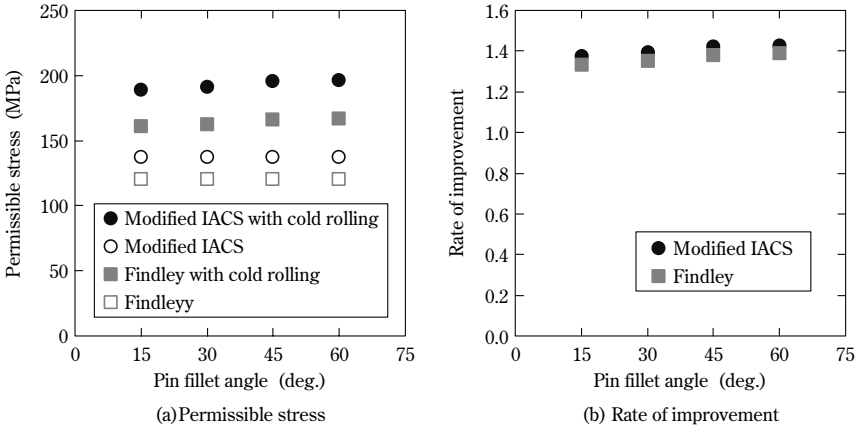

Fig.11 Rate of improvement of pin fillet permissible stress by cold rolling

more on the safe side than is the case with the Modified IACS; however, both methods evaluate the effect of the compressive residual stress on the permissible stress as being almost the same. It was also found that, on the pin fillet surface, the effect of the compressive residual stress applied by cold rolling improves the permissible stress by approximately 40%.

As reported in this paper, both the "Modified IACS" and "Findley" yield almost the same results for the evaluation of compressive residual stress applied by cold rolling on the fatigue strength of fillet surfaces. Findley's method makes it possible to account for all the stress components and phase differences; however, it requires repeated computation to determine the conditions that maximize the left-hand side of Formula (4). In the stress condition described in this paper, the stress in the circumferential direction of the pin can be regarded as negligible, and almost no phase difference exists. This has made accurate evaluation by the "Modified IACS" possible. The "Modified IACS" is a very convenient and effective evaluation method under stress conditions where only bending and torsion are combined, without a phase difference.

Conclusions

Fatigue tests were conducted under combined loading by regarding the effect of cold rolling as mean stress. The validity of three methods for determining fatigue strength under combined loading was evaluated. As a result, it was found that the "Modified IACS" and "Findley" methods provide evaluation that is on the safe side, regardless of the mean stress. The "Modified IACS" has turned out to be a very convenient and effective evaluation method in cases where the combined stress consists only of bending and torsion without a phase difference.

This evaluation method was adopted for the pin fillet surface of an operating engine. It turned out that the compressive residual stress applied by cold rolling improves the permissible stress on the pin fillet surface by approximately 40%. This study does not account for the effect of work hardening caused by cold rolling. Thus, a more significant improvement in fatigue strength can be expected for a material having a greater work-hardening effect. The cold rolling technique has been implemented in practice and is expected to see more use in the future.

References

1) T. Hamada, et al., *Annual Spring Meeting (131st), Iron and Steel Institute of Japan*, p.394.
2) M. Matsuda et al., *R&D KOBE STEEL ENGINEERING REPORTS*, Vol. 59, No. 1 (2009), pp.89-93.
3) IACS UR M53, Calculation of Crankshafts for I. C. Engines.
4) G. Sines, *NACA Tech. Note*, 3495 (1955).
5) W. N. Findley, *J. Eng. Ind., Nov.* (1959), pp.301-306.

Effect of Alloying Elements on Machinability and Hot Workability of α-β Titanium Alloy Containing Fe and C

Shogo MURAKAMI*1, Dr. Katsuhiko OZAKI*1, Kousuke ONO*2, Yoshio ITSUMI*3
*1 Materials Research Laboratory, Technical Development Group
*2 Titanium Marketing & Technical Service Section, Titanium Division, Iron & Steel Business
*3 Titanium Research & Development Section, Titanium Division, Iron & Steel Business

Many studies have been conducted on titanium alloys to improve their machinability and hot workability. They are inferior in machinability and hot workability when compared with other structural materials, such as steel and aluminum alloys. The KS EL-F (Ti-4.5Al-4Cr-0.5Fe-0.15C) that has been developed has mechanical properties equivalent to those of Ti-6Al-4V at room temperature and has superior hot workability. It was found that increasing Fe and decreasing Cr concentration in the chemical composition of KS EL-F improves both machinability and hot workability. The modified alloys (Cr: 1 to 2.5%, Fe: 1.25 to 2%) were found to decrease tool tip wear by almost 30% and the hot deformation stress by about 10%. Furthermore, decreasing Cr suppressed aging embrittlement caused by the precipitation of $TiCr_2$.

Introduction

As typified by Ti-6Al-4V alloy, α-β type titanium alloys have excellent specific strength, heat resistance and corrosion resistance, and are often used for parts for aircrafts, automobiles and motorcycles[1]. Titanium alloys are increasingly used for joint parts with carbon fiber reinforced plastic (CFRP), because they have a coefficient of thermal-expansion close to that of CFRP and do not cause electrolytic corrosion. This application is now commonly found; for example, it was used in the fuselage of the Boeing 787, which made its successful first flight in November, 2009. The demand for titanium alloys is envisaged to increase in the field of aviation[2]. The mechanical properties of α-β type titanium alloys can be adjusted by various heat treatments; however, commonly-used Ti-6Al-4V alloy suffers from a high machining cost, in addition to its high material cost, due to its poor forgeability and machinability compared with other materials such as steel and aluminum alloys. This has led to the development and use of various other alloys. KS EL-F is one of such alloys and has a significantly improved hot workability[3].

The KS EL-F alloy contains carbon, which decreases the alloy's deformation resistance at elevated temperatures, while maintaining its strength at room temperature. However, TiC may precipitate, depending on thermo-mechanical treatment, and the precipitates can increase tool wear[4].

This paper summarizes the results of the study on the effect of alloying elements on the machinability of the KS EL-F alloy, as well as the results found for the hot workability and machinability of modified compositions. Also discussed is the aging embrittlement of the modified compositions, since the KS EL-F alloy is known to exhibit aging embrittlement[5] and has limited applications where elevated temperatures are encountered.

1. Experimental procedure

1.1 Sample preparation

To experimentally select an alloy system, eight alloys as shown in **Table 1** were prepared; the KS EL-F alloy (Ti-4.5Al-4Cr-0.5Fe-0.15C, hereinafter referred to as "EL-F") being the reference composition; six alloys containing Fe Mo, V, Ni, Mn, and Co, these elements being substitutes for Cr; and one alloy containing Sn as a substitute for Al. The chemical compositions were designed such that the Mo equivalent falls in the range from 6.25% to 6.35% and Al equivalent in the range around 4.5%. Chromium was replaced to prevent the precipitation of TiC and to suppress the production of aging precipitates, $TiCr_2$. Aluminum was replaced because the substitution was expected to further decrease the deformation resistance at elevated temperatures. The tested materials were melted by vacuum arc melting to prepare button ingots of about $\phi 40 \times 20$mm in size, and each button ingot was forged into a size of about $\phi 25 \times 55$mm. In order to clarify in more detail the effect of alloying elements on machinability, it is preferable to have a beta-annealed microstructure that consists of many alpha laths in beta matrix. To

Table 1 Chemical compositions of samples for machinability (mass%)

No.	Al	Cr	Fe	C	Others	Mo equivalent	Al equivalent
EL-F	4.5	4	0.5	0.15	—	6.25	4.5
5%Mo	4.5	—	0.5	0.15	Mo:5.0	6.25	4.5
7.5%V	4.5	—	0.5	0.15	V:7.5	6.25	4.5
2Fe-1Cr	4.5	1	2	0.15	—	6.25	4.5
4%Ni	4.5	—	0.5	0.15	Ni:4.0	6.25	4.5
3%Mn	4.5	—	0.5	0.15	Mn:3.0	6.35	4.5
3%Co	4.5	—	0.5	0.15	Co:3.0	6.35	4.5
7.5Sn-2Al	2	4	0.5	0.15	Sn:7.5	6.25	4.5

achieve this, all the compositions were annealed at a temperature of 1,100℃, which is higher than the beta transus, held at the temperature for 2 hrs. and subsequently air-cooled.

Two compositions that were expected to be more excellent on the machinability (in **Table 2**) were then melted in a cold crucible induction melting (CCIM) furnace to prepare ingots of about ϕ155×165mm in size. Each ingot was forged into a round bar with a diameter of ϕ60mm, and the bar was annealed at 800℃ for 1.5hrs. Each annealed bar was investigated for its hot-workability, machinability and aging behavior. The samples of Ti-6Al-4V and "EL-F" alloys, both used as reference materials, were prepared from commercially available round bars of ϕ60mm.

1.2 Evaluation method

The machinability of each composition was evaluated using an optical microscope to determine the flank wear width of the cutting edge of a tool-chip after cutting. The details of the cutting conditions are shown in each figure.

Microstructures were observed under an optical microscope on each sample, which was mirror polished and etched by an etchant (i.e., water : nitric acid : hydrofluoric acid= 80 : 15 : 1). Hardness was measured using a Vickers tester with a load of 10kg.

Hot workability was evaluated on specimens, as shown in **Fig. 1**, each having a dimension of ϕ15× 22.5mm with notches 0.3mm deep on both sides.

Table 2 Chemical composition of high Fe system test alloys

Alloy	Al	Cr	Fe	C
EL-F	4.5	4	0.5	0.15
F-1	4.5	2.5	1.25	0.15
F-2	4.5	1	2	0.15

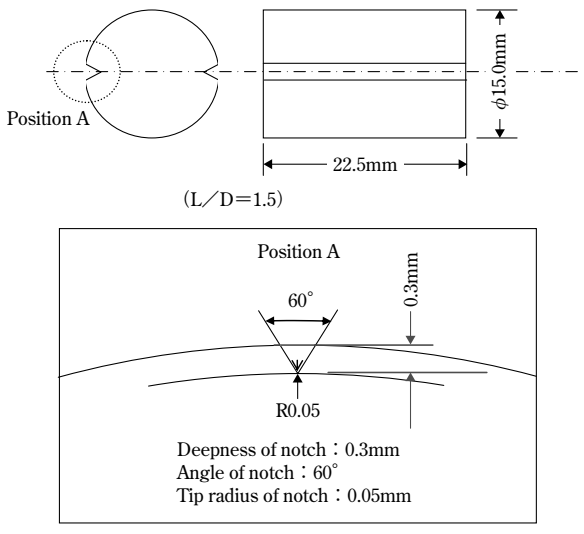

Fig. 1 Test specimen on limit of compressibility

The specimens were heated to 875℃ or 810℃ in an electrical furnace, held at their respective temperatures for 50min, and hot-pressed at 700℃ or 650℃, respectively, by a 1,600tonne press. The upper die was kept at a temperature ranging from 120 to 130℃ and the lower die at a temperature ranging from 150 to 170℃. The ends of each specimen were confined during the pressing. The strain rate was controlled to 1 to 2/s. The specimens were then investigated for the existence or non-existence of cracking at the bottom of the notches. A hot working simulator was used to evaluate deformation resistance on standard samples, each having a dimension of ϕ8×12mm, at working temperatures in the range from 400 to 800℃. The crosshead speed of the tester was set to 15mm/s, and the maximum deformation stress was taken as the value for the deformation resistance.

To study aging behaviors, each annealed sample was reheated to a temperature ranging from 300 to 700℃, held at that temperature for 8hrs and subsequently air-cooled. Tensile tests were conducted to study the change in strength and ductility. The tensile tests, according to JIS Z2241, were conducted on test pieces, each having a parallel portion diameter of ϕ6mm and a gauge length of 30mm.

A database, Ti-DATA ver.2, was adapted for thermodynamic calculation software, Thermo-Calc ver.P, to determine the quasi-binary phase diagram and the solid solubility limit of carbon.

2. Experimental results and discussion

2.1 Effect of alloying elements on machinability

In general, tool wear increases with an increase in the hardness of the work material. All of the compositions shown in Table 1 have an almost identical Vickers hardness of 310±10HV, hence the effect of hardness is regarded as negligible in this study. The microstructure of each composition exhibits a $\beta_{\text{-anneal}}$ structure, as shown in **Fig. 2**, with

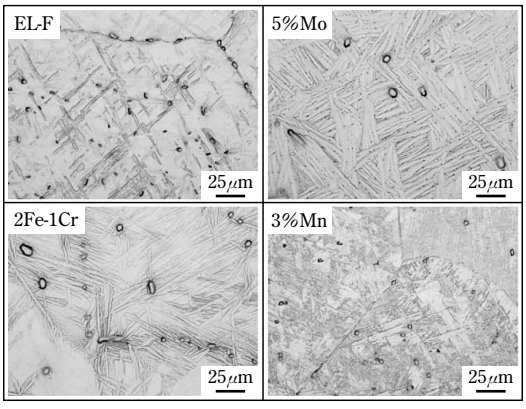

Fig. 2 Microstructure of representative samples

a small amount of TiC remaining.

Dry cutting was conducted with the cutting parameters as follows: cutting speed, 100m/min; feed rate, 0.1mm/rev; cutting depth, 0.5mm; and cutting distance, 50m. The flank wear widths after cutting are shown in **Fig. 3**. Compared with the tool wear by the EL-F reference composition, the materials designated as 5% Mo and 2Fe-1Cr show favorably small wear volumes. On the other hand, the materials designated as 7.5% V and 4% Ni show a tool wear volume almost the same as that of EL-F, and the ones designated as 3% Mn, 3 Co and 7.5Sn-2Al show wear volumes greater than that of the reference material.

As shown in Fig. 2, the 5% Mo and 2Fe-1Cr materials, each exhibiting a small wear volume, have alpha laths that are slightly larger. In general, larger strain concentration in a secondary shear zone facilitates the generation of cutting chips, improving machinability [6]. Because large alpha laths are considered to inhibit the strain concentration, the structure containing the phase was originally regarded to be unfavorable for machinability. Nevertheless, the structure exhibits a smaller tool wear volume, indicating that the substitution of Cr with Fe and/or Mo effectively reduces tool wear.

On the other hand, a large volume fraction of TiC precipitates increases tool wear, as shown in **Fig. 4** [4]; hence, it is preferable to make the solid solubility limit of carbon as large as possible when designing a composition. Using the thermodynamic calculation software, Thermo-Calc, the solid solubility limit of carbon near the beta transus was calculated for each composition of 5% Mo, 7.5% V, 1Cr-2Fe, 4% Ni and 7.5 Sn-2Al. The results are shown in **Table 3**. **Fig. 5** depicts a quasi-binary phase diagram in which the horizontal axis represents the carbon concentration of EL-F and 2Fe-1Cr materials. The addition of carbon should not noticeably deteriorate machinability as long as the carbon is added within the solid solubility limit shown in Table 3, because tool-wearing TiC precipitates near the beta-transus. Conversely, if the addition exceeds the solid solubility limit, the precipitation of TiC must be inhibited by adjusting the conditions of hot-working and/or annealing, including the annealing temperature and time. As shown in Table 3, the solid solubility limits of carbon for the 5% Mo material and for 2Fe-1Cr material are

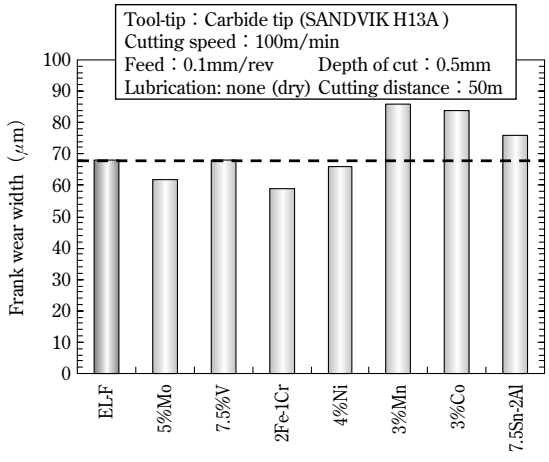

Fig. 3 Frank wear of test alloys for machinability

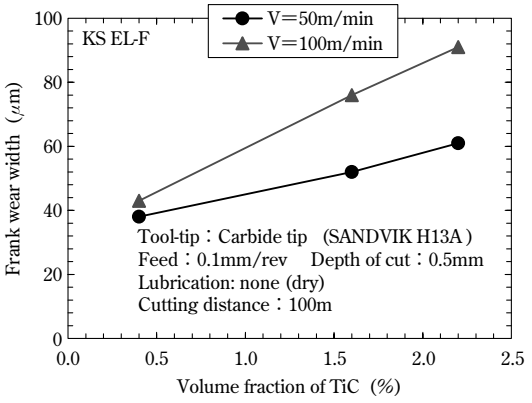

Fig. 4 Influence of TiC volume fraction on frank wear of cutting tool tip[4]

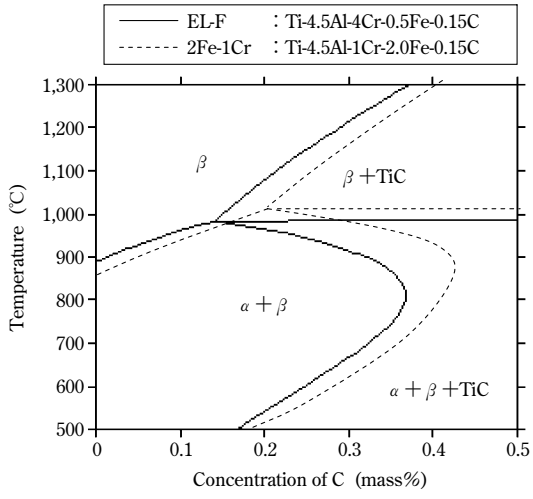

Fig. 5 Calculated phase diagram of Ti-Al-Cr-Fe-C system

Table 3 Solubility limit of C on beta transformed temperature in test alloys

No.	Solubility limit of C (mass%)
EL-F	0.140
5%Mo	0.182
7.5%V	0.133
2Fe-1Cr	0.198
4%Ni	0.118
3%Mn	no data
3%Co	no data
7.5Sn-2Al	0.259

greater than for the base material, EL-F. The greater solubility limit is preferable for inhibiting the precipitation of TiC, eliminating the need for specifically adjusting the conditions for forging, or for annealing.

As described above, it has been found that substituting Cr with Mo, or with Fe, effectively improves the machinability of EL-F. The substitution with Fe is preferable because the element is more widely found and less costly [7]. The following focuses on the compositions in which Cr is substituted with Fe.

2.2 Hot workability and machinability of α-β type titanium alloys containing high amount of Fe

Among alloying elements, Fe segregates significantly during actual production involving melting and casting. Taking this into consideration, the compositions shown in Table 2 were prepared for the evaluation of hot workability. **Fig. 6** shows the microstructures of the samples of these alloys. The samples have almost the same Vickers hardness of 340 ± 10HV.

Compression tests were conducted with the ends of each specimen confined to see if cracking occurred in the samples. **Fig. 7** shows the results of the evaluation. Compared with the conventional α-β type titanium alloy, Ti-6Al-4V (hereinafter referred to as "Ti-64"), the EL-F and the compositions with high content of iron, i.e., F-1 and F-2, have very high crack limits. In particular, the high-Fe compositions have crack limits even higher than that of EL-F. Also studied was the deformation resistance of each alloy. As shown in **Fig. 8**, the deformation resistance of Ti-64 depends less on temperature, while both EL-F and the high iron compositions (F-1, F-2) have deformation resistance that decreases significantly at elevated temperatures. At 600℃, F-1 and F-2 have a deformation resistance almost 10% smaller than that of EL-F. At 600℃, Fe, in α phase, has a diffusion coefficient approximately two orders of magnitude higher than that of Cr and, in β phase, three to four orders of magnitude higher than the same. Hence it is presumed that the decreased Cr and increased Fe content promote diffusion, further decreasing deformation resistance.

Fig. 9 compares tool wear, wherein each sample was cut at various cutting speeds ranging from 10 to 100m/min for a distance of 100m. Compared either with Ti-64, or with EL-F alloy, the alloys with higher Fe content wear the tools much less and exhibit the most favorable machinability. Comparing them with the results shown in Fig. 4, they exhibit smaller tool wear, despite the same cutting conditions and the doubled cutting distance. The decreased wear can be attributed to the microstructure, shown in Fig. 6, in which coarse TiC precipitates do not exist, and equiaxial α structure has been formed to be different from α lath structure shown in Fig. 2. In general, the equiaxial α structure has a fracture toughness lower than that of the alpha lath [8], which is considered to facilitate the generation of cutting chips and to decrease tool wear.

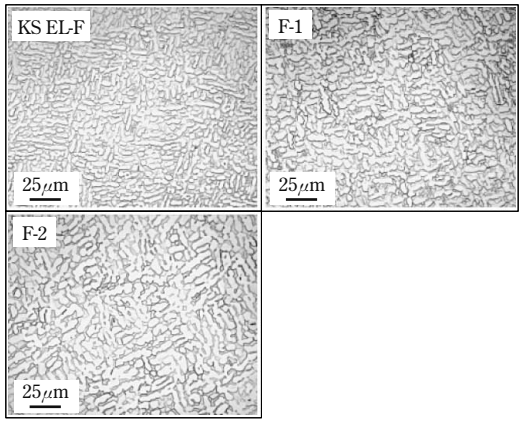

Fig. 6 Microstructure of high Fe system test alloys

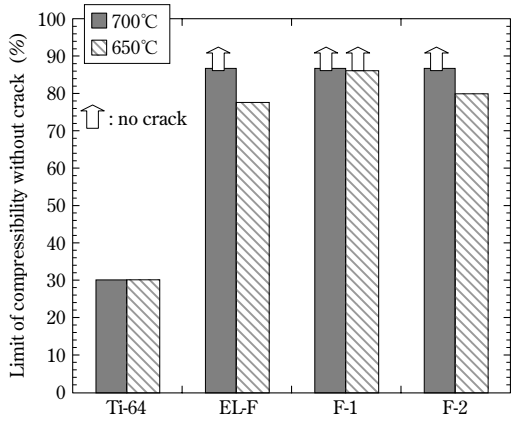

Fig. 7 Limit of compressibility of conventional and high Fe system alloys

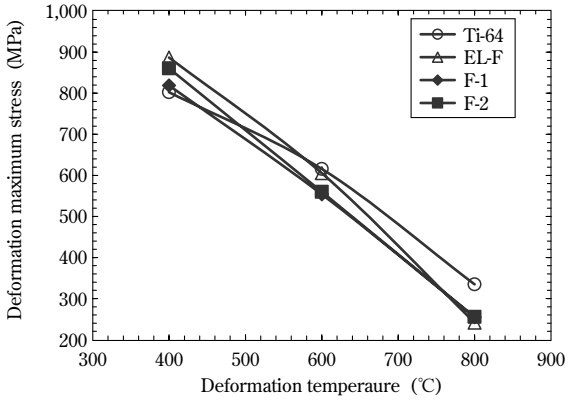

Fig. 8 Deformation stress of conventional and high Fe system alloys

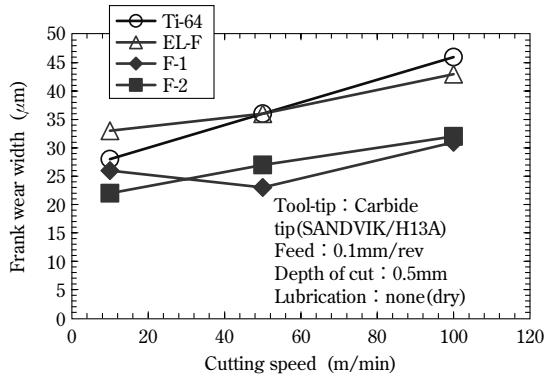

Fig. 9 Frank wear of conventional and high Fe system alloys

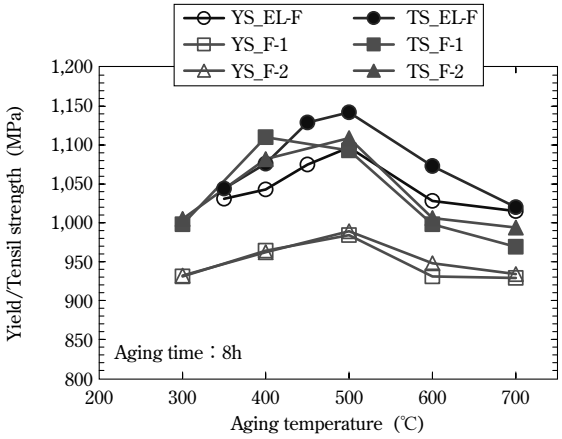

Fig.10 Strength after aging on high Fe system alloys (KS EL-F data : ref. 5))

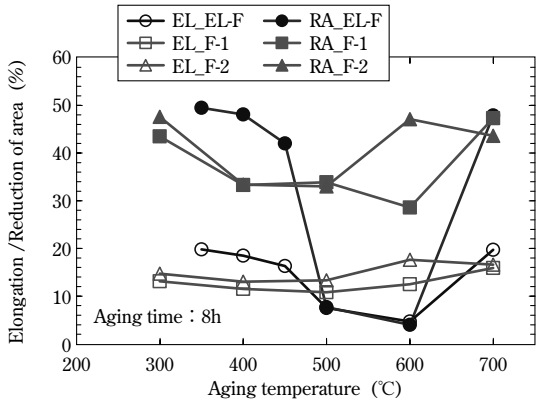

Fig.11 Ductility after aging on high Fe system alloys (KS EL-F data : ref. 5))

2.3 Aging behavior of α-β type titanium alloy having high Fe content

The EL-F alloy and high-Fe alloys shown in Table 2 were aged and subjected to tensile testing. **Fig.10** and **Fig.11** show their tensile properties after the aging. Each alloy has a high strength at around 500℃ with decreased ductility. Compared with the EL-F, the F-1 and F-2 exhibit a much smaller reduction of ductility. Aging embrittlement is known to occur in the EL-F alloy by the precipitation of $TiCr_2$[6], and the decreased Cr content in F-1 and F-2 is considered to inhibit the aging embrittlement. It should be noted that the F-1 and F-2 alloys have a slight difference in the temperature range where the changes in strength and ductility occur. This may be attributable to other precipitates, such as TiFe and $TiCr_2$, as well as to TiC, the details of which are to be the subject of future study.

Conclusions

A study was conducted on machinability and hot workability, using KS EL-F alloy as a reference. The results are as follows:

1) Using the KS EL-F composition (Ti-4.5Al-4Cr-0.5Fe-0.15C) as a base, alloys were prepared with decreased Cr and Al content. These elements were substituted with other alloying elements (i.e., Mo, V, Fe, Ni, Mn, Co, Sn). Each alloy was evaluated for its machinability. It has turned out that substituting Cr with Mo and/or Fe effectively improves the machinability.
2) In an equiaxial α structure, the alloys (1 to 2.5Cr-1.25 to 2Fe), which has a higher Fe content compared with Ti-6Al-4V, or with KS EL-F, exhibit tool wear decreased by about 30%. The alloys have an approximately 10% lower hot deformation resistance at 600℃ and crack limit compression rates no less than 5% higher.
3) Thermodynamic equilibrium calculation shows that the alloys containing high Fe have large solid solubility limits of carbon near the beta-transus. This makes the alloys less prone, compared with KS EL-F, to the precipitation of coarse TiC, which can adversely affect the machinability.
4) The alloys with compositions of decreased Cr and increased Fe have limited precipitation of $TiCr_2$, which prevents the aging embrittlement that occurs in KS EL at around 500℃.

A study is currently in progress to commercialize a modified alloy, KS 531C, which reflects the knowledge described in this paper. This work has been conducted as a part of the project, "Aerospace Industry Innovation Program-Advanced Materials & Process Development for Next-Generation Aircraft Structures" under the contract with RIMCOF Research Center of Materials Process Technology Center, founded by Ministry of Economy, Trade and Industry (METI) of Japan. We would like to express our sincere gratitude to all who were involved in this project.

References

1) *ADVANCED MATERIALS & PROCESSES/OCTOBER*, (2003), p.38.
2) "Material Technologies supporting the development of aircrafts (Japanese)," *Bulletin of The Iron and Steel Institute of Japan (Ferrum)*, Vol.11, No.2 (2006), pp.2-6.
3) H. Oyama et al., *Materials Science Forum*, 426-432 (2003) p.713.
4) K. Ozaki, *R&D KOBE STEEL ENGINEERING REPORTS*, Vol.55, No.3 (2005) pp.61-63.
5) K. Ono et al., *KEIKINZOKU*, Vol. 55, No. 12 (2005), pp.673-677.
6) Recht. R. F., *Trans. ASME* (1964), pp.186-193.
7) M. Niinomi, *61st Shiraishi Kinen Koza*, (2009), pp. 1-15.
8) M. Niinomi et al., *Tetsu-to-Hagane*, Vol. 72, No. 6 (1986), pp.99-106.

Pre-coated Titanium Sheet with Excellent Press Formability

Akihisa FUJITA*1, Yoshio ITSUMI*1, Tadashige NAKAMOTO*2, Kayo YAMAMOTO*2
*1 Titanium Research & Development Section, Titanium Division, Iron & Steel Business
*2 Sheet Products Development Department, Research & Development Laboratory, Iron & Steel Business

Plate type Heat Exchangers (PHEs) are one of the main applications for commercially pure titanium. The plates, each consisting of a titanium sheet press-formed into a complex corrugated pattern, are directly linked to high performance such as that seen in the thermal conductivity of the PHE. Now Kobe Steel has newly developed a pre-coated titanium sheet with excellent press-formability, whose design includes a lubricant coating that is easily removed by alkaline cleansing.

Introduction

Plate type heat exchangers (hereinafter referred to as "PHEs"), which exploit large amounts of sea water as their cooling media, are used in industrial fields including chemical plants, power-generating facilities and large transport vessels. PHEs employ large amounts of titanium for their primary parts such as their plates and piping because titanium exhibits excellent resistance against seawater corrosion. Now PHEs have become one of the main applications of titanium[1]. **Fig. 1** illustrates the operating principle of a PHE. A PHE is an apparatus for exchanging heat between hot water and seawater, each flowing in the opposite direction, wherein the flows are separated by titanium plates. Heat exchange occurs directly via these titanium plates. Each plate consists of a titanium sheet which is formed into a complicated corrugated shape and determines the heat transfer performance of the heat exchangers. The plate materials are also required to have increased strength, as the PHEs are increasingly being operated at higher pressures.

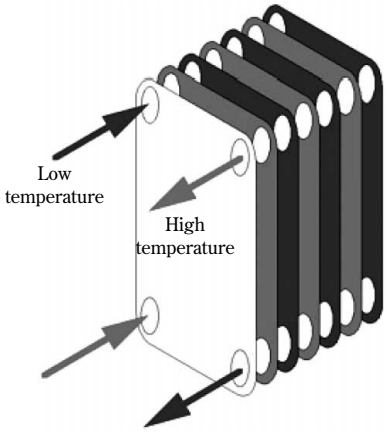

Fig. 1 Principle of plate type heat exchanger

Conventional PHEs use the softest grade of commercially pure (CP) titanium. If PHEs can employ harder CP titanium while preserving the favorable formability of the soft material, the application of titanium will expand to higher pressure applications with possible weight reduction achieved by wall thinning. Thus, a material for PHE plates is required to have both favorable press formability and high strength.

The strength and formability of a material, however, are in a trade-off relationship. Thus, Kobe Steel first focused on surface lubrication as a means for improving formability. Various methods have been known for such lubrication. One common approach is to attach a lubricating film to the surface to be formed[2]; however, this method costs time and money for attaching and detaching the film in actual operation. Another approach is to oxidize, or to nitride, the surface[3]; however, this method suffers from hardness and brittleness in the resulting surface layer, making the layer prone to crack in press patterns that are difficult to form. It also suffers from the fact that the surface layer may inhibit heat transfer. Taking these facts into account, Kobe Steel developed a method of pre-coating a lubricant, such that the pre-coated layer can be removed easily during the alkali cleaning that follows press forming. This method has enabled the use of JIS Class-2 CP titanium with a higher strength than that of conventional JIS Class-1 CP titanium, with the conventional press formability.

This paper introduces an adequate evaluation method uniquely developed for numerically evaluating the press formability of the titanium sheets used for PHE plates. Also introduced is a titanium sheet pre-coated with lubricant, which was developed using this evaluation method.

1. Kobe Steel's approach to evaluating press formability

During press forming, cracking occurs more frequently at sites called "flow passages" or "gaskets". The deformation mode at these sites is close to the mode of biaxial stretch forming[4), 5)]. Thus, the Eriksen value is used as a simple index of press formability. In reality, however, not only stretching, but also

other deformation modes, such as deep drawing, come into play together. Thus, a method must be established for quantitatively evaluating press formability in real-life situations.

To achieve this, attempts have been made to quantify press formability by scoring the conditions of cracking and necking after pressing, according to the following methods. For simplified evaluation, pressing was conducted using a compact test die which simulates a fishbone pattern, also known as the herringbone pattern, which is commonly found in the heat transfer portion of PHE plates. Also used was a large die covering a size close to that of an actual PHE.

It is to be noted that there are still issues remaining, including the fact that the present press-formability evaluation does not correlate sufficiently well with actual production. Further study will be conducted to improve the evaluation accuracy.

1.1 Evaluation using compact die

The following describes the shape of the compact die.

- Size: 160mm square (forming portion: 100mm square)
- Pitch between ridges: 10.0mm
- Ridge height: 4.0mm
- Radii of ridges R : 0.4, 0.6, 0.8, 1.0, 1.4, 1.8 (mm)
- Number of ridges: 6

The test samples were sized to 160mm square and were pressed by an 80tonne hydraulic press. The ridges were formed with a height of 3.4mm, the height having been determined to exhibit clear differences in cracking conditions between JIS Class-1 and Class-2 titaniums.

After test pressing, the samples were quantitatively ranked by the existence or non-existence of cracks and/or neckings at predetermined sites, as follows. In a press-formed sample (**Fig. 2**), a total of 24 sites were selected for evaluation, i.e., the 18 convex portions represented by the crossing between the 6 ridge-lines, the sites of potential cracks, and the three broken lines (A-A', B-B', C-C'), and the 6 concave portions on the broken line A-A', the concave portions where cracks can also originate. The following scoring was applied for each site:

- No cracking (soundness) : score 4
- Slight necking : score 3
- Significant necking : score 2
- Small cracking : score 1
- Large cracking : score 0

Based on these scores, the overall score was calculated as follows:

$$\text{Score}\ (\%) = (\Sigma\,(E/R))/(\Sigma\,(4/R)) \times 100 \quad \cdots\cdots\cdots(1)$$

wherein E is the score at each measuring point and R is the ridge radius (mm) at each measuring point. No cracking at any of the sites yields 100%, while the cracking at all the sites yields 0%. The reason for dividing by R is to account for the effect of bending deformation at each ridge with radius R.

1.2 Evaluation using large die

The shape of the large die is as follows:

- Size : 500mm square; (forming portion : 300mm square)
- Pitch between ridges : 14.9mm
- Ridge height : 8.1mm
- Radius of the ridges $R = 3.4$ (mm)

The test samples were sized to 500mm square and were pressed by a 1,000tonne servo-press. The criterion used for the compact die was adapted, making the forming height of the ridge portions

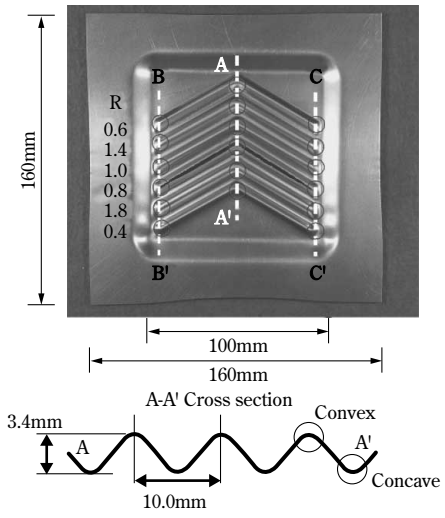

Fig. 2 Pressed test shape and positions for scoring in order to evaluate the pressformability using compact size test die

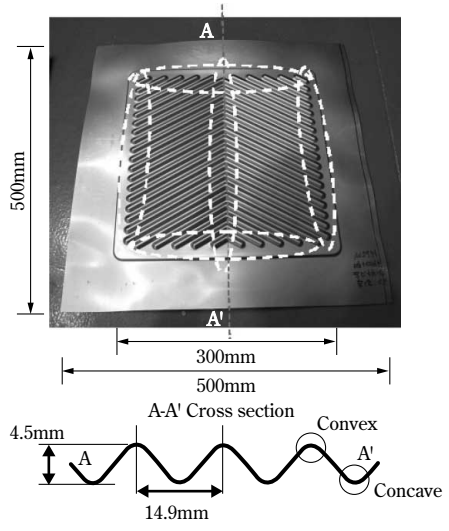

Fig. 3 Pressed test shape and positions for scoring in order to evaluate the pressformability using large size test die

4.5mm. There are a total of 92 evaluation sites in the areas surrounded by the broken lines in **Fig. 3**, including ridge ends and ridge central regions (convex portions and concave portions). Scoring was conducted in the same manner as in the case of the compact die. It is to be noted that R is set to be constant to form a shape close to that of a real product.

$$\text{Score}(\%) = \Sigma E/(4\times 92)\times 100 \quad \cdots\cdots\cdots\cdots\cdots\cdots(2)$$

2. Features of lubricant pre-coated titanium sheets

To study the difference in deformation between film lubrication and press oil lubrication, samples were pressed by the compact die with a lubricant film and with a press oil (SUNPRESS S-304 manufactured by Sugimura Chemical Industrial Co., Ltd.). **Fig. 4** compares the cross-sections of the ridge lines (R = 0.8, 1.0, 1.8) of the pressed samples. In the area surrounded by dotted circles, the sheet thickness is decreased in relation to its periphery. The comparison indicates that film lubrication results in less cracking and necking compared with press oil lubrication. In the case of press oil lubrication, the die comes into contact locally with the titanium sheet as the forming proceeds, restraining and immobilizing the sheet. In the meantime, the forming continues as a whole, causing necking and eventual cracking. On the other hand, in the case of film lubrication, the die does not directly contact the titanium sheet as long as the film is not broken, which assures the fluidity of the sheet, allowing the supply of the material from the surrounding region. This is considered to be the reason for the resulting uniform deformation compared with the case of press oil lubrication. Thus, in order to obtain a high formability, it is important to reduce the friction force as much as possible.

To improve lubricity and, in particular, to reduce the kinetic coefficient of friction, a lubricant pre-coated sheet was prepared. **Table 1** shows the composition of the lubricant pre-coating. Acrylic resin was chosen as the base resin because it adheres well to the titanium sheet, sufficiently follows the deformation and can easily be removed by alkali. Colloidal silica hardens the coating. Polyolefin wax improves lubricity against dies and was added to reduce the kinetic coefficient of friction of the pre-coating.

To study press formability under different lubricity, three types of lubricated titanium sheets were prepared using JIS Class-2 CP titanium, which has properties as shown in **Table 2**. One type of sheet was coated with press oil (SUNPRESS S-304 manufactured by Sugimura Chemical Industrial Co., Ltd.), another was covered with a film having the composition of the pre-coated lubricant without polyolefin wax (i.e., acrylic resin + colloidal silica), and the remaining one was pre-coated with lubricant. The coatings were applied with a roll coater and were dried in a thermostatic oven into a thickness of 1.0μm.

The coating thickness was adjusted by varying the solid content in the pre-coat solution. An X-ray fluorescence analyzer (MIF-2100, manufactured by Shimadzu Corporation) was used to quantify the amount of Si in the film. The coating thickness (μm) was determined from the coating quantity (g/m^2), obtained by Formula (3), which was converted by Formula (4).

$$\text{Coating quantity}(\text{g/mm}^2) = \text{Si}\times 60\times 100/28\times \text{C}\times 1000 \quad \cdots (3)$$

wherein Si represents the amount of Si in the coating(mg/m^2), C represents the concentration of SiO_2 in the surface treatment composition(%), the numeral 28 is the atomic weight of Si, and the numeral 60 is the molecular weight of SiO_2.

$$\text{Coating thickness}\ (\mu\text{m}) = (\text{Coating quantity}\times 0.1/2.2) + (\text{Coating quantity}\times 0.9/1.0) \cdots (4)$$

Formula (4) is applicable to a coating, that is 10% SiO_2 (specific gravity 2.2) and 90% resin + wax (specific gravity 1.0).

The press formability was quantified based on the method using the compact die as described in Section 1.1. The kinetic coefficient of friction was

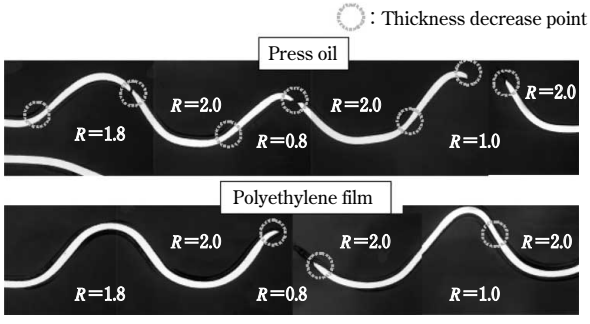

Fig. 4 Comparison between cross sections of pressed samples using press oil and polyethylene film as lubricant

Table 1 Composition of pre-coated layer

	mass%	Contents
Resin	80	· Acrylic resin consisted of alkylacrylate-methacrylate copolymer
Colloidal silica	10	· Amorphous SiO_2 · Alkali Na_2O
Wax	10	· Polyolefin wax

Table 2 Tensile properties of JIS Class-2 titanium sheet

Tensile direction	0.2%Yield strength (MPa)	Tensile strength (MPa)	Elongation (%)
L direction	243	396	31
T direction	288	389	29

measured by a tester (HEIDON by Shinto-Science) in the longitudinal direction with a test load of 500g, a sliding speed of 100mm/min and a sliding distance of 40mm. The partner material was a stainless steel ball of ϕ10.0mm.

Fig. 5 shows the relationship between the kinetic friction coefficient and press formability of the pre-coated sheet that was prepared. It can be concluded, despite the limited data, that the kinetic friction coefficient of the material is decreased by the application of the coating comprising resin and colloidal silica and is further decreased by the addition of polyolefin wax. This is accompanied by an improvement in formability.

To determine the optimum pre-coating thickness for press forming, the effect of pre-coat thickness on press formability was studied using JIS Class-2 CP titanium sheets having the properties shown in Table 2. **Fig. 6** shows the results. Formability improves with increasing coating thickness up to 0.5μm, but beyond this thickness, the improvement saturates. This result indicates that, within the range of deformation examined in this study, a coating as thin as 0.5μm serves the purpose.

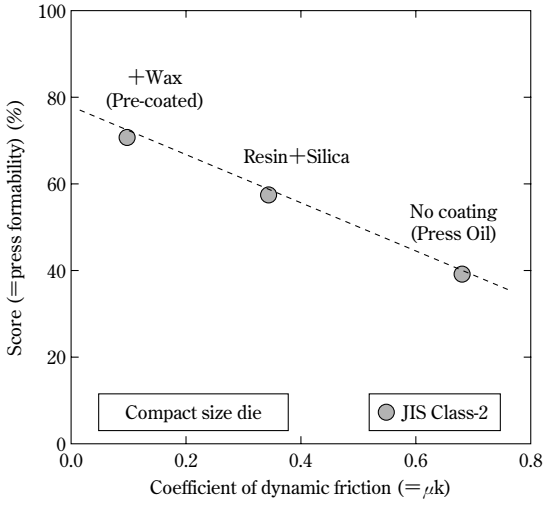

Fig. 5 Effect of coefficient of dynamic friction on press formability

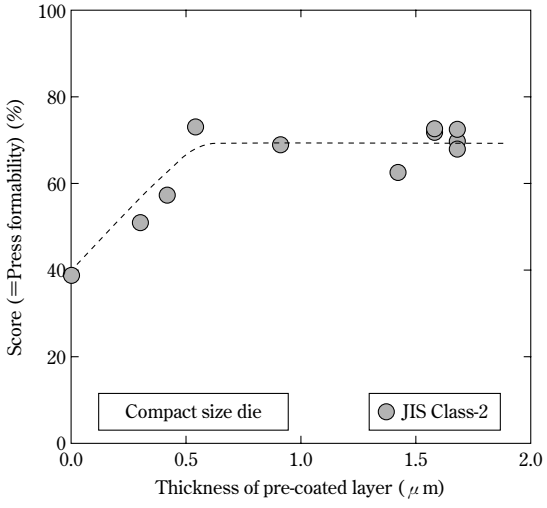

Fig. 6 Effect of thickness of pre-coated layer on press formability

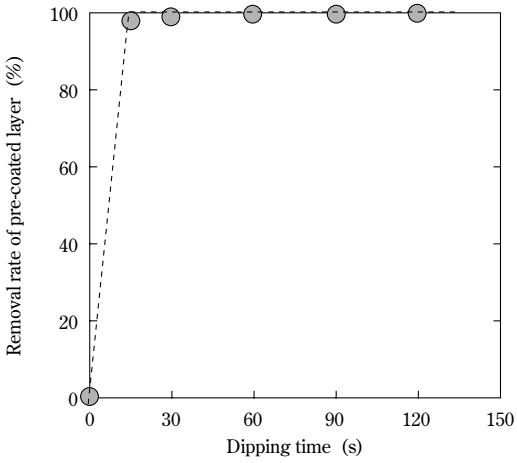

Fig. 7 Removability of pre-coated layer by dipping in alkaline cleaner bath

This lubricant pre-coating is applicable as-is to PHEs; however, heat transfer via the coating deteriorates the heat transfer performance. To resolve this issue, the coating was modified so that it can be removed by commonly-used alkali cleaning. The removability of the coating was evaluated by the test described below.

Each lubrication coating was measured for its coating quantity and subsequently immersed for a predetermined time in a cleaning solution which is generally recommended for titanium. After water cleansing and drying, the coating quantity was measured. The degreasing solution was a weak alkali, FINE CLEANER 4368 (manufactured by Nihon Parkerizing Co., Ltd.), which was diluted to a concentration of 20g/L. The bath temperature was set at 60℃. The removal rate of the coating was determined by Formula (6).

$$\text{Removal rate (\%)} = 100 \times (V_0 - V_1)/V_0 \quad \cdots\cdots\cdots (6)$$

wherein V_0 (g/m^2) and V_1 (g/m^2) are the coating quantities before and after the cleaning, respectively.

Fig. 7 shows the relationship between the coating removal rate and immersion time in the alkali solution. The results indicate that coating removal commences immediately after the coating is immersed. The coating is removed completely within 60 seconds. Since alkali cleaning is usually conducted for 1 to 3 minutes, the coating has been proven to be commercially applicable.

3. Press formability of lubricant-pre-coated titanium sheet for test production

Sheets of CP titanium, having different tensile

properties and pre-coated with lubricant, were tested for their press formability. The result was compared with press oil lubrication and with film lubrication. **Fig. 8** compares the results. The large die was used for evaluating formability in a condition close to that of real press forming. The figure indicates that the pre-coated lubricant offers a favorable formability similar to that offered by lubricant film. It was also found that the JIS Class-2 material, having strength 15% higher than that of JIS Class-1, exhibits a formability similar to that of the JIS Class-1 material that is press oil lubricated.

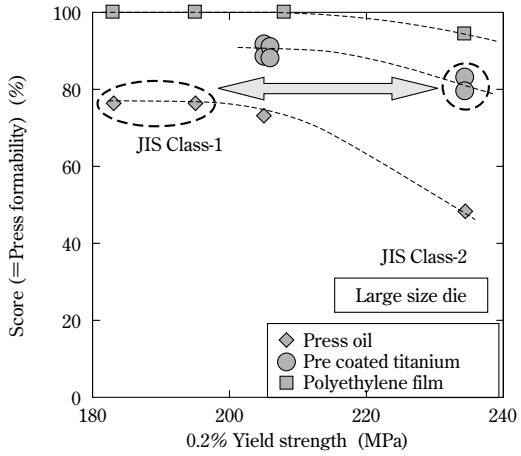

Fig. 8 Press formability of pre-coated JIS Class-1 and JIS Class-2, compared with using press oil and polyethylene film as lubricant

Conclusions

Kobe Steel developed a lubricant-pre-coated titanium sheet to be used for PHEs, a major application for commercially pure titanium. The pre-coating can be applied to JIS Class-2 material that has a strength higher than that of the conventional JIS Class-1, while retaining press formability close to that achieved by press-oil lubrication. The characteristics of the pre-coated titanium sheet have been introduced in this paper. This coating is also designed to be environmentally friendly. The coated layer, which is very thin, requires only light degreasing, leaves much less residue and can be used with much less concern than in the case of press oil. The newly-developed technology is widely applicable not only to PHEs, but also to various press-formed products.

References

1) Kusamichi et al., *Japan titanium industry and new technolog*, (1996), p.18. AGNE Gijutsu Center.
2) *Processing Technology of Titanium, Japan Titanium Society* (1992), pp. 82-86.
3) Takahashi et al., Development of High Lubricity Titanium Sheet with Excellent Press Formability, *Ti-2007 Science and Technology* (2007), pp.1079-1082.
4) Moriguchi et al., *R&D KOBE STEEL ENGINEERING REPORTS*, Vol. 32, No. 1 (1982), pp.24-27.
5) S. Ishiyama, Ph.D. thesis, Tohoku University, (1993). pp.13-78.

Newly Developed Iron-based Powder Mixture, High-density SEGLESS®, for High Density Compaction

Hironori SUZUKI[*1], Satoshi NISHIDA[*2], Takayasu FUJIURA[*3]
[*1] Takasago Steel Powder Plant, Steel Powder Division, Iron & Steel Business
[*2] Steel Powder Sales Department, Steel Powder Division, Iron & Steel Business
[*3] Research & Development Planning Department, Technical Development Group

The newly-developed lubricant Kobelco Polyhydroxyl Amide (KPA) consists of two different functional materials. Based on this feature, an iron powder mixture with KPA lubricant has better powder flow at the powder stage and better ejection performance at the green stage. Since KPA lubricity is superior to that of conventional lubricants, it is possible to reduce lubricant content without increasing the ejection pressure. By utilizing this process, high-density powder metallurgical parts can be made at a production cost relatively lower than that of conventional methods.

Introduction

Iron-based sintered parts are produced by a powder metallurgy process which comprises steps of mixing iron powder with additives, such as alloying powder and lubricant, compacting the mixture and sintering the compact (**Fig. 1**). It is a low-cost high-volume process for manufacturing complex-shaped products. Various efforts have been made to increase the strength of iron-based sintered parts, particularly for automotive engines, in response to the recent need for reducing automotive weight and enhancing engine performance. Among them, techniques such as warm compaction and die-wall lubricated compaction, which increase strength by decreasing porosity and thus densifying the sintered bodies, are effective because they are widely applicable to various sintered parts. These compaction techniques, however, require special ancillary equipment, such as heating and lubricant spray apparatuses. Thus, there has been a need for a more convenient method of high density compaction.

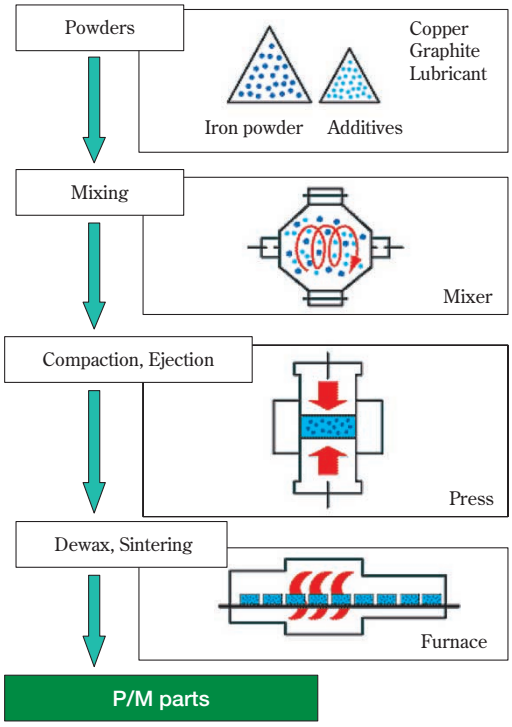

Fig. 1 Production process of powder metallurgy

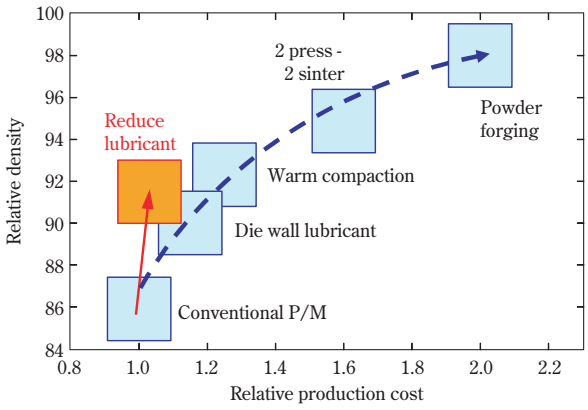

Fig. 2 Production cost and typical density for various high density processes

Fig. 2 depicts the relationship between the relative production costs and typical densities achieved by various powder metallurgical processes. Conventional high-density processes such as warm compaction, die-wall lubricated compaction and powder forging tend to cost more as the product density increases. Kobe Steel has found that a functional lubricant can decrease the amount of internal lubricant additive and achieve high density at relatively low cost without changing the existing equipment. This paper introduces the features of the functional lubricant, which exhibits excellent mold releasability. Also introduced is an iron-based powder mixture, containing the functional lubricant and designed for high-density compaction.

1. Role of lubricant in powder metallurgy

A lubricant for powder metallurgy is used for reducing frictional forces among powder particles, and between a compact and mold, particularly at the time of the powder compaction and releasing of the compact from the mold. Internal lubrication is a

common approach for using lubricant, in which metal soap, such as zinc stearate (hereinafter referred to as "Zn-st"), and/or wax resin, such as ethylene bisstearamide (hereinafter referred to as "EBS") are/is added in powder form to the base powder. **Fig. 3** shows the relationship between lubricant content and the theoretical maximum density achieved by a commonly-used composition consisting of 2% copper powder and 0.8% graphite powder with the balance of iron powder, and also the same relationship found in the case of iron powder alone. This clearly shows that increasing the amount of lubricant significantly decreases the density. It should be noted that the lubricant becomes useless once the compaction is completed and must be removed from the powder compact. Thus, a smaller amount of additive is preferable. To ensure lubricity, lubricant is typically added to iron powder in the amount of about 0.75 wt. percent.

Lubricant is known to significantly affect the flowability of the mixture consisting of iron powder and lubricant. It also affects the mold releasability, or the ejection force required to eject the compact of the powder mixture from a mold after compaction. The flowability is evaluated by a unique Kobe Steel method and is represented by the minimum bore diameter, known as the "critical discharging diameter," which allows the discharge of subject powder from a test container. After the comprehensive evaluation of a variety of commercially available lubricants, flowability and mold releasability have been found to be in a trade-off relation, as shown in **Fig.4** [1].

A lubricant with a low melting point accumulates easily on the wall surfaces of a mold and facilitates the release of compacts from the mold after compaction; however, it adheres strongly to iron powder during the powder mixing and may cause problems such as agglomeration and decreased flowability. A lubricant with a high melting point, on the other hand, remains solid during the powder mixing and exhibits excellent flowability; however, it does not accumulate sufficiently on the wall surface and may exhibit poor mold releasability. Thus, conventional lubricants have been unable to satisfy both flowability and mold releasability at the same time.

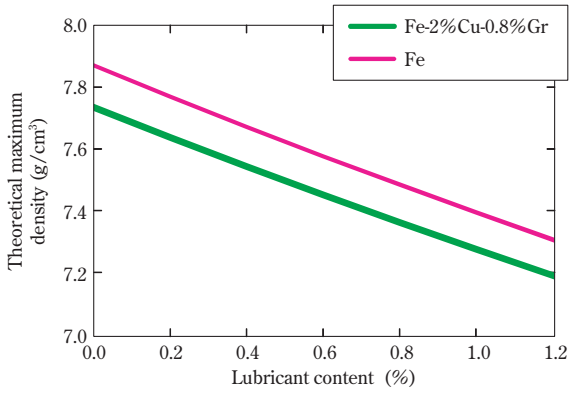

Fig. 3 Effect of lubricant content on theoretical maximum density

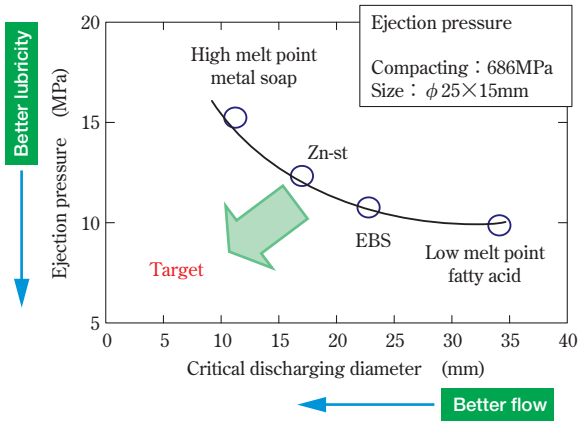

Fig. 4 Relation between flowability and ejection pressure for various lubricant mixture [1]

Targeting the development of a lubricant that can achieve both flowability and mold releasability, as shown by the arrow in Fig. 4, Kobe Steel has newly formulated a functional lubricant, Kobelco Polyhydroxyl Amide (hereinafter referred to as "KPA"), that selectively exerts the functions of assuring flowability during the powder mixing step and satisfying mold releasability at the time of compact ejection.

2. Concept of functional lubricant, KPA

KPA comprises two types of lubricants, both polyhydroxylamides, but having different melting points[2] (**Fig. 5**). A lubricant with a high melting point (no lower than 150℃), which contributes to flowability, is mixed with another lubricant with a low melting point (no higher than 100℃), which contributes to mold releasability, at an optimum ratio. These materials are also optimized for their qualities, such as particle size, to improve both characteristics, flowability and mold releasability. It should be noted that KPA is a wax-type lubricant consisting only of organic materials, which decrease the contamination of the sintering furnace and leave less smearing on the surfaces of sintered bodies.

A mixture of iron powder and KPA was compacted to evaluate dewaxing ability. The powder compact was heated in a thermobalance to measure its weight loss during heating (**Fig. 6**). The result indicates that the lubricant decomposes and gasifies as the temperature rises and is fully removed from

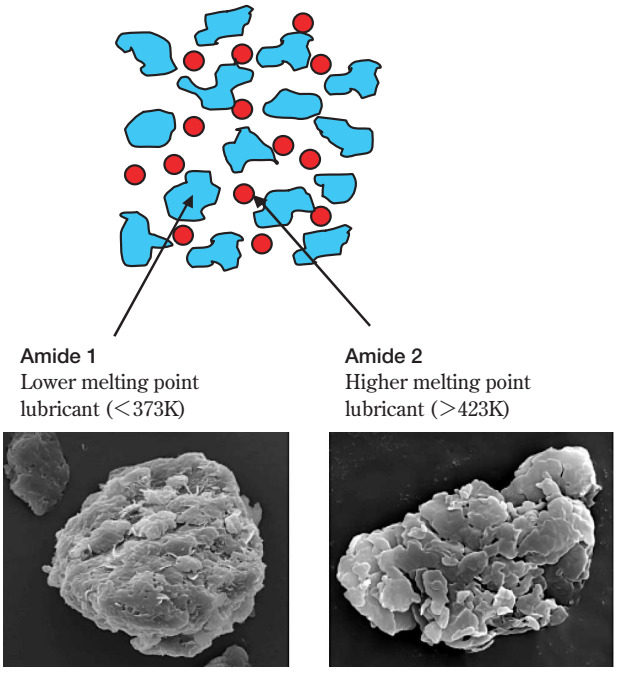

Fig. 5 Conceptual diagram of functional lubricant KPA

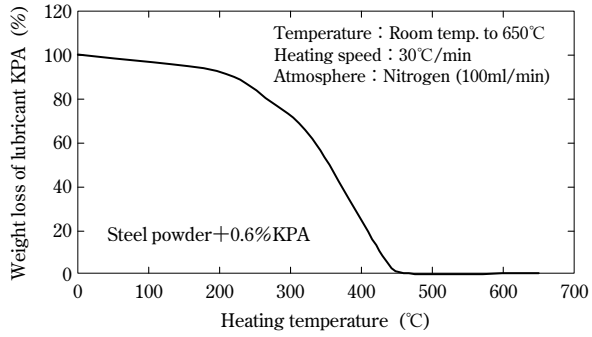

Fig. 6 Weight loss of KPA lubricant during heating

the powder compact in nitrogen atmosphere as the temperature approaches 450℃. Almost no residue of lubricant was found after the dewaxing.

3. Characteristics of KPA

3.1 Basic properties of powder mixture containing KPA[3), 4)]

Three different mixtures were prepared, each consisting of Kobe Steel's atomized iron powder, 300M (average particle size, 70 μm), 2% of copper powder (average particle size about 30 μm), and 0.8% of graphite powder (average particle size 5 μm), plus 0.75% of one of three lubricants, i.e., the newly developed KPA, Zn-st (average particle size 10 μm) and EBS (average particle size 25 μm). The latter two lubricants, both commercially available and added in the same amount, were used as reference materials. These compositions, called "SEGLESS", were designed to prevent the segregation of graphite.

Table 1 summarizes the typical properties of these three powder mixtures, as well as those of their green compacts. The apparent densities and flow rates were measured according to JIS 2504 and JIS 2502, respectively. Each powder mixture was compacted into a cuboid (31.8mm × 12.7mm × height 6.3mm) with a compacting pressure of 490MPa. The green density was measured on each powder compact. Also measured was its three-point bending strength according to JIS Z2511. The mold releasability was evaluated by the ejection force (peak value) required to release each compact of the powder mixture from the mold. The compacts were made into solid cylinders (ϕ25 × 25mm, ea.) under three different levels of compacting pressures; i.e., 490, 588 and 686MPa. **Fig. 7** shows the results of the releasability evaluations. The mixture containing KPA requires a significantly smaller ejection force compared with the conventional mixture and exhibits superior mold releasability. This effect is enhanced at higher compacting pressures. The ejection force is decreased by about 20% at a compacting pressure of 686MPa.

3.2 Lubrication mechanism of KPA

Several experiments were conducted to clarify the lubrication mechanism of KPA, which exhibits a superior mold releasability compared with Zn-st, or with EBS, both of which are commercially available. The viscoelasticity of the newly developed KPA and conventional EBS lubricants was measured

Table 1 Powder and green properties of KPA and other lubricant mixture

Lubricant	KPA	Zn-st	EBS
Apparent density (g/cm^3)	3.27	3.49	3.24
Flow rate (s/50g)	24.1	22.1	28.3
Critical flow diameter (mm)	22.5	22.5	30.0
Green density (g/cm^3)*	6.92	6.90	6.91
Green strength (MPa)*	12.0	10.0	10.6

*Compacting pressure : 490MPa

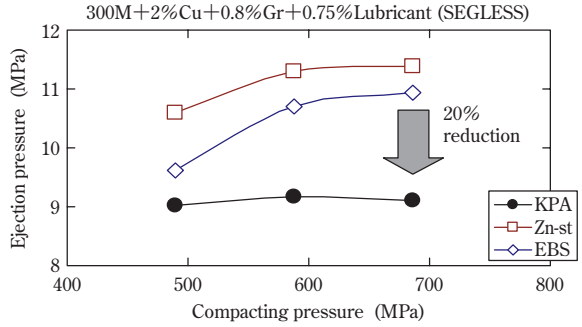

Fig. 7 Ejection pressure of KPA and conventional mixture

at different temperatures, using an instrument for measuring molten viscosity. The measuring instrument comprises a pair of disks, rotating in opposite directions, and a layer of lubricant placed between them, the layer being maintained at a thickness of about 1mm. The viscoelasticity is determined from the torque values obtained by rotating the disks at 62.5 rad/s (10Hz). **Fig. 8** compares the viscoelasticity of KPA to that of EBS. This figure indicates that the viscoelasticity of KPA gradually lessens as the temperature comes to exceed around 60℃, the temperature not exceeding the melting point of KPA, and remains lower than that of EBS. This suggest that, when ejecting the powder compact from a mold, KPA, which has a lower viscosity, can migrate more easily from the inside of the powder compact and accumulate on the mold wall surfaces to function better as a lubricant [5), 6)].

Next, the static friction coefficients of KPA and EBS were measured using a sliding tester, HEIDON. Each lubricant was applied on the surface of the steel plate in a thickness of 10 to 30 μm. Each sliding test was conducted with a load of 2 to 3MPa at a sliding speed of 100mm/min. The static friction coefficient was determined from the peak value of the resistance force during sliding for a specified distance. As shown in **Fig. 9**, the static friction coefficient of EBS increases with the rise in the surrounding temperature, while that of KPA appears to be independent of the temperature. This difference becomes more significant at temperatures above around 60℃. A static friction coefficient represents the lubricity of the lubricant itself. Even during compaction at room temperature, temperatures in some parts of the compact may exceed 60℃ due to the friction heat caused by the compacting pressure. This is considered to be the reason for the more effective lubricity of KPA.

Also studied were the behaviors of lubricants which migrate during compaction and ejection step to accumulate on the surfaces of the powder compacts. Three powder mixtures, each containing iron powder and 0.75% of the three respective lubricants, were compacted under three different pressures. For each compact, the surface that was in contact with a punch during the compaction was observed. **Fig.10** shows the results of energy dispersive X-ray (EDX) analyses performed on the surfaces of the powder compacts.

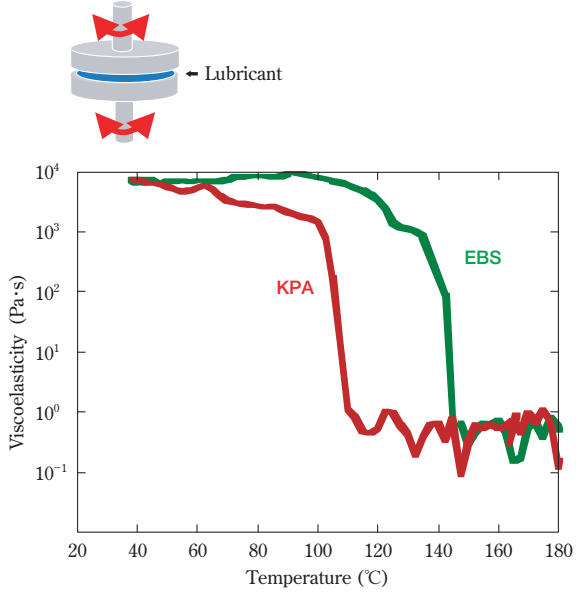

Fig. 8 Viscoelasticity of KPA and conventional lubricant

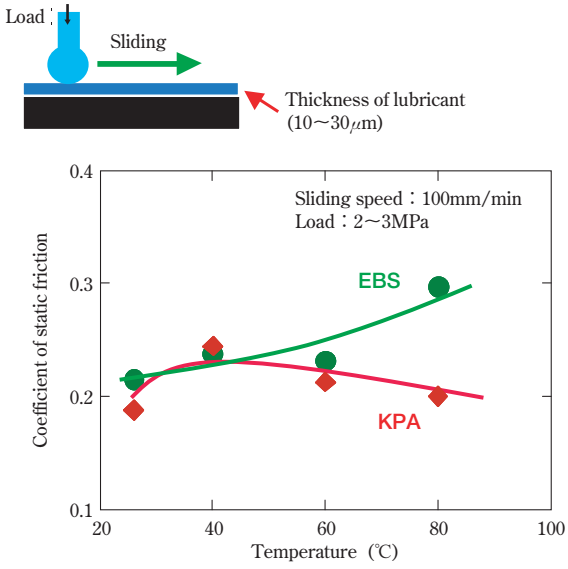

Fig. 9 Coefficient of static friction of KPA and conventional lubricant

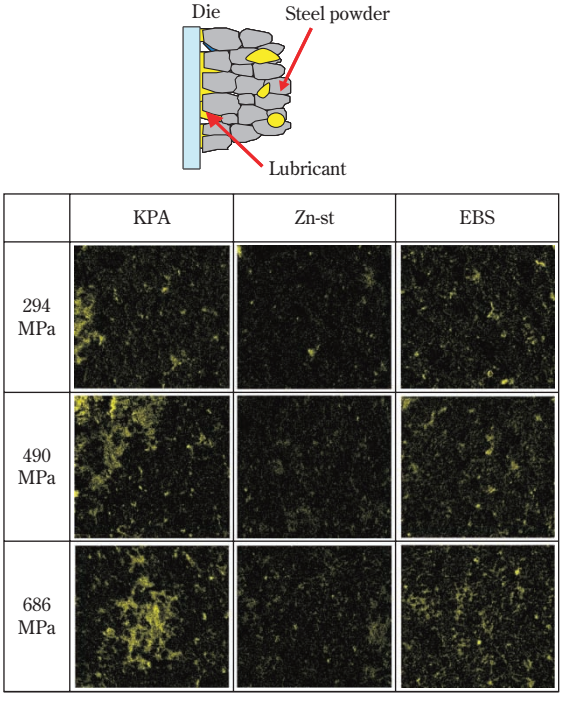

Fig.10 Lubricant distribution on surface of green compact by EDX

The yellow portions are where carbon, contained in each lubricant, is detected. These results indicate that, for all of the compacting pressures, larger quantities of KPA accumulate on the compact surfaces than in the case with the other two lubricants.

It has been concluded from the above experiments that KPA not only has a low static friction coefficient, which improves its lubricity, but also has a low viscosity that enables the lubricant to effectively seep to the compact surfaces. The resulting synergistic effect provides KPA with a mold releasability that is superior to that of other lubricants.

3.3 Characteristics of High-density SEGLESS containing KPA

KPA, with its excellent mold releasability, is expected to reduce the burden imposed on molds. This will extend the life of the molds and enable it to be applied to parts having complicated shapes. One way of using KPA is to decrease the amount added to a level that attains the ejection force achieved by conventional lubricants, while increasing the density of compacts. The high-density process with a reduced amount of lubricant additive does not call for additional equipment and, thus, can be established with relative ease. Such a process emits much less gas during dewaxing and is more environmentally friendly. This section introduces the features of a newly developed powder mix, "High-density SEGLESS", which contains KPA and halves the amount of lubricant additive compared with conventional technology.

Two types of powder mixtures were prepared: i.e., High-density SEGLESS, consisting of Kobe Steel's high-compressibility iron powder, 300NH, 2% of copper powder (average particle size, about 30μm), 0.8% of graphite powder (average particle size, 5μm) and 0.4% of KPA; and a conventional SEGLESS, containing 0.8% of conventional lubricant, EBS (average particle size, 25μm). **Table 2** summarizes the powder properties of High-density SEGLESS and the conventional SEGLESS. Both have a similar apparent density, however, High-density SEGLESS has a smaller amount of lubricant added and thus has a flow rate improved by 3s/50g compared with that of the conventional SEGLESS.

Fig.11 compares High-density SEGLESS with the conventional SEGLESS, in terms of the relationship between the compacting pressure, required to compact the mixture into a solid cylinder of $\phi 25 \times 25$mm, and the resulting compact (green) density. High-density SEGLESS exhibits an improved compact density, 7.30g/cm^3 (compacting pressure, 686MPa), which is a result of the reduced amount of lubricant and is higher by 0.2g/cm^3 than that achieved by the conventional SEGLESS. **Fig.12** shows the forces required to eject the powder compacts of the various mixtures. In both the cases, the ejection force increases with increasing compact density. When comparing the two mixtures at a given compact density, High-density SEGLESS with reduced lubricant exhibits an ejection force comparable to that of conventional SEGLESS, proof that the amount of lubricant additive can be decreased without sacrificing ejection force.

Finally, both of the powder mixtures were compacted under different pressures into a ring shape with an outer diameter of 64mm, inner diameter of 24mm and height of 10mm. The ring-shaped compacts were sintered at 1,120℃ for 30 minutes in a nitrogen atmosphere containing 5% of hydrogen to produce sintered bodies. The characteristics of the sintered bodies were compared. Compressional load was applied by a press in the radial direction of each ring-shaped sample. The radial crushing strength was determined from the load that caused fracturing in each ring. The results are shown in **Fig.13**. In the case of High-density SEGLESS, the strength of the sintered body increases

Table 2 Powder properties of high density SEGLESS and conventional SEGLESS

	High density SEGLESS	Conventional SEGLESS
Apparent density (g/cm^3)	3.49	3.46
Flow rate (s/50g)	23.1	26.5

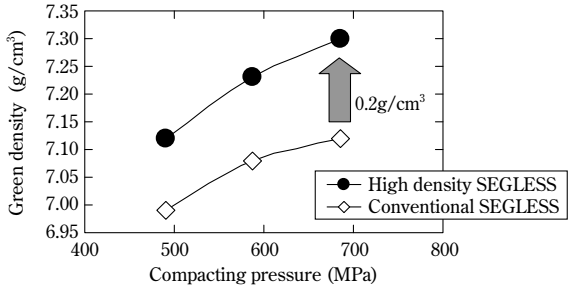

Fig.11 Compressibility curve of high density SEGLESS

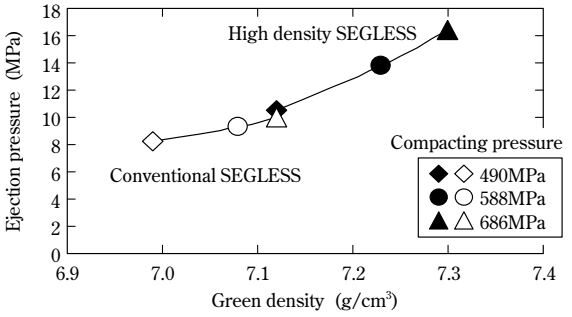

Fig.12 Ejection pressure of high density SEGLESS

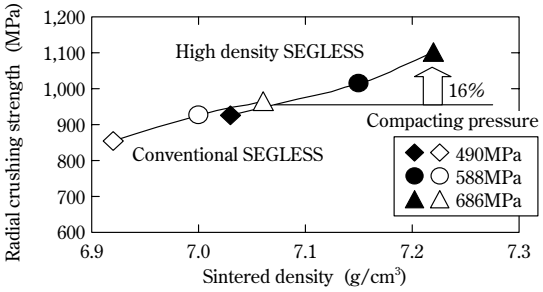

Fig.13 Radial crushing strength of sintered high density SEGLESS

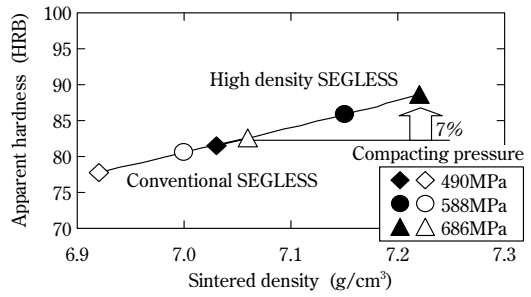

Fig.14 Apparent hardness of sintered high density SEGLESS

with increasing density, and, for a given compacting pressure, it increases by about 16% compared with conventional SEGLESS. **Fig.14** shows the apparent hardness, measured on the Rockwell Hardness B-Scale, of each sintered body. The hardness was determined from the average of the values measured at three points on the upper surface and another three points on the lower surface. The hardness also increases with increasing density in the same manner as in the case of strength; at a compaction pressure of 686MPa, it increased by about 7% as compared with conventional SEGLESS.

Conclusions

The following summarizes the characteristics of a newly developed functional lubricant, Kobelco Polyhydroxyl Amide (KPA), developed for powder metallurgy, and the features of the powder mixture comprising iron powder and the lubricant:

1) KPA, consisting of two types of lubricants with different melting points, can improve both flowability and mold releasability at the same time. Such an improvement has conventionally been difficult to achieve.
2) The iron-based mixed powder containing KPA exhibits an excellent mold releasability, which reduces the burden imposed on molds and is suitable for use in parts having complicated, thin-walled shapes.
3) High-density SEGLESS, containing an amount of KPA decreased to a level that exhibits the same ejection force as exhibited by conventional SEGLESS, enables the production of higher density parts without additional equipment. This responds to the needs for parts with higher strength and lower weight, features receiving much attention in recent years.
4) The newly developed lubricant is applicable to a wide variety of products, such as pure-iron based machine parts, high-strength parts made from alloy powder with inferior compactability and magnetic iron powder requiring higher density.

References

1) H. Suzuki et al., *R&D KOBE STEEL ENGINEERING REPORTS*, Vol.55, No.3 (2005), pp.64-67.
2) S. Nishida et al., *Proceeding of 2006 Powder Metallurgy World Congress* (2006), Part Ⅱ, pp.731-732.
3) H. Suzuki et al., *Japan Society of Powder and Powder Metallurgy, Abstracts, Annual Spring Meeting* (2005), p.124.
4) H. Suzuki et al., *Proceeding of the 2007 International Conference on Powder Metallurgy & Particulate Materials* (2007), Part 3, pp.11-18.
5) Y. Ito et al., *Japan Society of Powder and Powder Metallurgy, Abstracts, Annual Autumn Meeting* (2007), p.81.
6) Y. Ito et al., *Proceeding of the 2008 World Congress on Powder Metallurgy & Particulate Materials* (2008), Part 3, pp.41-49, 74.

Newly Developed Iron Powder for Highly Efficient Dust Cores

Hirofumi HOJO[*1], Nobuaki AKAGI[*1], Tetsuya SAWAYAMA[*2], Hiroyuki MITANI[*3]
[*1] Takasago Steel Powder Plant, Steel Powder Division, Iron & Steel Business
[*2] Steel Powder Division, Iron & Steel Business
[*3] Materials Research Laboratory, Technical Development Group

Dust cores are made by compacting insulated magnetic powder. One of the advantages of dust cores is magnetic isotropy, which enables three-dimensional magnetic circuit designs. Such designs are expected to reduce the size and weight of magnetic parts. There is a strong demand to reduce core loss so that the cores can be used more for magnetic parts, such as motor cores. This paper reports on methods for reducing iron loss in dust cores and on the magnetic properties of the dust cores consisting of improved powder made by a new method. A dust core with an iron loss of 28.6W/kg was produced. This core is comparable with ones made of laminated steel sheets.

Introduction

To decrease the environmental burden and to save energy, there are growing needs for electromagnetic components with reduced loss. Components such as photovoltaic power conditioners and the reactors that are used for boost converters of hybrid electric vehicles (HEVs) and electric vehicles (EVs) require magnetic materials that have low magnetic loss and can be used at higher frequencies. In addition, the electric motors used for HEVs and EVs call not only for reduced magnetic loss, but also for smaller size and lighter weight.

Dust cores, made by compacting insulated soft-magnetic powder, have the advantage that they can suppress eddy current loss because the constituent particles are electrically insulated. The eddy current loss is proportional to the second power of frequency. Thus, components used at higher frequencies can better exploit this advantage. Because of this, dust cores are progressively being used for applications such as the reactors for the boost converters of HEVs.

In addition, dust cores have isotropic magnetic characteristics. This enables the designing of new magnetic circuits with three-dimensional structures, which have been difficult to design using conventional magnetic cores made of laminated steel sheets having magnetic anisotropy. Because of this, various efforts are being made to exploit dust cores for the downsizing and weight reduction of components, including electric motors[1), 2)]. Such components, however, are typically driven by the commercial frequency, which is so low that the iron loss is governed predominantly by hysteresis loss, rather than by eddy current loss. This makes it difficult to take advantage of the reduced eddy current loss of dust cores, hence the desire for a dust core with decreased hysteresis loss.

The present paper describes technologies, including the determination of optimum temperature for magnetic annealing to relieve strain for reducing the iron loss of dust cores. This paper also includes the development of a highly heat-resistant insulation coating for the optimum magnetic annealing, as well as the effect of powder particles and crystal grain sizes on iron loss. Also introduced are the characteristics of a powder compact with reduced iron loss, the compact having been developed on the basis of the knowledge that was obtained.

1. Factors determining iron loss of dust core

In general, iron loss consists of eddy current loss and hysteresis loss. The eddy current loss is further classified into intra-particle eddy current loss, caused by the eddy current flowing inside each individual particle, and inter-particle eddy current loss, caused by the eddy current flowing across the particles throughout the component.

The hysteresis loss of a material, on the other hand, corresponds to the looped area in the BH (magnetic flux density vs. magnetic field) curve, in which the size of the loop correlates strongly with the material's coercive force (i.e., coercivity). Thus, decreasing the coercivity decreases the hysteresis loss. The factors determining coercivity are particle composition (solid solution elements), precipitates, inclusions, crystal grain boundaries, powder surfaces and dislocations (strains), i.e., the factors that inhibit the movement of domain walls.

The factors determining the intra-particle eddy current loss include particle composition (solid solution elements), which affects the electrical resistivity of each particle, and particle size, which defines the area within which the eddy current flows. The factors determining the inter-particle eddy current loss include the electrical resistivity of the insulation coating, which affects the inter-particle insulation (**Fig. 1**).

Among these factors, the coercivity is decreased more significantly as the temperature for magnetic annealing, performed to relieve strain, rises.

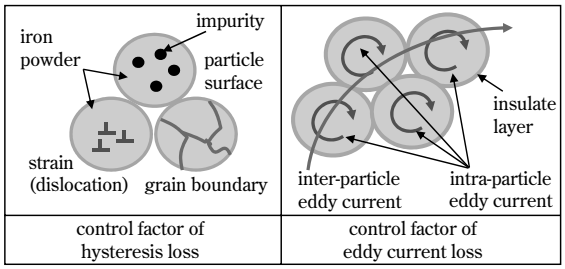

Fig. 1 Control factor of iron loss

Conventional dust cores, however, suffer from the problem of the lack of heat resistance of the insulation coating on the particle surfaces, which causes the fracture of inter-particle insulation during annealing at elevated temperatures, resulting in increased inter-particle eddy current loss. Another known technique for decreasing coercivity is to increase particle size. Intra-particle eddy current loss, however, is proportional to the second power of particle size; hence particle size is a factor controlling trade-off characteristics.

From the above, it can be seen that an important issue in reducing the iron loss of a dust core is to suppress its eddy current loss and at the same time to decrease its hysteresis loss.

2. Optimum annealing temperature for relieving stress from compacts

Dust cores are compacted in dies. Therefore, the powder particles are plastically deformed and have a large amount of strain introduced. Strain (dislocation) is a factor which increases coercivity and can be relieved by heat treatment. A study was conducted to determine the optimum annealing temperature for strain relief.

2.1 Experimental method

Pure iron powder (300NH, manufactured by Kobe Steel; average particle size, approximately 100 μm) is mixed with 4.0mass% of highly-pure alumina fine powder (manufactured by Showa Denko K.K.; average particle size, approximately 1.3 μm), along with an organic binder. The particles of the highly-pure alumina powder are adhered to the surface of iron powder particles, forming insulation layers. The powder mixture was compacted into ring-shaped samples, each having an outer diameter of 45mm, inner diameter of 33mm and height of 5mm, by die-wall lubricated compaction with a compacting pressure of 980MPa. Zinc stearate was used as the die wall lubricant. Each compact was annealed in a nitrogen atmosphere at a temperature in the range of 673 to 1,073K for 7.2ks. The direct-current magnetic properties were measured on these samples, using a BH curve tracer (BHS-40S by Riken Denshi Co., Ltd). Furthermore, the sample cross-section was etched with NITAL (an etching solution consisting of ethyl alcohol and nitric acid) so as to be subject to metallographic observation under an optical microscope.

2.2 Results and discussions

Fig. 2 shows the relationship between the temperatures for magnetic annealing and the resulting coercivities of the samples. The coercivity decreases as the annealing temperature approaches 973K. This is considered to be caused by the relief of strain in the compacts by the magnetic annealing. The sample annealed at 1,073K exhibits a coercivity higher than that of the sample annealed at 973K. There is only a slight difference in coercivity between the compact annealed at 873K and the one annealed at 973K. This result indicates that the coercivity-decreasing effect of annealing becomes nearly saturated at about 873K.

Fig. 3 are optical micrographs of the cross-sections of two compacts, i.e., one before magnetic annealing, and the other after magnetic annealing at 1,073K. The crystal grains of the compact annealed at 1,073K are finer than they were before magnetic annealing. This shows recrystallization. In general, the smaller the grain size, the higher the coercivity. Thus, the increase in coercivity of the compact annealed at 1,073K is attributable to the grain refining caused by recrystallization. If we examine this in more detail, in the temperature range no lower than 873K, the

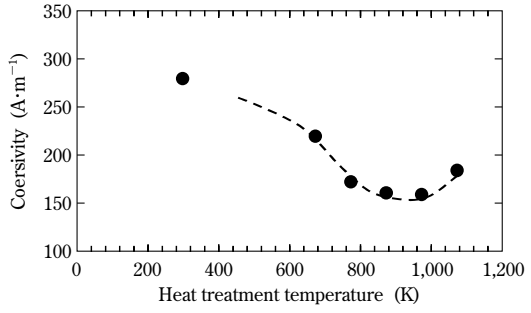

Fig. 2 Relationship between coersivity and annealing temperature

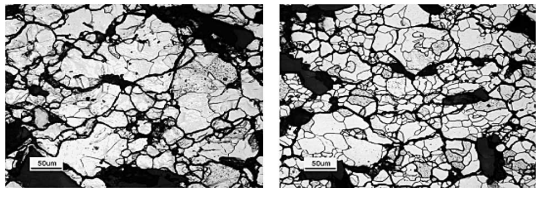

Fig. 3 Cross sectional microstructure of before annealed (left) and annealed at 1,073K(right) compact

coercivity-decreasing effect of magnetic annealing lessens, and the upper limit annealing temperature, effective in decreasing coercivity, is regarded as to be approximately 973K. In addition, magnetic annealing at 1,073K has turned out to adversely affect the coercivity reduction.

From the above, the optimum temperature for magnetic annealing of dust core made from pure iron powder is concluded to exist in the temperature range from 873K to 973K.

3. Heat resistance of insulation coating

The magnetic annealing at the optimum temperature determined in section 2 is effective in decreasing coercivity and thus reducing hysteresis loss; however, conventional insulation coatings suffer from the problem of their heat resistance not being high enough. The following outlines a heat resistant coating developed to solve this problem.

3.1 Experimental method

Three powder samples mainly consisting of pure iron powder, 300NH, were prepared. Each powder sample was coated with two layers, i.e., one inorganic layer and one organic layer. Each inorganic layer was formed from one of three phosphoric acid-based solutions (A, B or C) for insulation. The organic layer consists of silicone resin having heat resistance. The coated powder samples were compacted by die-wall lubricated compaction with a pressure of 980MPa into plate-shaped specimens, each having dimensions of 12.7mm × 31.8mm × 5mm. The compact specimens were annealed in a nitrogen atmosphere at a temperature in the range of 773 to 873K for 1.8ks. Their electrical resistivities were measured by a four-terminal method.

3.2 Results and discussion

The electrical resistivity of an insulation coating varies depending on the coating material, coating thickness and magnetic annealing temperature. These factors, determining the electrical resistivity of insulation coating, were changed to study the eddy current losses of samples with various electrical resistivities (**Fig. 4**). The result indicates that an electrical resistivity higher than about 100 $\mu\Omega\cdot$m effectively suppresses the inter-particle eddy current loss. It is thus concluded that the coating used for a dust core must have an electrical resistivity that causes the overall resistivity of the compact to be higher than about 100 $\mu\Omega\cdot$m.

Fig. 5 compares the dependence of electrical

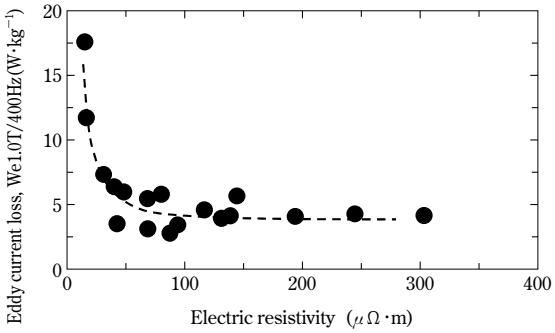

Fig. 4 Relationship of eddy current loss and electric resistivity

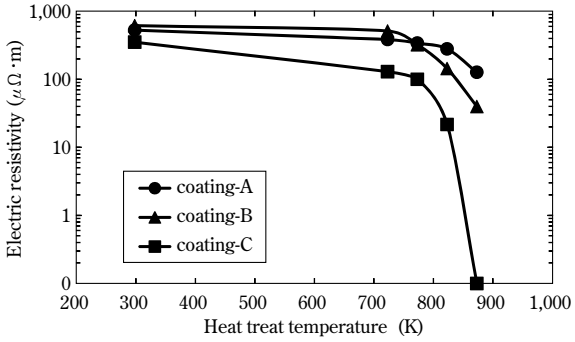

Fig. 5 Relationship between electric resistivity and annealing temperature

resistivities on the annealing temperature of powder compacts, each coated with two layers, one layer consisting of one of the three inorganic materials made from phosphoric acid solutions and the other layer consisting of silicone resin. All the coatings exhibit a decrease in electrical resistivity with rising annealing temperature. The decrease is considered to be due to the deterioration of the coatings. The two-layered coating, consisting of a layer of inorganic material (A) and a layer of silicone resin, exhibits a smaller decrease in electrical resistivity and has an electrical resistivity higher than 100 $\mu\Omega\cdot$m at an annealing temperature of 873K, the resistivity required at the optimum magnetic annealing temperature. There are reports on the improvement in heat resistance of inorganic coating made from a phosphoric acid-based solution. Such reports include one focusing on the vitrification temperature of coating[3] and another focusing on the diffusion of elements[4]. However, the cause of the high heat resistance of the two-layer coating, consisting of the inorganic layer (A) and silicone resin, as reported in this paper, requires further investigation.

Conventional insulation coatings have low heat resistance, limiting the magnetic annealing temperature to around 773K. The newly developed two-layered coating allows magnetic annealing at 873K, a temperature high enough for the strain relief of dust cores.

4. Effect of powder particle size and crystal grain size on iron loss

Studies were conducted on the effects of powder particle size and crystal grain size on iron loss. The powder particle size, in particular, affects both the hysteresis loss and eddy current loss. Thus, a study was conducted from the two aspects of hysteresis loss and eddy current loss. Also outlined is the relation between the powder particle size and crystal grain size, which are inseparably connected.

4.1 Experimental method

Pure iron powder, 300NH, was heat-treated in powder form. Each heat-treatment cycle was conducted in a nitrogen atmosphere at 1,243K for 5.4ks and the cycle was repeated three times to grow crystal grains. The resulting powder was sifted using sieves with mesh sizes of 180, 150, 100, 75, 63 and 45 μm. Powder samples were prepared with the finer particles removed sequentially, as described in 4.2. Each powder sample thus obtained was compacted into a ring-shaped specimen having a compact density of 7.60Mg/m^3 by die-wall lubricated compaction. Each compact specimen was annealed in a nitrogen atmosphere under one of two conditions, i.e., 823K for 1.8ks, or 873K for 1.8ks. The annealed specimens were measured for their direct current magnetic properties. Iron loss was measured by an automatic magnetic measurement apparatus (manufactured by Yokogawa Electric Corporation). The conditions for iron loss measurement were the excitation magnetic flux density, 1.5T, and excitation frequency, 200Hz.

4.2 Results and discussion

In a magnetic material, interfaces such as grain boundaries and powder surfaces provide sites for preventing domain wall migration. To study this behavior, pure iron powder was heat treated to grow its crystal grains. **Fig. 6** shows the cross-sectional micrographs of the powders before and after the heat treatment. The heat treatment has been shown to grow the crystal grains.

Fig. 7 compares the coercivities of the compacts of the powders before and after the heat treatment applied for crystal grain growth. The figure indicates that coercivity is decreased as a result of the grain growth.

After the grain growth heat treatment, the powder was sifted using sieves with mesh sizes of 180, 150, 100, 75, 63, 45 μm. Powder samples were prepared with finer particles removed sequentially. The size distribution width of the powder samples were A) 0 ～250 μm; B) 45～250 μm; C) 63～250 μm; D) 75～250 μm; E) 106～250 μm; F) 100～250 μm; and G) 180～250 μm. **Fig. 8** shows the coercivities of the compacts made from these powders. It has turned out that coercivity is effectively decreased by growing crystal grain and removing finer particles from the powder to increase the average particle size.

If all the powder particles become single crystals as a result of the powder heat treatment for crystal grain growth, no further increase in the average grain size is expected. Thus, finer particles serve to decrease coercivity. When removing finer particles by sieving, it is effective to remove particles smaller than the crystal grain size; however, fine crystals in coarse particles still inhibit the decrease in coercivity.

Thus, in order to decrease coercivity, it is important to combine the removal of fine particles (coarsening) and the growth of crystal grains.

It should be noted that increasing the particle size increases the intra-particle eddy current. Therefore, particle size should be selected by incorporating the

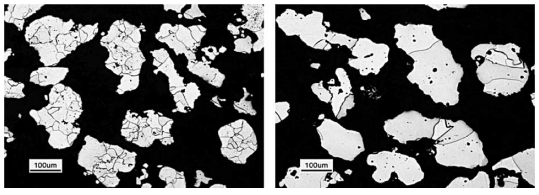

Fig. 6 Cross sectional microstructure of powder with(right) and without(left) grain growth treatment

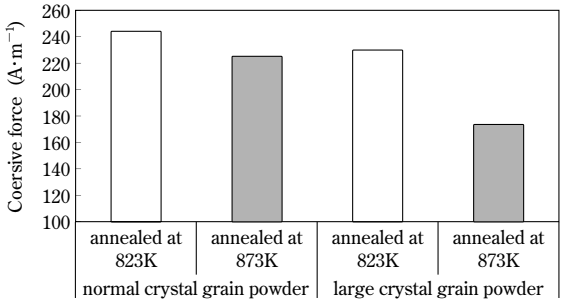

Fig. 7 Coersive force comparison of crystal grain size

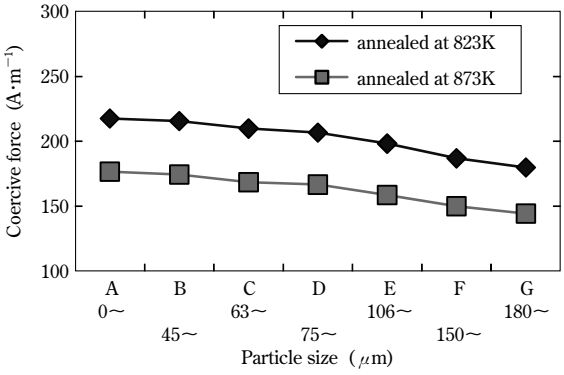

Fig. 8 Relationship of particle size and coersive force

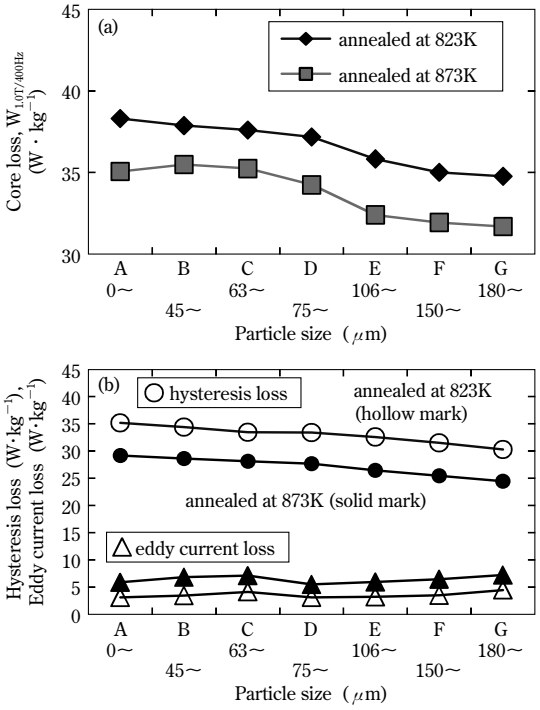

Fig. 9 Relationship between particle size and core loss(a), and between particle size and hysteresis, and eddy current loss(b)

decreasing effect of hysteresis loss and increasing effect of eddy current loss.

Fig. 9 (a) represents the iron losses of compacts made from iron powders with or without fine particles, and Fig. 9 (b) represents the respective iron loss, separated into hysteresis loss and eddy current loss. As shown in Fig. 9 (b), removing fine particles is effective in decreasing both coercivity and hysteresis loss and has a minimal effect in increasing eddy current loss within the particle size distribution investigated. Therefore, the iron loss shown in Fig. 9 (a) monotonically decreases as a result of removing fine particles.

5. Characteristics of newly developed iron powder with reduced iron loss

The following introduces the iron powder with reduced iron loss developed on the basis of the knowledge obtained.

To investigate the characteristics of compacts made from the newly developed powder, pure iron powder (i.e., starting material, 300NH), was classified using a sieve with 150 μm mesh openings to remove fine particles. The remaining coarse powder was treated to grow its crystal grains. The treated powder was coated by two-layer insulation, consisting of a phosphoric inorganic layer (A) and a silicone resin layer. This powder was heated to 403K, compacted by die-wall lubricated compaction at a pressure of 1,176MPa, and was annealed in a nitrogen atmosphere at 873K for 1.8ks to prepare the compact specimen.

The magnetic properties and iron losses of the specimens are shown in **Table 1** and **Fig.10**, respectively. Also shown for comparison are the characteristics of a conventional material and electrical steel sheets. The ring-shaped specimens for the electrical steels were prepared by wire cut. The conventional dust core in Fig.10 was made from 300NH with conventional insulation coating applied, after which it was annealed at 773K for 1.8ks.

The newly developed powder exhibits significantly reduced iron loss compared with the conventional materials. It shows reduced iron loss in the frequency range above 200 to 300Hz, compared with a conventional electrical steel sheet, JIS 50A400. It also shows reduced iron loss in the frequency range above 700～1kHz, compared with JIS 35A360. Thus the newly developed powder is expected to be used for applications such as motors that rotate at relatively high speed.

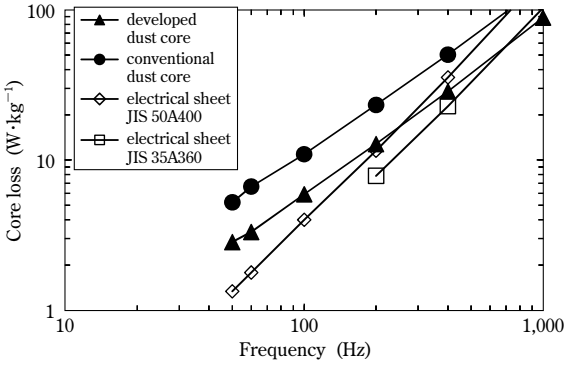

Fig.10 Comparison of core loss

Table 1 Properties of developed material

		size distribution (sieve size) (μm)	density (Mg/m^3)	heat treatment temperature (K)	flux density (@8,000A/m) (T)	maximum permeability	coersivity (A/m)	core loss (1.0T/400Hz) (W/kg)	transverse rupture strength (MPa)
dust core	developed	150～250	7.69	873	1.66	669	134	28.6	76
	conventional	0～250	7.61	823	1.58	446	243	50.4	82
electrical sheet	JIS 50A400	—	—	as cutted	1.8	6,213	60	35.5	—
	JIS 35A360	—	—	as cutted	1.79	6,532	59	22.9	—

Conclusion

As a means for decreasing coercivity and hysteresis loss, a new iron powder was developed focusing on magnetic annealing, powder particle size and crystal grain size. The following was found:

- The optimum magnetic annealing temperature for dust cores made from pure iron powder lies in the range from 873 to 973K. Annealing at temperatures above this range adversely increases coercivity. This is partially due to the refinement of crystal grains caused by recrystallization.
- An electrical resistivity higher than about 100 $\mu\Omega$·m is required to suppress the magnetic loss caused by inter-particle eddy current. An insulation coating was developed which maintains the required resistivity even after magnetic annealing at 873K. This coating has made it possible to decrease coercivity and, therefore, hysteresis loss.
- The effects of crystal grain size and powder particle size on the coercivities of compacts have been clarified. A significant reduction of coercivity is made possible by combining the size effects of crystal grains and powder particles, rather than controlling them independently.
- Combining the newly-developed heat-resistant insulation coating with crystal grain coarsening and particle coarsening (removal of fine particles) enable the production of a dust core having iron loss comparable with that obtained by conventional electrical steel sheets. Dust cores have the feature of being able to suppress eddy current loss at high frequencies. Thus, the newly developed powder can be used as a material with iron loss lower than that achieved by electrical steel sheet in the high-frequency range (several hundred Hz to 1kHz or above).

References

1) Lars Hultman et al., *Advances in Powder Metallurgy & Particulate Materials*, (2002), pp.14-26.
2) Y. Enomoto et al., *The transactions of the Institute of Electrical Engineers of Japan*, D, Vol.129, (2009), pp.1004-1010.
3) S. Tajima et al., *Journal of the Japan Society of Powder and Powder Metallurgy*, Vol.53, (2006), pp.290-296.
4) S. Tajima et al., *Journal of the Japan Society of Powder and Powder Metallurgy*, Vol.52, (2005), pp.164-170.

Overseas Deployment of Wire Rod & Bar Manufacturing and Wire Rod Secondary Processing

Goro AKAISHI*1, Noriaki HIRAGA*2
*1 Wire Rod & Bar Products Marketing & Technical Service Department, Iron & Steel Business (currently with Wire Rod Production Department, Kakogawa Works)
*2 Wire Rod & Bar Products Marketing & Technical Service Department, Iron & Steel Business

The demand for special steel wire rods and bars has been increasing as Japanese auto makers continually expand their overseas operations, increasing the local procurement of automotive parts. Kobe Steel now has a technical tie-up with two special steel mills in Europe and North America so that high quality wire rod and bar can be supplied to auto makers and parts makers. Kobe Steel has also constructed a system to provide for the secondary processing of wire rod products for Japanese parts makers, mainly by establishing secondary processing companies in Asia and North America.

Introduction

The automobile trade dispute between Japan and US caused Japanese automakers to accelerate their local auto production in North America, a major consumption area. This has led Japanese automakers to expand their manufacturing bases in other areas, such as Europe and Asia, where the demand for automobiles has been increasing. Some regions may have significance as operational bases for exporting because of low manufacturing costs. In 2009, the overseas production of Japanese automakers exceeded their domestic production[1] (**Fig. 1**). Many Japanese parts manufacturers have moved into North America, Southeast Asia and China and are expanding their on-site production against the backdrop of the rising yen.

Without a doubt, Japanese auto parts are supported by customized steel of consistent quality, as well as secondary processing products. For the overseas manufacturing bases, it has thus become increasingly important to ensure a stable supply of materials of the same quality as those delivered in Japan, using a similar delivery system.

This paper reports on Kobe Steel's overseas deployment of sites for fabricating wire rods and bars made of special steel. Also described is the deployment of overseas sites for secondary processing products.

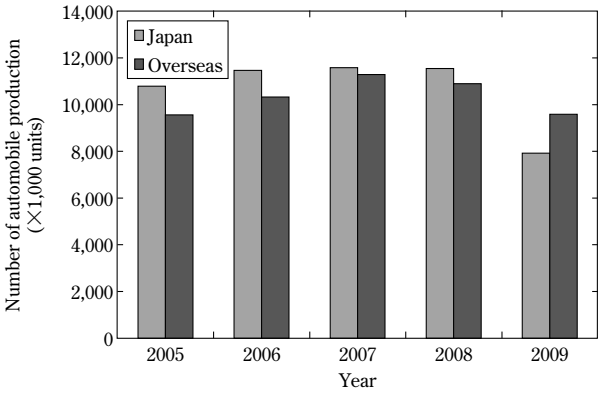

Fig. 1 Domestic and overseas automobile production by Japanese auto makers

1. Kobe Steel's approach toward establishing overseas production sites

Special steel wire rods and bars have a wide variety of applications. In general, they are used not only for parts such as bearings, springs and gears, which are subject to continuous dynamic load, but also for applications such as structural steel, which are used under static load but are exposed to severe cold work during the manufacturing process. In other words, the wire rods and bars must have high quality surfaces and interiors in response to the performance requirements for end products and manufacturing processes.

As described, many Japanese auto parts employ wire rods and bars made of customized special steels. Thus, the required qualities vary item by item. To meet these quality requirements, detailed and flexible management is needed; and to that end, the overseas production sites must have manufacturing and quality control, production planning and technical services comparable to what has been implemented in Japan. Kobe Steel proceeds with this implementation while keeping the following aspects in mind.

1.1 Business form

Even if made of special steel, steel bars are hot-forged as-is in many cases. In contrast, wire rods are cold-forged plastically into more near-net shapes, requiring a secondary process that gives the wire rods homogeneous structures and sizes suitable for cold forging. This make the role of secondary processing increasingly important.

Kobe Steel's overseas deployment depends on the type of product. The steel bars are made by local manufacturers of special steel with technical assistance agreements. On the other hand, secondary processing sites are established for wire rods. The

wire rods are either imported from Kobe Steel in Japan, or procured from special steel manufacturers who are located near the secondary processing sites and are under technical assistance agreements.

1.2 Manufacturing & quality control and production management

The impetus behind the need for item-by-item quality control is the downsizing and weight reduction of Japanese automobile parts, which require materials that have high strength and can withstand heavy working. In particular, parts that are subject to heavy cold working call for materials without defects. Thus, the local industry demands steel with no surface defects and no non-metallic inclusions near the surface, which are harmful to the quality. Also in demand is secondary processing that optimizes the microstructure for cold working. To meet these requirements, it is necessary to fully understand what is going on during the production processes and to implement detailed quality control; however, these are technologies supported by accumulated data and experience and are impossible to learn in a short time.

Thus, Kobe Steel focuses on selecting local special steel manufacturers with high technological competence, especially in quality control. Kobe Steel also takes the approach of stationing technical teams at special steel manufacturers equipped with first-class facilities.

Furthermore, Kobe Steel and secondary processing companies in close relationships with Kobe Steel, have jointly established firms to provide bases for secondary processing. These bases are provided with state-of-the-art facilities, as well as with engineers and managers who are stationed locally to transfer the technologies for production/quality control and to implement management know-how.

1.3 Technical service

It is extremely important to listen to customers' voices to understand how our products are being used and to determine if the customers are satisfied, or if they have any problems. Visual confirmation of the usability of the products is also important.

Determining how our products should be made through such continuous dialogue with customers is the most effective way of strengthening product competitiveness.

Kobe Steel deploys capable human resources to the bases and resident offices in charge of the various regions, where they collect relevant information so as to ensure smooth communication with customers, thus adding value to the products.

2. Deployment of manufacturing bases by regions

Kobe Steel currently has manufacturing bases at important locations in North America, Europe and Asia (**Fig. 2**) to respond to customers' needs.

The following describes the market trend and status of deployment in each region.

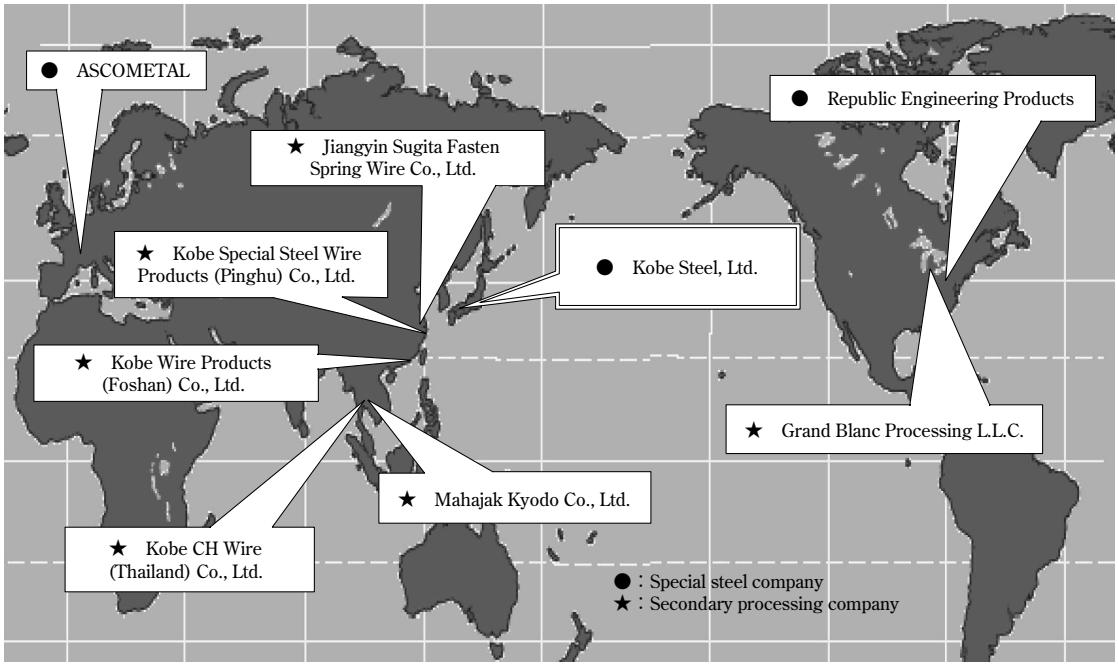

Fig. 2 Location of overseas special steel mill which have a technical tie-up with Kobe Steel and overseas secondary processing companies

2.1 North America

The automobile industry in North America was hit hard by the Lehman Shock in 2008. Two of the Big Three companies filed for protection under federal bankruptcy laws. In this environment, Japanese automakers have increased their market share, thanks to their cars featuring high fuel economy and requiring minimum maintenance[1] (**Fig. 3**).

Kobe Steel provides technical assistance to Republic Engineered Products (REP), Ohio, USA, for its production of special steel wire rods and bars and has licensed it to produce wire rods for suspension springs developed by Kobe Steel. Kobe Steel also has a base at Grand Blanc Processing L.L.C. (GBP), Michigan, USA, to produce steel wire for cold heading and for bearing parts such as balls, rollers and needles. Currently, both the steel products and secondary processing products are supplied not only to Japanese customers, but also to local consumers. The company outlines of REP and GBP are included in **Table 1** and **2**, respectively.

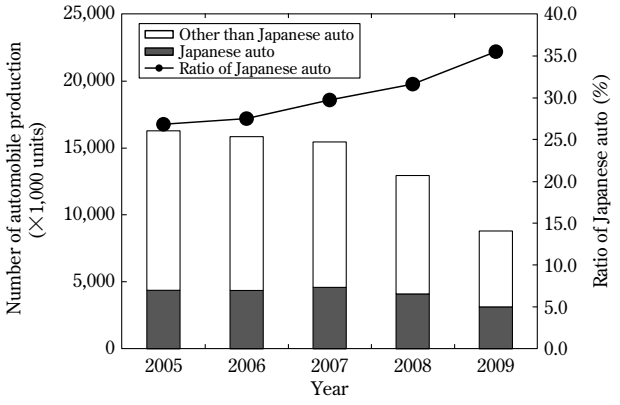

Fig. 3 Automobile production in North America

2.2 Europe

Many steel manufacturers in Europe exceed or even equal Japanese manufacturers in technological competence and management know-how. They are capable of independently producing special steel wire rods and bars with high quality, once they learn the Japanese method of quality control.

Kobe Steel and ASCOMETAL agreed on technical cooperation including a license exchange for producing steels developed by their respective

Table 1 Overseas technical tie-up mills and their outline

Company name	Republic Engineered Products			ASCOMETAL		
Head office	Lorain, OH, USA			Paris, France		
Tie-up year	1999			2002		
Main factory	Lorain	Canton	Lackawanna	Hagondange	Fos sur mer	Le Cheylas
Main facilities	Blast furnace Basic oxygen furnace LF Vacuum degassing Bloom CC Billet CC Billet inspection Bar mill Wire rod mill	Electric furnace LF Vacuum degassing Bloom CC Billet CC	Bar mill Bar inspection	Electric furnace LF Vacuum degassing Bloom CC Bar mill Bar inspection	Electric furnace LF Vacuum degassing Ingot casting Billet inspection Wire rod mill	Electric furnace LF Billet CC Bar mill Bar inspection

Table 2 Overseas wire rod secondary processing companies and their outline

Company Name	Grand Blanc Processing L.L.C. GPB	Mahajak Kyodo Co., Ltd. MKCL	Kobe CH Wire (Thailand) Co., Ltd. KCH	Kobe Wire Products (Foshan) Co., Ltd. KWPF	Jiangyin Sugita Fasten Spring Wire Co., Ltd. JYSF	Kobe Special Steel Wire Products (Pinghu) Co., Ltd. KSP
Place	Michigan, USA	Bangkok, Thailand	Bangkok, Thailand	Guangdong, People's Republic of China	Jiangyin, People's Republic of China	Pinghu, People's Republic of China
Nature of business	Secondary processing of CH & Bearing wire	Secondary processing and sales of cold finishing steel bar	Secondary processing and sales of CH wire	Secondary processing and sales of cold finishing steel bar and CH wire	Secondary processing and sales of oil tempered wire	Secondary processing and sales of CH wire
Establishment	1995 (invested in March 2003)	1996 (invested in February 2002)	1997	2004	2005	2007
Capital	US$ 16.8 million	THB 143 million	THB 103 million	JP¥ 725 million	JP¥ 760 million	JP¥ 1,200 million
Equity participation	20%	27.5%	30%	60%	60%	50%
Nominal capacity	6,000 t/month	1,800 t/month	3,000 t/month	750 t/month for cold finishing bar 650 t/month for CH wire	600 t/month	2,100 t/month
Main facility	Pickling & coating: 1 unit Continuous furnace: 2 units STC furnace: 1 unit Drawing machine: 5 units Eddy current tester: 1 unit	Combined drawing machine: Type Ⅰ 1 unit Combined drawing machine: Type Ⅱ 2 units Eddy current tester: 2 units Straightener: 1 unit Cutting machine: 3 units	Pickling & coating: 2 units Shot-blasting: 1 unit Batch type furnace: 5 units STC furnaces: 4 units Drawing machine: 9 units	Pickling & coating: 1 unit Combined drawing machine with eddy current tester: 2 units Drawing machine: 3 units	Pickling & coating: 1 unit Drawing machine with eddy current tester: 1 unit oil tempered equipment: 1 unit	Pickling & coating: 1 unit STC furnaces: 2 units Drawing machine: 3 units

companies and have implemented joint development activities to produce special steel such as that used in suspension springs. Kobe Steel also provides technical guidance to establish the management know-how required for the supply bases providing special steel to Japanese automakers in Europe. The profile of ASCOMETAL is included in Table 1.

2.3 ASEAN

The annual production of automobiles in Thailand exceeded one million in 2005[1] (**Fig. 4**). The country, now dubbed the "Detroit of Asia", has become a manufacturing base with a concentration of automakers and parts manufacturers. Worthy of special mention is that Japanese cars occupy more than 90% of the automobiles produced there and the country is positioned as a huge base of operations for exporting automobiles and auto parts to other countries in Southeast Asia, the Middle East and the Southern Hemisphere.

The eco-car project proposed by the Thai government in 2007 was temporarily put on ice in the aftermath of the Lehman Shock; however, with economic recovery, Japanese automakers, in particular, began to announce plans to exploit the program and produce compact cars. Kobe Steel's contribution to the growth of the auto industry in Thailand includes the establishment, in the late 1990s, of Kobe CH Wire (Thailand) Co., Ltd., a production base for wire rods for cold heading, and Mahajak Kyodo Co., Ltd., which produces bright steel bars, a major material for hot-coiled suspension springs. The outlines of these two companies are included in Table 2.

2.4 China

China is one of the few countries to have experienced ever-increasing economic growth, despite a brief stagnation after the Lehman Shock. The country, which has been called "the world's factory,"

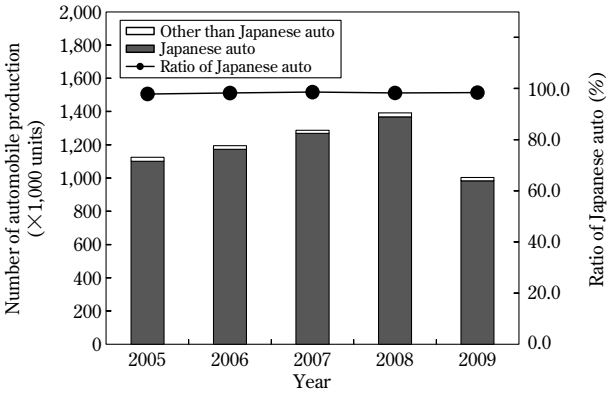

Fig. 4 Automobile production in Thailand

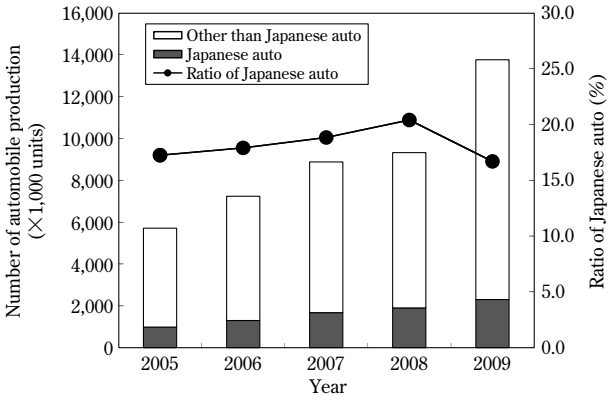

Fig. 5 Automobile production in China

has not only remained, but continued to grow as a big consumer. Now it is fair to say that no industry can get along without China, which has overtaken Japan to become an economic super power that has the second largest GDP in the world.

China overtook the US as the world's largest auto-making country in 2009[1] (**Fig. 5**). Major automakers of the world have established manufacturing bases there, with some manufacturers producing more in China than they do in their own countries. New local manufacturers are growing rapidly. Japanese and European component manufacturers are moving in one after another, increasing the demand for wire rods and bars made of special steel.

With this background, Kobe Steel has established three bases for wire rod fabrication since 2004 and has built a structure for producing and supplying wires for cold heading, bright steel bars for hot-coiled suspension springs and oil-tempered wires for cold-coiled suspension springs. Kobe Wire Products (Foshan) Co., Ltd. was established in Guangzhou, a major production center for Japanese automakers. Jiangyin Sugita Fasten Spring Wire Co., Ltd. and Kobe Special Steel Wire Products (Pinghu) Co., Ltd. were established in the suburbs of Shanghai, where there is a concentration of many component manufacturers. Kobe Steel thus has built a system for the widespread supplying of secondary processing products of wire rods to major auto production sites in China. The outlines of these three companies are included in Table 2.

Conclusions

In response to the demand for customized steel with consistent quality and secondary processing products from Japanese automakers overseas, Kobe Steel has established manufacturing bases in North America, Europe, Thailand and China. These secondary processing bases for wire rods will continue to be used, despite the trend toward

reexamining standard steel with a view to cost reduction. Kobe Steel will expand its capacity to meet demands in a timely manner and strive to build a system to satisfy customers by working with its partners to improve the management skills of local staffs in production and quality control.

References

1) FOURIN, *FOURIN Monthly Report on the Global Automotive Industry (FY 2005 to 2009)*.

Development History of Wire Rods for Valve Springs

Nao YOSHIHARA*1
*1 Wire Rod & Bar Products Development Department, Research & Development Laboratory, Iron & Steel Business

To reduce fuel consumption, automotive valve springs need to be made lighter. Kobe Steel has developed high strength steel for valve springs to meet this requirement. Furthermore, by continuously developing technology for the control of internal defects, such as non-metallic inclusions, high strength valve spring steels with good robust quality have been provided. This paper describes the development history of wire rods for valve springs with high fatigue strength.

Introduction

Valve springs (**Fig. 1**) are used in the valve actuation mechanisms of internal-combustion engines. A valve spring serves to move an intake, or an exhaust, valve according to the head-discharge curve of a cam such that the valve is in contact with its seat to prevent compression leakage. In the meantime, a valve spring is required to impose appropriate tension on the valve so as not to increase the friction loss of the valve operating system. The environmental regulations for automobiles are becoming more stringent in order to further reduce CO_2 emissions. To achieve this and to improve fuel economy, valve springs are required to be lighter and smaller. Such downsizing improves followability with cams, reduces the inertia weight of valve operating systems, and helps to reduce the size of engines. However, as valve springs become lighter and smaller, more stress is imposed on spring wires. In addition, the spring wires must withstand repeated loading at a frequency of several thousand cycles per minute for extended periods of time. Furthermore, aging degradation can cause shortening of the spring, a phenomenon called "sag"; hence valve springs are also required to have improved sag resistance under high stress. Until the late 1970s, valve springs had been made of hard-drawn wire of high carbon steel having a tensile strength of about 1,700MPa. Then oil-tempered wires of 1,900MPa grade began to be used. Nowadays, oil-tempered wires of 2,100~2,200MPa grade are commonly used[1), 2)]. Furthermore, nitriding treatment is being applied to the surfaces of wires to increase durability (**Fig. 2**).

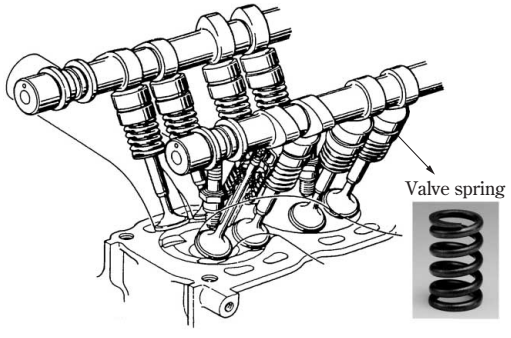

Fig. 1 Valve spring in automobile engine

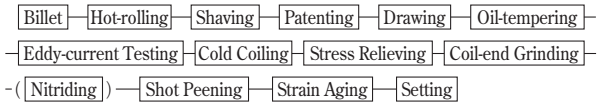

Fig. 2 Manufacturing process of valve spring

This paper introduces Kobe Steel's history of strengthening valve spring steel and newly developed materials.

1. Strengthening of valve spring steel at Kobe Steel

1.1 History of strengthening steel for valve springs

Wires used for valve springs include piano wires (i.e., as-drawn high-carbon steel wires) and oil-tempered wires (i.e., wires that are drawn, oil-quenched and tempered).

Until World War II, piano wires had been made in Sweden. Kobe Steel started producing wire rods made of high carbon steel in 1930. The company successfully developed wire rod for valve springs and inaugurated the production of piano wires for valve springs in 1941. Around that time, the piano wires were first used for the valve springs of aircraft engines and then started to be used for the valve springs of automobile engines[3)]. In 1952, Kobe Steel succeeded in developing a wire rod (KPR: Kobe Piano Wire Rod) that was comparable with Swedish steel[4)].

After the war, oil-tempered wires were introduced from the USA. In 1955, Kobe Steel began producing oil-tempered wires of carbon steel and also of Cr-V. These wires gradually came to be used in automobile engines[5)].

Since around 1964, wires with excellent heat resistance (SAE9254, JIS SWOSC-V), made of oil-tempered steel containing Si and Cr, have been used to increase fatigue strength and improve sag

resistance. This steel has become a de facto standard.

Table 1 shows the chemical compositions of wire rods used for valve springs, i.e., the compositions specified by SAE (SAE steels) and the ones developed by Kobe Steel. **Fig. 3** depicts the development trend of the wire rods. Kobe Steel's technologies include techniques for reducing surface scratches and decarburized layers, both of which can adversely affect the fatigue strength of oil-tempered wires, and a method[6] for peeling the wire rod surface over its entire length. In the early 1980s, the company developed and implemented technologies[7] for evaluating and cleaning off harmful inclusions. Adopting this technology to the SAE9254 steel has significantly improved the fatigue strength of valve springs.

Studies have been conducted aiming at optimizing chemical compositions for higher strength. In the mid-1980s, a new composition, KHV7, was developed and implemented. This composition was based on SAE9254 and has a higher content of C for increased tensile strength and an additional content of V, which refines austenitic grain and improves softening resistance. Oil-tempered wires of SAE9254 have a tensile strength of about 1,900MPa, while those of KHV7 have a tensile strength around 2,050MPa. The developed steel has an increased fatigue strength that is about 1.1 times higher than that of the conventional SAE9254. Furthermore, applying nitriding treatment has increased the fatigue strength by a factor of about 1.3.

In the early 1990s, a new alloy, KHV10N, containing 2.0% of Si, was developed to increase resistance against temper softening. This steel has raised the tensile strength of oil-tempered wires to the 2,200MPa level. Combined with nitriding treatment and modified shot peening, KHV10N has achieved a fatigue strength about 1.4 times higher than that of SAE9254.

To further improve the fatigue strength and sag resistance of KHV10N, larger amounts of Cr and V were added to make the crystal grains ultrafine. The developed alloy, KHV12N, was commercialized in 2006.

Fig. 4 shows the ratio of high and super-high strength steels occupying the valve spring steels produced by Kobe Steel. In recent years, the adoption of high-strength steel has been increasing rapidly. High-strength steel currently accounts for about 60 percent of the valve spring steel shipped by Kobe Steel, and this rate is expected to increase.

1.2 Means for strengthening

Assuming no defect, the following relationship[8] generally exists between the fatigue limit, σ_w, and Vickers hardness, HV:

$$\sigma_w = 1.6HV \quad \cdots\cdots(1)$$

wherein the units are in MPa for σ_w and kgf/mm^2 for HV.

Table 1 Chemical compositions of wire rod for valve spring

(mass%)

Steel grade		C	Si	Mn	Ni	Cr	V
KHV12N	Ultra high tensile	0.60	2.15	0.45	0.20	1.75	0.27
KHV10N	Super high tensile	0.58	2.00	0.85	0.30	0.95	0.10
KHV7	High tensile	0.62	1.45	0.60	—	0.60	0.12
SAE9254	SWOSC-V	0.55	1.40	0.65	—	0.65	—
SAE6150	SWOSV-V	0.50	0.25	0.80	—	0.95	0.20
SAE1070	SWO-V	0.70	0.25	0.80	—	—	—

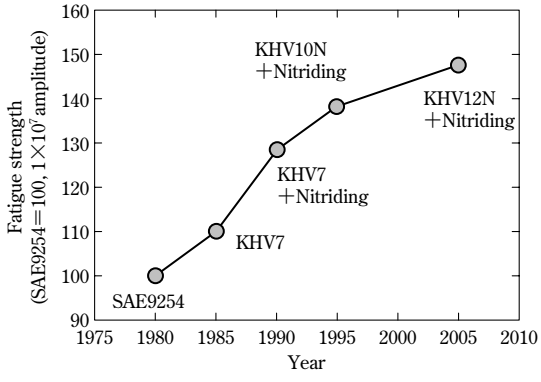

Fig. 3 Trend of high strength steel grades for valve spring in KOBE STEEL

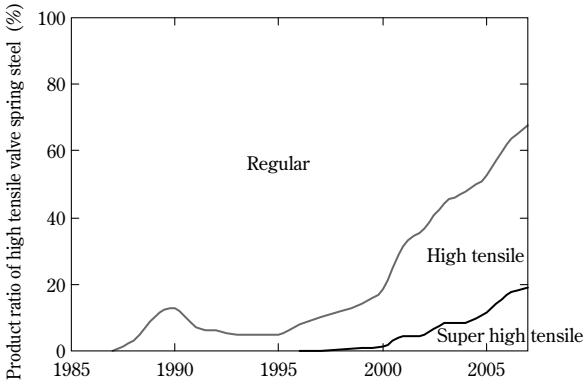

Fig. 4 Product ratio of valve spring steel grades in KOBE STEEL

Valve springs for automobile engines are used over an extended period of time in a severe environment of high temperature and high stress. In such an environment, a non-metallic inclusion larger than about 10μm can initiate fatigue fracture.

Murakami estimated the fatigue limit, σ_w, when internal defects such as inclusions were present, as follows[8].

$$\sigma_w = \frac{1.56(HV+120)}{(area)^{1/2}} \cdot \left[\frac{(1-R)}{2}\right]^{\alpha} \quad \cdots\cdots\cdots\cdots\cdots\cdots(2),$$

where $R=(\sigma_m-\sigma_a)/(\sigma_m+\sigma_a)$,

$\alpha=0.226+HV\times10^{-4}$,

$area$: Area of defect [μm^2],

σ_m: Mean stress [MPa],

σ_a: Stress amplitude [MPa],

in which the units are in MPa for σ_w and kgf/mm^2 for HV

According to this formula, hardness must be increased and the defect size decreased to improve fatigue strength. A conventional method of improving fatigue strength is to increase the strength of wire by oil tempering; however, when the tensile strength exceeds 1,800MPa, fracture is initiated at non-metallic inclusions, causing the fatigue strength to vary[1] as shown in **Fig. 5**. Thus, there is a limit to improving fatigue strength by increasing the tensile strength of wires. To overcome this issue, several approaches have been undertaken, such as increasing surface hardness by nitriding treatment and applying compressive residual stress by shot peening. Compressive residual stress can be treated as mean stress that reduces the effective stress.

Sag resistance, on the other hand, can effectively be improved by increasing the tensile strength (internal hardness) of spring wires[9].

The following outlines the treatment and technology for strengthening.

1.2.1 Nitriding treatment

Nitriding treatment is generally applied at a temperature from 400 to 600℃. This treatment hardens the surface layers of springs, increases compressive residual stress and significantly improves fatigue strength. However, the treatment reduces internal hardness, making it difficult to satisfy both fatigue strength and sag resistance at the same time. To resolve this issue, oil-tempered wires with softening resistance are very important.

1.2.2 Shot peening treatment

Shot peening is effective in improving the fatigue strength of parts such as valve springs. This treatment increases the compressive residual stress and hardness of the treated surfaces so as to increase fatigue strength. Multi-stage shot peening has been employed for increasing the fatigue strength[10]. Methods reported more recently include fine shot peening to improve residual stress[11), 12)] and enhanced shot peening for nano-sizing surface crystals to improve fatigue strength[13]. These shot peening technologies should be combined with other surface modification technologies to achieve further strengthening.

1.2.3 Inclusion control technology

Non-metallic inclusions, which mainly consist of SiO_2, can cause breakage of valve springs. These non-metallic inclusions are rendered harmless by lowering their melting point by controlling their compositions in the direction indicated by the arrow[2] in **Fig. 6**.

To control the composition in the direction of

Material	Initiation of Fracture		Chemical Compositions (wt%)				
	Inclusion	Surface	C	Si	Mn	Cr	V
Si-Cr Steel	●	○	0.55	1.40	0.70	0.70	—
Cr-V Steel	▲	△	0.67	0.25	0.75	0.50	0.20
Plain Carbon Steel	—	□	0.82	0.25	0.45	—	—

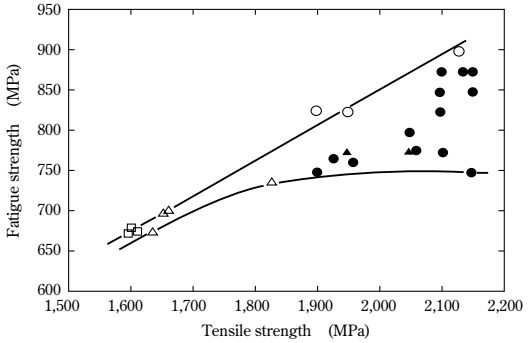

Fig. 5 Effect of tensile strength of steel wire for valve spring on fatigue strength

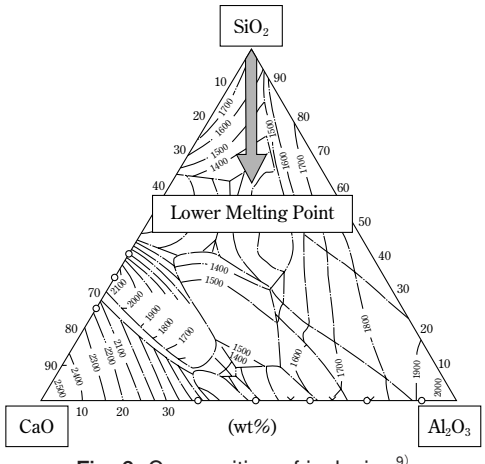

Fig. 6 Composition of inclusion[9]

the arrow, the processing parameters, such as slag basicity during secondary melting, must be controlled more accurately.

2. Characteristics of ultra-high strength wire rod for valve springs

Kobe Steel developed, and commercialized in 2006, an ultra-high strength wire rod, KHV12N, for valve springs; this wire rod has the world's highest fatigue strength. This chapter introduces the characteristics of KHV12N.

2.1 Concept of composition design

To improve the nitriding property and refine crystal grains, larger amounts of Cr and V are added than was the case with the previously developed KHV10N. In addition, an increased amount of Si was added to improve temper softening resistance in order to prevent a reduction in internal hardness during nitriding treatment and thus to enhance sag resistance.

2.2 Characteristics of oil-tempered wires

Table 2 shows the mechanical properties and grain size numbers of oil-tempered wires. An ultrafine grain structure (austenite grain size number 14) was obtained for KHV12N. This oil-tempered wire was subjected to low temperature annealing for 20 minutes for stress relieving after cooling. **Fig. 7** shows the mechanical properties after annealing at different temperatures. KHV12N exhibits improved softening resistance and less strength reduction at elevated temperatures even when compared with another high-strength valve spring wire, KHV10N.

2.3 Fatigue characteristics of springs

Fig. 8 shows the fatigue and sag characteristics of springs made of three different wires. Nitrided KHV12N exhibits a fatigue strength about 1.6 times higher than that achieved by SAE9254. This enables the spring weight to be almost halved. **Fig. 9** shows an example of a spring made of KHV12N.

Fig.10 shows the sag resistances of springs made of various materials. KHV12N exhibits the highest resistance against sag. The austenitic grain size number turns out to correlate well with the tensile strength of spring wires. The sag for KHV12N is decreased by about 60% compared with that for SAE9254, and by about 20% compared with that for KHV10N. This is regarded as attributable to the refinement of crystal grains. **Fig.11** shows the

Table 2 Properties of oil-tempered wire

	Tensile strength [MPa]	Reduction of area [%]	γ grain size No.
KHV12N	2,157	46.4	14.0
KHV10N	2,155	52.4	12.0

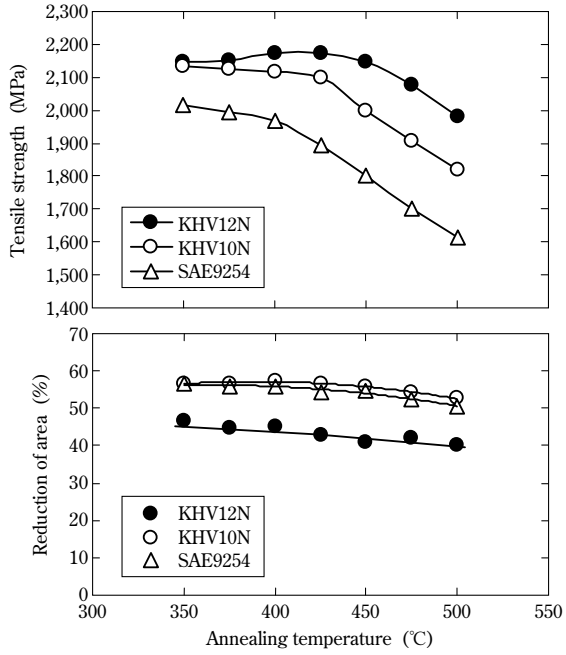

Fig. 7 Relationship between annealing temperature and mechanical properties

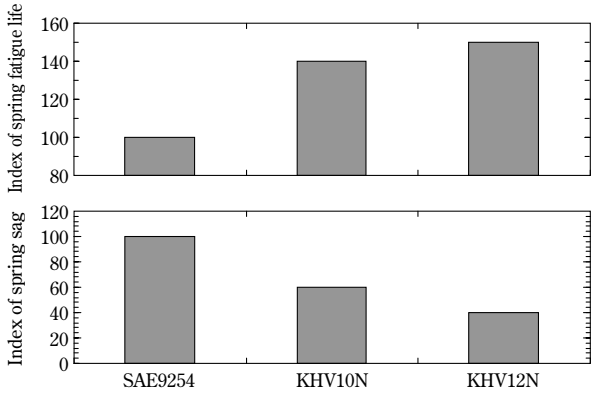

Fig. 8 Fatigue life and sag index of high-tensile valve spring

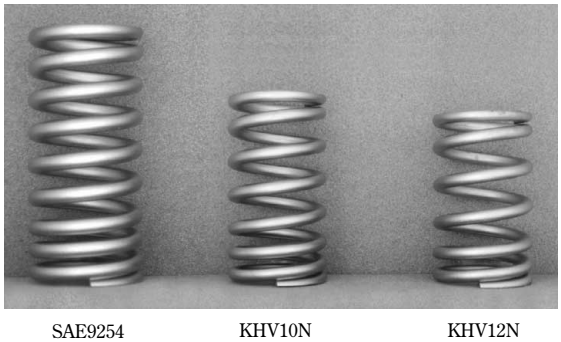

Fig. 9 Comparison of valve spring height

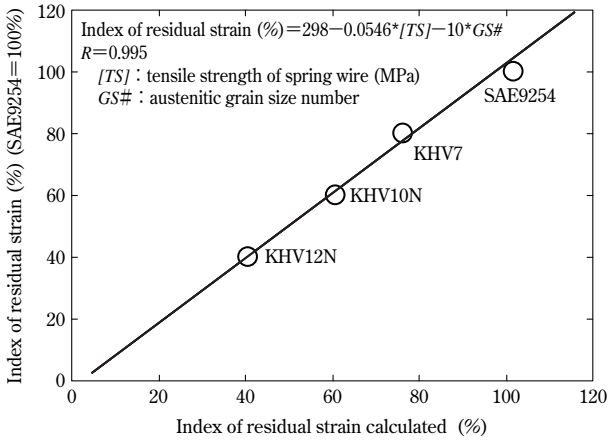

Fig.10 Sag resistance with a function of tensile strength and austenitic grain size number

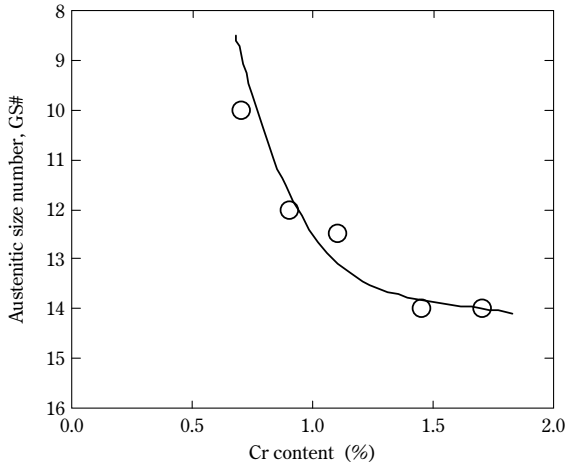

Fig.11 Relationship between austenitic grain size number and Cr content

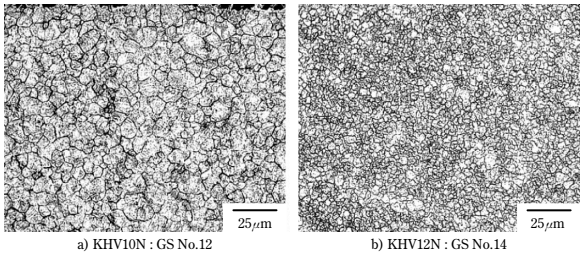

Fig.12 Etched austenitic grain of ultra-high tensile valve spring

relationship between the amount of Cr added and grain size. **Fig.12** are micrographs of KHV12N and KHV10N after grain boundary etching. The increased amount of Cr added in KHV12N improves the thermal stability of carbide, making the carbide more effective in preventing crystal grains from coarsening. Furthermore, the increased addition of V increases the amount of carbide containing V, enabling the ultra-refinement represented by grain size number 14. These are considered to be the reasons for the improved sag resistance.

Conclusions

Kobe Steel developed wire rods for valve springs earlier than any other company and has supplied them to the market. The wire rods are characterized by good robust quality and high strength, which enable the steel to be used under high stress. After 2015, the production volume of hybrid vehicles (HV) using both gasoline engines and electric motors is expected to increase rapidly. Kobe Steel's high strength wire rods for valve springs, including the ultra-high strength series, are effective in downsizing HV engines and in improving the fuel economy of gasoline engines. Kobe Steel will strive to contribute to the growth of the automobile industry and help to resolve global environmental problems.

References

1) N. Ibaraki, *R&D KOBE STEEL ENGINEERING REPORTS*, Vol.50, No.3(2000), p.7.
2) N. Yoshihara et al., *Transactions of Japan Society of Spring Engineers*, No.45(2000), p.15.
3) Japan Spring Manufacturers Association, *History of Springs in Japan* (1984), p.173.
4) K. Urakawa, *R&D KOBE STEEL ENGINEERING REPORTS*, Vol.18, No.4(1968), p.29.
5) Japan Wire Production Association, *SENZAI DOKUHON* (rev. 3), 1980, p.170.
6) Y. Nakamura et al., *R&D KOBE STEEL ENGINEERING REPORTS*, Vol.24, No.1(1974), p.115.
7) T. Ohshiro et al., *Stahl und Eisen*, 109(1989), Nr.21, p.1011.
8) Y. Murakami, *Effect of Micro-defects and inclusions*, YOKENDO Ltd. (1993), p.90.
9) S. Suda et al., *R&D KOBE STEEL ENGINEERING REPORTS*, Vol.55, No.2(2005), p.22.
10) H. Toshino et al., *Transactions of Japan Society of Spring Engineers*, No.32(1987), p.31.
11) Y. Yamada et al., *SAE paper* 2000-01-0791.
12) Y. Yamada et al., *SAE paper* 2003-01-1312.
13) H. Mano et al., *Transactions of Japan Society for Spring Research*, Autumn 2003, p.23.

Development Trends of Soft Magnetic Iron

Dr. Masamichi CHIBA*1
*1 Wire Rod & Bar Products Development Department, Research & Development Laboratory, Iron & Steel Business

Driven by advances in electronically controlled systems for automobiles, the demand is growing for soft magnetic steels that can generate a large electromagnetic force with low electric power. New steels with very low carbon content have been developed in consideration of their DC electromagnetic properties, their cold forgeability, and machinability. This paper describes the recent development trends of soft magnetic steel and the advantages of our developed steel (ELCH2 series).

Introduction

Recently automobiles are being heavily equipped with various systems operated electrically, electronically and/or electromagnetically to ensure safety, comfort and fuel economy. Such systems include computer controlled automatic transmissions, electronic power steering (EPS) and anti-lock braking systems (ABS)[1), 2)].

In the early years (1950s-1960s) when electric and electronic devices started to be used in automobiles, the main purpose was to improve and upgrade the performance of individual systems. Highly complicated vehicle control in recent years, however, is incomplete without high-speed linkage and movements coordinated among different systems. Hence electronically and/or electromagnetically controlled components are becoming increasingly important.

Among these electronically and/or electromagnetically controlled systems, components that utilize electromagnetic force incorporate iron cores in their coils to generate magnetic fields. Many conventional cores consist of low carbon steel, containing about 0.1% of carbon, to improve the response to control signals and increase energy efficiency.[3)] With the remarkable advancement of electromagnetic control in recent years, it has become essential for electromagnetic components to have even higher performance and lower power consumption.

This paper describes the trend of soft magnetic materials, such as those for iron cores used in electromagnetic components, and introduces the characteristics of the pure iron-based soft magnetic materials in the ELCH2 (Extra Low Carbon Cold Heading Wire) series developed by Kobe Steel.

1. Transition of soft magnetic materials

Fig. 1 depicts the structure of a solenoid device for hydraulic control. This is a typical example of the electromagnetic components used in automobiles. Soft magnetic materials are usually used for iron cores that form magnetic circuits and for the housings, including covers.

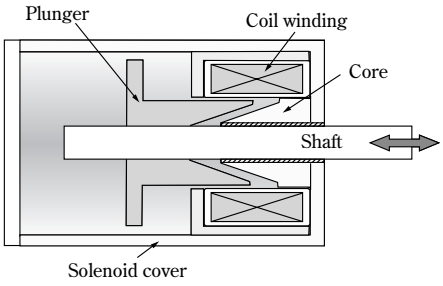

Fig. 1 Example of solenoid structure

Early solenoid devices for automobiles were mainly used for controlling the oil flow by on-off switching. Thus, the availability and workability of iron core materials were more important than their magnetic characteristics. As a result, low carbon steels such as SWRCH10A (JIS G 3507-1) and SUM23 (JIS G 4804) were used for the iron cores.

Recent solenoid devices, however, must be able to control hydraulics swiftly and stably. To achieve this, the on-off control is being replaced by linear control in many cases.[4), 5)] For linear control, the control current must be proportional to the pulling force (electromagnetic force) of the iron cores, which necessitates soft magnetic materials having low coercivity (low hysteresis) at high flux density. The latest iron core materials for linear solenoids are required to have magnetic characteristics better than those of SUY-1 (JIS C 2504), making it difficult for low carbon steel, formerly used for on-off control, to satisfy the required characteristics of magnetic flux density and coercivity (**Fig. 2**).

In the mid-1980s, Kobe Steel worked to totally eliminate factors that can adversely affect the magnetic characteristics of soft magnetic materials and developed a soft magnetic material, ELCH2, based on pure iron, which can achieve the best characteristics among JIS grade (JIS SUY-0) materials.[6)] The company has studied parts forming using a forging process and parts function. Now this material is being widely used as a soft magnetic material for cold forging.

In the late 1990s, there was an increasing need for

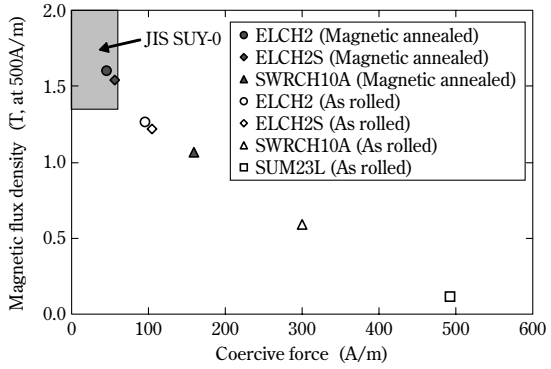

Fig. 2 Comparison of magnetic properties

parts having more complex shapes and higher accuracy. This required machining after cold forging, increasing the importance of the machinability of soft magnetic materials. Pure iron based materials have excellent magnetic characteristics, but they are more difficult to machine than is carbon steel, due to factors such as chip handling during machining and decreased tool life. To resolve this issue, a small amount of Pb was added to the materials.[7] However, Pb is a substance with a heavy environmental burden, hence forming parts without Pb has become an important issue.

Kobe Steel studied techniques to improve machinability without sacrificing magnetic characteristics and developed, in 2001, a new Pb-free steel with improved machinability, ELCH2S.[8] The commercial production of iron cores of large electromagnetic clutches started in 2004. The newly developed material, as well as the previously developed basic steel, is used for many automotive electromagnetic systems with high-functionality.

2. Concept of developed steel

The magnetic characteristics of a soft magnetic material depend on the magnetic moment of the material, as well as its metallic structure, including the size of crystal grains and precipitates. In the case of a polycrystal, in particular, its magnetic characteristics may deteriorate because of its crystal grain boundaries and precipitates, both working as pinning sites of domain walls.[9]

Therefore, the magnetic characteristics of the ELCH2 series have been improved along the following lines:

i) Making the structure a single phase of highly pure ferrite to increase the magnetic moment of the material, or reducing C content to no higher than 0.01% (**Fig. 3**)

ii) Decreasing the grain boundary area to reduce resistance against domain wall migration, or reducing Al and N content

Furthermore, the following aspects were considered, taking into account the fact that metallic soft magnetic materials have the advantage of superior workability and high productivity:

iii) Improving cold forgeability by reducing Si and adding Mn to render S harmless

iv) Improving the machinability of ELCH2S by increasing S to disperse an appropriate amount of MnS

Fig. 4 shows the relationship between the amount of S added to ultra-low carbon steel and tool wear width during turn cutting. It is expected that by increasing the S content to about 0.025%, the tool wear width will be decreased by half compared with the conventional pure iron based material containing less than 0.010% of S.

However, as shown in **Fig. 5**, an excessive addition of S deteriorates magnetic characteristics significantly, while increasing the width of variation in coercive force. Precipitation of FeS is observed at prior austenite grain boundaries.[8] This indicates that the deterioration of magnetic characteristics is attributable to FeS, which decreases the compression ratio of ferrite phase determining magnetic moment and increases the resistance against domain wall migration. Because of this, the newly developed steel

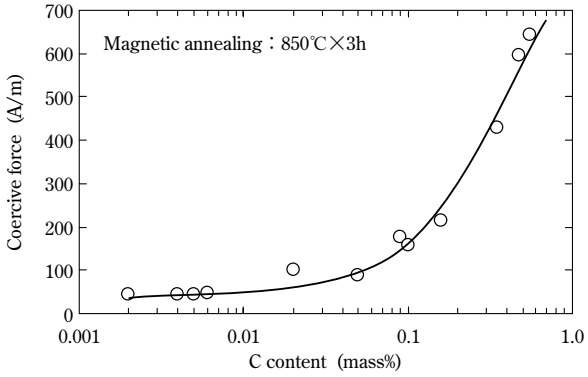

Fig. 3 C content dependence of coercive force

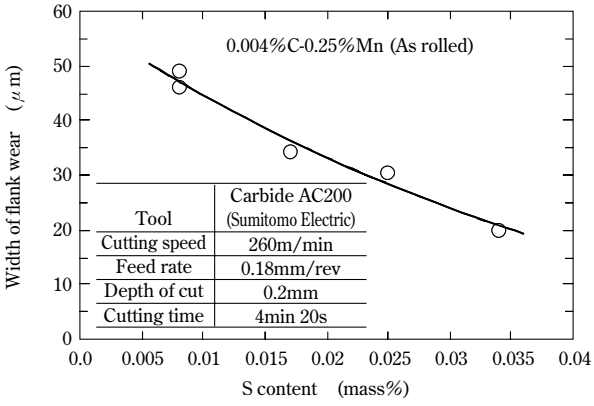

Fig. 4 Relation between S content and width of flank wear

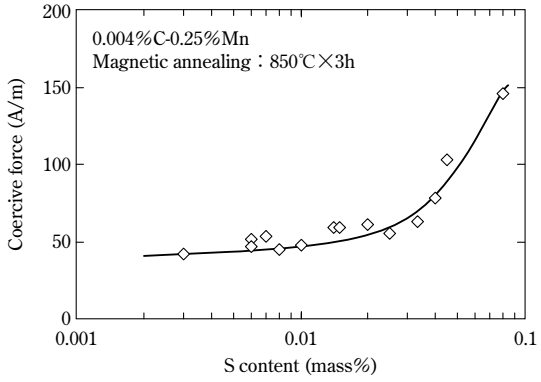

Fig. 5 S content dependence of coercive force

with improved machinability, ELCH2S, is designed to have an optimum Mn/S ratio, such that no FeS phase remains with increased S.

3. Specimens and experimental method

Table 1 shows the chemical compositions of steels that were studied: i.e., ELCH2 as a base composition, ELCH2S with improved machinability and SWRCH10A as a reference composition. These tested materials were melted in a converter furnace and rolled into wire rods, each having a diameter of ϕ20mm. The rolled materials were evaluated for their direct current magnetic characteristics, mechanical properties, machinability and corrosion resistance.

3.1 Magnetic characteristics

Magnetic characteristics were evaluated on ring-shaped specimens made of the respective test materials. The evaluation was conducted according to JIS C 2504 (Soft magnetic iron). An automatic magnetometer (BHS-40, manufactured by Riken Denshi Co., Ltd.) was used to obtain an initial magnetization curve and hysteresis curve, and these curves were used to determine coercivity and magnetic permeability. Also determined was the magnetic flux density under each magnetic field. It should be noted that the sweep rate (200~250(A/ms)) of the applied magnetic field during each measurement was set within a range in which eddy-current loss does not affect the hysteresis curve.

3.2 Mechanical properties

Mechanical properties were evaluated by tensile testing at room temperature. Tensile test pieces, 14 A according to JIS Z 2201 (Tensile Test for Metallic Materials), were prepared from the respective sample materials.

Table 1 Chemical composition of steels used in this study

(mass%)

Steel	C	Si	Mn	P	S
ELCH2S	0.005	0.004	0.26	0.010	0.025
ELCH2	0.005	0.004	0.25	0.009	0.008
SWRCH10A	0.10	0.04	0.45	0.014	0.009
JIS SUY	max. 0.03	max. 0.20	max. 0.50	max. 0.03	max. 0.03

3.3 Cold forgeability (deformability)

Deformability of the developed steel was evaluated on specimens (ϕ20×30mm), each having a notch on its lateral face. An upsetting test was conducted using a mechanical press while restraining the ends of each specimen. Deformability was determined from the critical upsetting ratio at which no cracking occurs from the notch.

3.4 Machinability

Machinability (i.e., burr height, chip disruption and wear width of cutting tool) was evaluated by a drill penetration test and cutting test using a carbide tool.

3.5 Corrosion resistance

Corrosion resistance was evaluated by the salt spray test according to JIS Z 2371 (salt spray test method), using 5% brine water. After the salt spray, the specimens were immersed in a 10% solution of ammonium citrate at 70℃ for rust removal before measuring the mass change.

4. Experiment results and discussion

4.1 Magnetic characteristics

Fig. 6 shows the relationship between the strength of the applied magnetic field and magnetic flux density for ELCH2 series steels and SWRCH10A. The tested materials had been annealed in a vacuum at 850℃ for 3 hrs. This magnetic annealing condition is widely used in the industry.

The ELCH2 series steels exhibit higher magnetic flux density for a given applied magnetic field compared with the reference steel, showing significant improvement for the magnetic field below 2,000A/m. The improvement effect seen in flux density lessens with a higher magnetic field. This is because, as magnetization approaches saturation, the magnetization mechanism shifts from domain wall migration to rotation magnetization, decreasing the effect of domain wall migration governed by metallic structure.

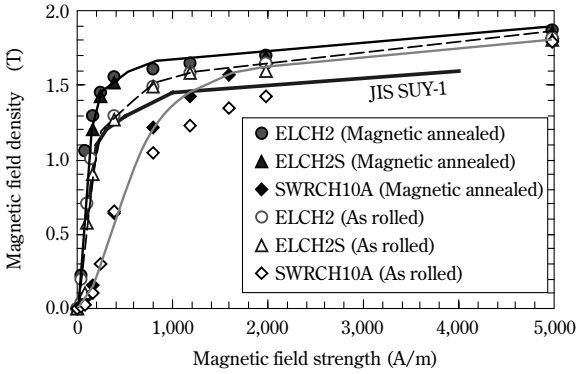

Fig. 6 Magnetic field dependence of magnetic flux density

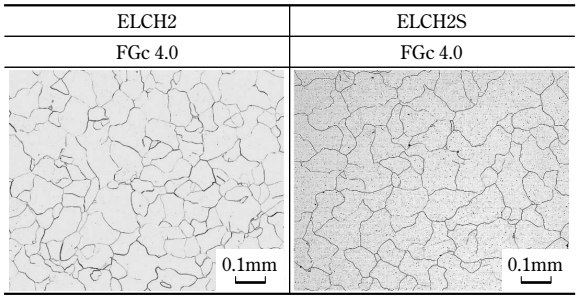

Fig. 7 Microstructure of developed steel after magnetic annealing

Fig. 7 compares the microstructures after the magnetic annealing of ELCH2 series steels. Each material shows a clean structure of single phase ferrite. It has been reported that, in the case of ELCH2S with improved machinability, MnS may provide pinning points against the growth of crystal grain during magnetic annealing[10]; however, the tested steels have almost the same size of ferrite grains, and no adverse effect was observed. Thus, in the case of the ELCH2 series, both the base composition and modified steel with improved machinability can have almost the same magnetic characteristics, as long as the heat treatment conditions are the same.

Table 2 shows typical magnetic characteristics of the ELCH2 series. Both of the base compositions, ELCH2 and ELCH2S with improved machinability, satisfy the superb magnetic characteristics achieved by JIS SUY-0. Also, they can exert electromagnetic force, comparable with that exerted by conventional low carbon steel, with a smaller applied magnetic field or smaller electric current, providing solutions for the improvement of component characteristics and power saving.

For example, assuming the magnetic flux density required to actuate an electromagnetic device to be 1.6T, SWRCH10A requires a magnetic field of 1,200A/m, while the ELCH2 series materials require only about 400A/m, reducing the energy for magnetomotive force required to produce magnetic flux by about 65%.

In addition, as shown in Fig. 6, ELCH2 series materials, as-rolled, satisfy magnetic characteristics comparable with those achieved by SWRCH10A, magnetic annealed. Thus, the magnetic annealing step can be omitted for the parts currently made of SWRCH10A, or of materials equivalent to it.

4.2 Mechanical properties

Table 3 shows the mechanical properties of the developed steels, as-rolled. The as-rolled materials have a tensile strength of about 300MPa and are comparable to spheroidized SWRCH10A. The tensile strength is increased by working, such as wire drawing, however, the softening that occurs during magnetic annealing makes the ultimate tensile strength about 230MPa regardless of the drawing reduction.

4.3 Cold forgeability

Fig. 8 compares the critical upsetting ratios at which the notched specimens start to exhibit cracks. The spheroidize annealed SWRCH10A exhibits a critical upsetting ratio as high as 70%, while the

Table 2 Magnetic properties of ELCH2 series (Magnetic annealed)

Steel	Magnetic field density (T)						Coercive force (A/m)
	B100	B200	B300	B500	B1000	B4000	
ELCH2S	0.90	1.24	1.47	1.54	1.64	1.80	55.7
ELCH2	0.92	1.30	1.50	1.60	1.65	1.81	45.2
SUY-1	≧0.60	≧1.10	≧1.20	≧1.30	≧1.45	≧1.60	≦80
SUY-0	≧0.90	≧1.15	≧1.25	≧1.35	≧1.45	≧1.60	≦60

Table 3 Mechanical properties of ELCH2 series

Steel	Tensile strength (MPa)	Young modulus (GPa)	Elongation (%)	Reduction area (%)
ELCH2	305	208	38.1	90.1
ELCH2S	306	209	36.7	92.8

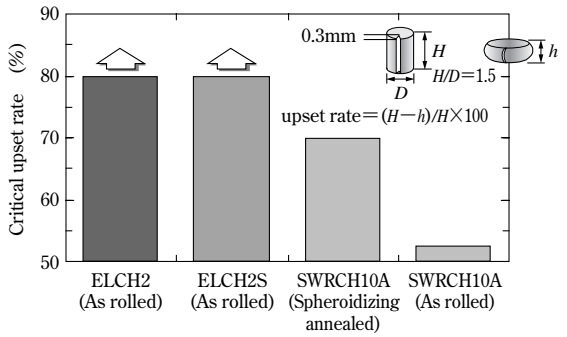

Fig. 8 Critical upset rate

newly developed steels exhibit no cracking at an upsetting ratio of 80%, even without softening annealing, demonstrating excellent deformability. Thus, ELCH2 series materials are effective in omitting process steps, such as heat treatment for softening before cold forging, and reducing the production cost of components.

4.4 Machinability

(1) Drillability

Fig. 9 shows the chips and average burr height observed for the through holes drilled under the conditions summarized in **Table 4**. In the case of ELCH2S with improved machinability, the chips are shorter and segmented with burr height significantly reduced when compared with the base composition, ELCH2. The ELCH2S steel has MnS precipitated and dispersed in its matrix. The precipitates behave effectively as stress concentration sites in the chips, improving the drillability.

(2) Turnability

Fig.10 shows the relationship between cutting speed and flank wear width for ELCH2S with improved machinability. The steel was cut under the conditions shown in **Table 5**. For a given cutting length (800m), the wear width tends to decrease with increased cutting speed. An increase in cutting speed from 80m/min to 700m/min decreased the tool wear to about 1/3 from 0.117mm to 0.038mm. The improvement effect is significant in the cutting speed range up to about 250m/min. High-speed cutting, with a cutting speed higher than 250m/min, has turned out to be effective in reducing tool wear when cutting pure iron based material as the newly-developed steel. The following are considered to be the reasons for reduced wear width during high-speed cutting[11]:

i) The temperature increase associated with cutting heat softens the work material, decreasing the cutting resistance.

ii) A lower cutting speed suppresses the generation of built-up edge on the cutting tool, which promote tool wear.

Fig.10 shows the tool wear width for the base composition, ELCH2, cut at a speed of 260m/min. For the same cutting condition, the wear width for the developed steel is about half that of the conventional steel, which verifies the effectiveness of the newly developed steel from the aspect of tool life.

4.5 Corrosion resistance

Salt spray tests were conducted on both the developed steel, ELCH2, and reference steel, SWRCH10A. **Fig.11** shows the changes in corrosion weight loss. The newly developed steel exhibits a corrosion weight loss about 40% smaller than that of the reference steel, SWRCH10A, demonstrating superior corrosion resistance compared with the reference material. The newly developed steel can be used without any problem for parts that have been made of conventional SWRCH10A or its equivalent.

ELCH2 series materials are designed to have ultra-low carbon content and a homogeneous structure with suppressed precipitation to achieve improved magnetic characteristics. This is considered to

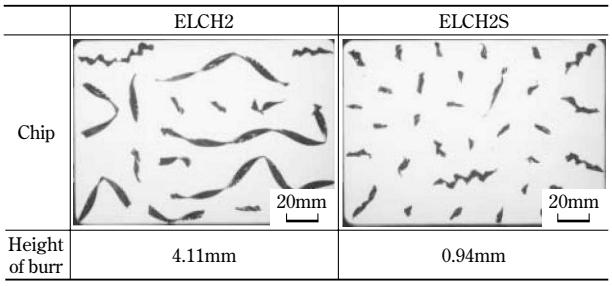

Fig. 9 Comparison of chip and height of burr

Table 4 Conditions for turning test

Tool	SKH straight drill
Cutting speed	30m/min
Feed rate	0.20mm/rev
Coolant	Dry

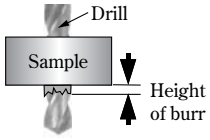

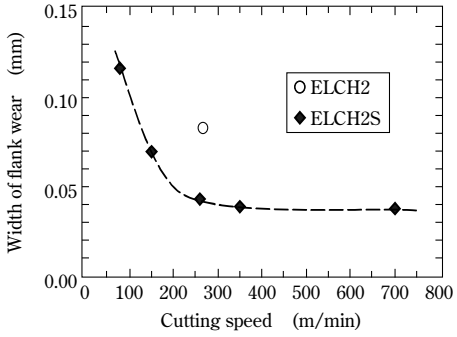

Fig.10 Relation between cutting speed and width of flank wear

Table 5 Conditions for turning test

Tool	Carbide AC200 (Sumitomo Electric)
Cutting speed (m/min)	80, 150, 260, 350, 700
Feed rate (mm/rev)	0.15
Depth of cut (mm)	0.2
Coolant	Water-solube

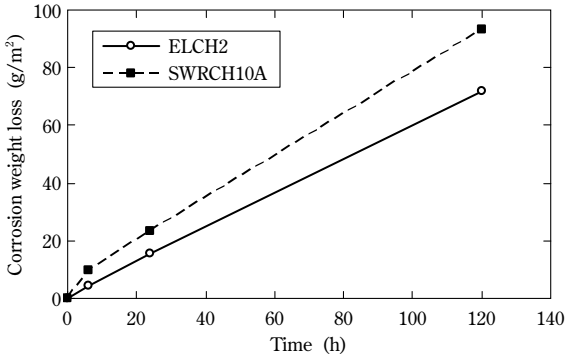

Fig.11 Corrosion weight loss

suppress the generation of local cell in the corrosive environment, leading to excellent corrosion resistance.

5. Application examples

ELCH2 series offer soft magnetic materials which are effective in improving and upgrading the performance of electromagnetically controlled systems and in reducing the cost of parts production.

The materials have been employed for iron cores for hydraulic control solenoids, as well as for large iron cores for electromagnetic clutches, greatly contributing to the reduction of power consumption and improvement of parts productivity[12), 13)].

Conclusions

Pure iron based soft magnetic materials, the ELCH2 series, having excellent magnetic characteristics and cold forgeability have been developed with the following features:

i) Reduced power for generating electromagnetic force, suppressing heat generation from components and reducing the load imposed on control circuits
ii) Cold forgeability, enabling the production of complex shaped parts, which greatly contributes to the performance improvement of electromagnetic devices and to the reduction of their production costs
iii) A steel with improved machinability featured by significantly reduced burrs and tool wear during cutting, which reduces the work load during cutting, compared with the base composition, which highly prioritizes magnetic characteristics

With the prevalence of hybrid electric vehicles and electric vehicles, electromagnetically controlled systems of new types are expected to be developed and applied. Kobe Steel strives to reduce the environmental burden and thus to contribute to society by providing pure iron based soft magnetic materials, the ELCH2 series, which make it possible to improve the performance of electromagnetic devices, save energy and reduce production costs.

References

1) A. HAMADA, "*Mitsubishi Denki Giho*" *(in Japanese)*, 1987, Vol.61, No.8, pp.651-656.
2) T. KAWANOBE, "*NAINENKIKAN*" *(in Japanese)*, 1987, Vol.26, No.333, pp.230-241.
3) ASM Committee on Magnetically Soft Materials, *Metals Handbook Vol.1*, American Society for metals, 1961, pp.785-797.
4) N. FUKAYA, Journal of Society of Automotive Engineers of Japan, 2004, Vol.58, No.4, p.48.
5) *JTEKT Engineering Journal*, 2007, No.1003.
6) M. CHIBA et al., *R&D Kobe Steel Engineering Reports*, 2002, Vol.52, No.3, pp.66-69.
7) T. KATO et al., *DENKI-SEIKO ELECTRIC FURNACE STEEL*, 1967, Vol.38, No.1, pp.2-8.
8) M. CHIBA et al., *R&D Kobe Steel Engineering Reports*, 2005, Vol.55, No.2, pp.18-21.
9) S. CHIKAKADO, *Physics of Ferromagnetism*, SHOKABO PUBLISHING, 1963, 310p.
10) Y. ODA et al., *NKK TECHNICAL REPORT*, 2002, No.178, pp.16-20
11) K. OZAKI et al., *Proceedings of JSPE Semestrial Meeting*, 2005, Vol.2005S, pp.593-594.
12) R. KUNII et al., *HONDA R&D Technical Review*, 2004, Vol.16, No.2, pp.9-16.
13) K. KUROKAWA et al., *Journal of Society of Automotive Engineers of Japan*, 2005, Vol.59, No.8, pp.105-108.

Influence of Ti Precipitate in Carburizing Steel Containing Boron

Dr. Nariaki OKAMOTO*1, Yosuke SHINDO*1, Mutsuhisa NAGAHAMA*2
*1 Wire Rod & Bar Products Development Department, Research & Development Laboratory, Iron & Steel Business
*2 Wire Rod & Bar Products Development Department, Research & Development Laboratory, Iron & Steel Business (currently with Wire Rod & Bar Products Marketing & Technical Service)

When cold forged gear steel is carburized, fine precipitates of TiC prevent austenite grain from coarsening. While preventing grain from coarsening, these precipitates increase the deformation resistance against cold forging due to precipitation hardening. This study evaluates the influence of TiC precipitates on the deformation resistance, as well as their characteristics that work to prevent grain coarsening during the carburization of a steel containing boron.

Introduction

Cold forging has caught the attention of automobile manufacturers in recent years because the process emits less CO_2 and enables lower-cost production than conventional forming methods such as cutting and hot forging. In particular, there is an increasing need for the steel used to produce cold-forged gears. Cold forging of steel, however, is associated with a deformation resistance much higher than that associated with hot-forging. Because of this, it is difficult to form complex shaped parts, such as gears, by cold forging. Thus steel for cold forged gears is required to have a deformation resistance much lower than that of conventional gear steel.

On the other hand, gears are carburized for strengthening. If the gears are cold forged before carburizing, the strain energy induced by the cold forging can cause crystal grain to coarsen during carburization, which may adversely affect the accuracy of the parts. To prevent this, steel for cold forged gears contains alloying elements, such as Al, Nb and Ti, which precipitate carbonitrides having a "pinning effect". This pinning effect has long been exploited to prevent crystal grain from coarsening. The addition of these elements, however, increases the deformation resistance. Thus, it is important to exert the pinning effect effectively by carefully controlling the precipitation state of the carbonitrides while minimizing the amount of alloying elements added.

With this background, a study was conducted on the effect of the precipitation state of carbonitrides, as reported in this paper. This study aims to develop a steel that has a small deformation resistance, is effective in preventing crystal grain from coarsening and is suitable for the cold forging of gears.

1. Considerations on steel for cold forged gears

Steel for cold forged gears exploits the pinning effect exerted by carbonitrides of elements such as Al, Nb and Ti to prevent the coarsening of crystal grains. To effectively exert this pinning effect, it is necessary to secure a large number density of carbonitride precipitates during carburization by suppressing Ostwald ripening, in which large precipitates grow larger by absorbing adjacent smaller precipitates. Since Ostwald ripening is a phenomenon accompanying atomic diffusion, alloying elements with low diffusion coefficients are preferable for effectively exerting the pinning effect[1]. The diffusion coefficients of Al, Nb and Ti (**Table 1**) indicate that Ti is the most effective element in exerting the pinning effect.

As shown in **Fig. 1**[2], the pinning effect can be explained by a force acting to grow crystal grains (hereinafter referred to as "growth force") and a force exerted by precipitates and acting to suppress grain growth (hereinafter referred to as "suppressive force"). The growth force is given by Formula (1) according to the Gibbs-Thomson law:

Table 1 Diffusion coefficient forming carbonitride

Element	Diffusion coefficient (m^2/sec)	Precipitation
Al	3.0×10^{-3}	AlN
Nb	5.6×10^{-4}	NbCN
Ti	1.5×10^{-5}	TiC

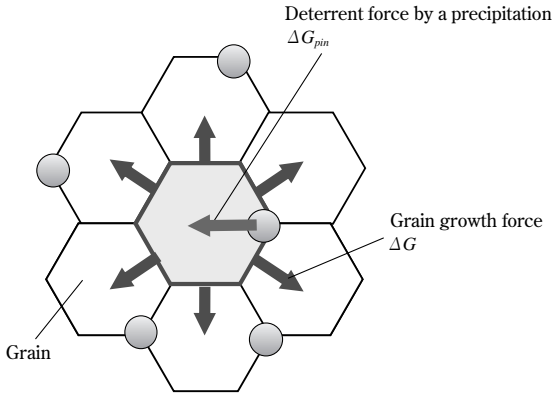

Fig. 1 Schema of grain growth and pinning effect

$$\Delta G \approx \frac{4\sigma V}{D} \quad \cdots\cdots(1)$$

wherein ΔG : growth force
σ : grain boundary energy
V : molar volume
D : crystal grain diameter

On the other hand, the suppressive force is given by Formula (2) according to the Zener-Smith model:

$$\Delta G_{pin} \approx \frac{\pi d \sigma}{2} nV \quad \cdots\cdots(2)$$

wherein ΔG_{pin} : suppressive force
d : diameter of precipitates
n : number density of precipitates per unit area

In the case where grain boundary growth is suppressed, the growth force and suppressive force become equal ($\Delta G = \Delta G_{pin}$:), and thus the relationship between the grain diameter and precipitates diameter is given by Formula (3).

$$D \approx \frac{8}{\pi n d} \quad \cdots\cdots(3)$$

Formula (3) indicates that grain coarsening is more effectively suppressed by precipitates grown in a high number density and having large diameters.

On the other hand, the precipitates generated may trigger the precipitation strengthening mechanism, increasing the deformation resistance during cold forging. The precipitation strengthening is given by Formula (4) according to the Ashby-Orowan model[3]:

$$\Delta\sigma = 2.95\sqrt{\pi n}\ln\left(\frac{d}{2.5\times10^{-4}}\right) \quad \cdots\cdots(4)$$

where $\Delta\sigma$ is the deformation resistance increment.

Formula (4) indicates that the deformation resistance during cold forging increases with higher precipitate density and larger precipitate diameter. In other words, properly controlling the precipitate density and grain size can suppress grain coarsening during carburizing and prevents the deformation resistance from increasing during cold forging.

2. Experimental method

Two types of steel, as shown in **Table 2**, were used for the present experiment, i.e., carburizing steel containing Ti and B, and SCM420H, which is generally used for gears. In order to clarify the effect of precipitation states on the deformation resistance and on the characteristic of preventing grain from coarsening, the carburizing steel containing Ti and B was subjected to four kinds of heat treatment (i.e., conditions ① to ④) to prepare steel samples having different precipitation states of TiC, as shown in **Fig. 2** and **Fig. 3**.

To study the deformation resistance, all the steel samples (the carburizing steel containing Ti and B, heat-treated under conditions ① to ④, plus SCM420H) were formed into solid cylinders, each having a dimension of $\phi 20 \times 30$mm. The cylindrical specimens were compressed with their ends confined with a compression rate of 75%. After this compression test, the specimens were carburized at 950℃ to investigate the characteristic of preventing grain from coarsening. Observations to determine grain size number were conducted in the area including an equivalent strain of 2.0, as shown in **Fig. 4** (the area surrounded by a broken line in the figure).

Table 2 Chemical composition of specimens

Steel	Chemical composition (mass%)						
	C	Si	Mn	Cr	Mo	Ti	B
Carburizingsteel containg B	0.17	0.06	0.44	1.38	—	0.04	add
SCM420H	0.20	0.18	0.83	1.12	0.17	—	—

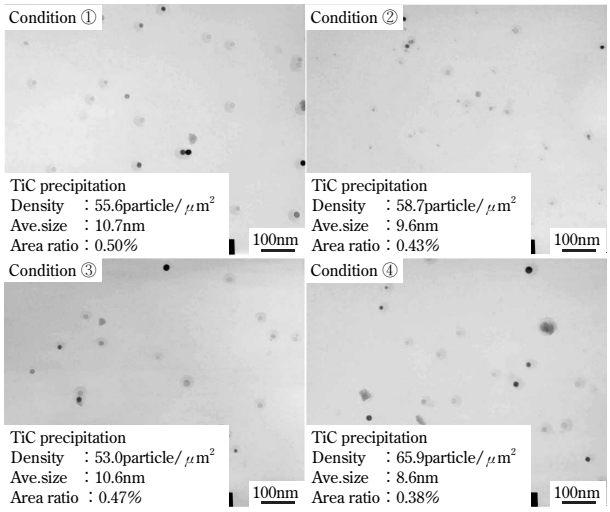

Fig. 2 Precipitation condition of TiC

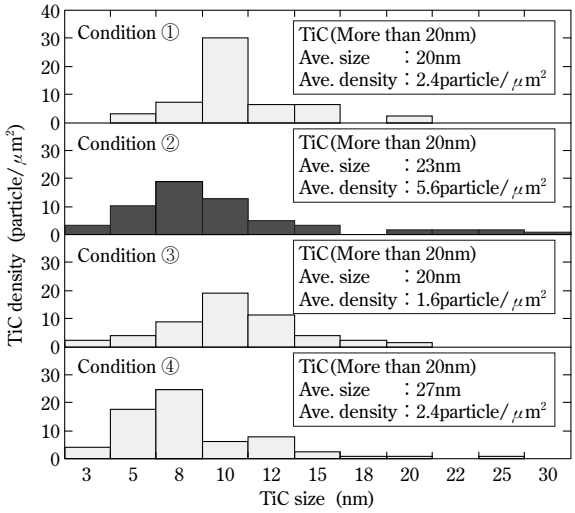

Fig. 3 Condition of TiC distribution

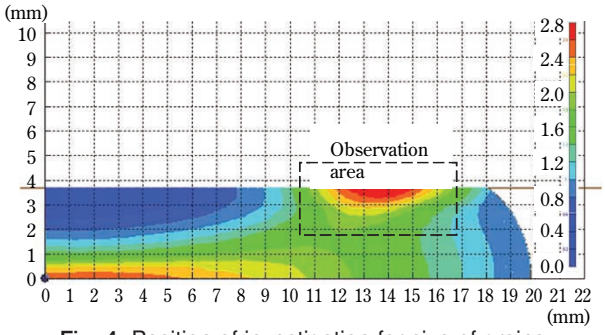

Fig. 4 Position of investigation for size of grains

3. Experimental results

Fig. 5 shows the deformation resistance of materials softened under conditions ① to ④. Almost no difference was found in the deformation resistance for carburizing steels containing Ti and B, treated under conditions ① to ④. (Their hardness is about 16% lower than that of SCM420H.) The results indicate that the difference in the precipitation state of TiC, investigated in this experiment, does not significantly affect the deformation resistance.

Fig. 6 depicts micrographs showing the grain size numbers of specimens carburized after a compression test. These micrographs indicate that the grain size numbers of the top-most surface layers all fall around No.12 regardless of which of the ① to ④ conditions applies; they show no difference. It should be noted however that, at a depth deeper than 400 μm from the surface layer, conditions ①, ③ and ④ (unlike condition ②) yielded coarser grains with grain size numbers no greater than No. 3, as observed in the area surrounded by circles in the figures. This is despite the fact that conditions ① to ④ all yield an average grain size number of around No.8.

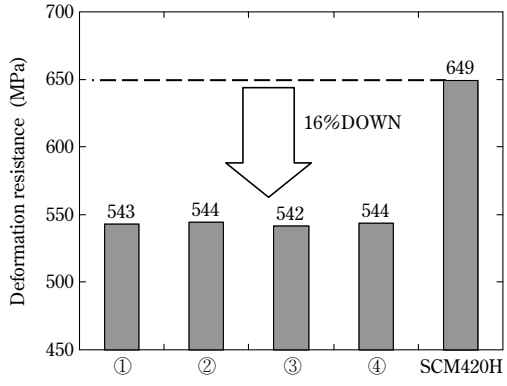

Fig. 5 Deformation resistance of each specimen

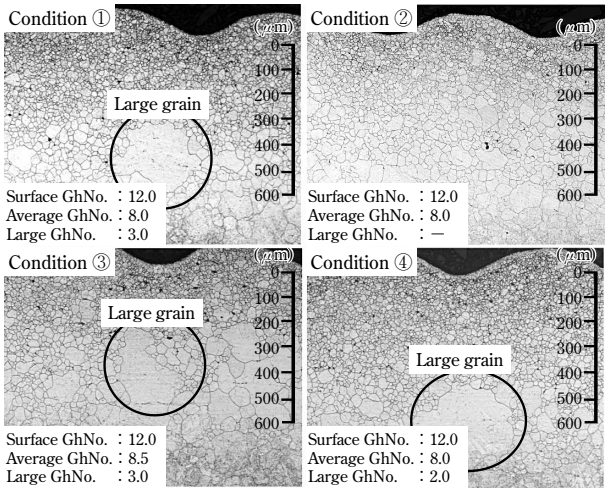

Fig. 6 Grain size of carburized specimen after compressing test

4. Discussions

4.1 Effect of precipitation state on deformation resistance

Formula (4) indicates that the deformation resistance during cold forging is affected by the grain size and density of precipitates. The materials, treated under conditions ① to ④, have precipitates (TiC) with different diameters and densities, as shown in Fig. 2 and Fig. 3; however, they resulted in almost no significant difference, with their deformation resistances falling around 542 to 544MPa, as shown in Fig. 5. The effect of the precipitation state on deformation resistance is calculated by applying the values of the density and average size, shown in Fig. 2, to Formula (4). As shown in **Table 3**, the increments in deformation resistance for the precipitation state of conditions ① to ④ are calculated to be 143 to 150MPa, showing hardly any difference, just as in the case of the measured values. Therefore, the precipitates from conditions ① to ④ are regarded as having almost no effect on the deformation resistance.

4.2 TiC effect of preventing crystal grain coarsening

As shown in Fig. 6, all the conditions, ① to ④, resulted in surfaces with a grain size number of No.12 (grain size: about 6 μm), with hardly any differences. These fine crystal grains are attributable to the pinning effect of TiC. According to Formula (3), grain size can be evaluated by precipitate diameter and density. Assuming that TiC, observed before carburization, remains unchanged after carburizing, Formula (3) yields grain sizes of 4.3 to 4.5 μm for conditions ① to ④, using the values shown in Fig. 2. These values agree with the observed values, showing hardly any differences. These results indicate that the majority of TiC precipitates effectively exert a pinning effect.

On the other hand, for conditions ①, ③ and ④, coarse crystal grains with a grain number of 8 (grain size: about 22 μm), were observed at a depth deeper than 400 μm (Fig. 6). These coarse grains are attributable to the less effective pinning effect exerted by smaller TiC precipitates, which are energetically less stable than larger ones, and dissolve into the solid matrix during carburization, decreasing the number density of the precipitates.

The solid solubility of these precipitates can generally be explained by solubility curves such as the one shown in **Fig. 7** [4]. In Fig. 7, dissolved Ti becomes more stable as the concentrations of Ti and C approach the lower left corner, and TiC becomes more stable as the concentrations approach the upper right corner, with respect to the border curve for the carburizing temperature of 950℃. Thus it is considered that the carburized steel containing B has a lower C concentration in its interior than in its surface layer, making TiC less stable. It is also considered that, in the interior of the carburizing steel containing B, smaller TiC precipitates, which are energetically less stable, dissolve into the solid matrix, leaving relatively larger TiC precipitates in the matrix during carburization. Thus, it is possible to quantitatively evaluate the crystal grain coarsening from the condition of the relatively larger TiC precipitates observed before carburization. Assuming that the TiC precipitates larger than 20nm, as shown in Fig. 3, remain effective in exerting a pinning effect during carburization without being dissolved into the matrix to form a solid solution, Formula (3), provided with their average diameter and number density, yields grain sizes for conditions ① to ④, as shown in **Fig. 8**. Fig. 8 indicates that condition ②, which caused no crystal grain coarsening yielded a measured grain size that agrees well with the calculated value. On the other hand, conditions ①, ③ and ④, which caused crystal grain coarsening, resulted in calculated values greater than 40 μm (grain number, No.6). These results consistently elucidate the fact that, at a depth deeper than 400 μm from the surface, TiC precipitates smaller than 20nm dissolve into the matrix to form a solid solution during carburization, losing their pinning effect and leaving only TiC greater than 20nm exerting the pinning effect.

From the above, the behaviors of TiC and crystal grains, during carburization in the B-containing carburizing steel, are classified into two cases as shown in **Fig. 9**, i.e., Case I, where a small number of TiC precipitates greater than 20nm exist; and Case II, where a large number of TiC precipitates greater than 20nm exist. In Case I, the surface layer has a C concentration high enough to maintain TiC

Table 3 Deformation resistance and calculation of the influence by precipitation hardening

Heat history	Measurement (MPa)	Calculation (MPa)
	Deformation resistance	Increase of deformation by precipitation
Condition ①	543	146
Condition ②	544	146
Condition ③	542	143
Condition ④	544	150

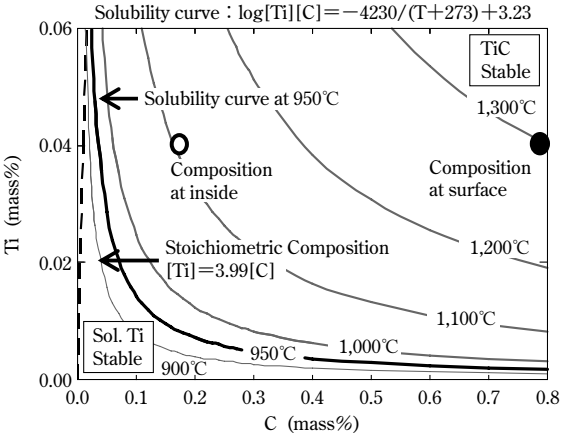

Fig. 7 Solubility Curve of TiC

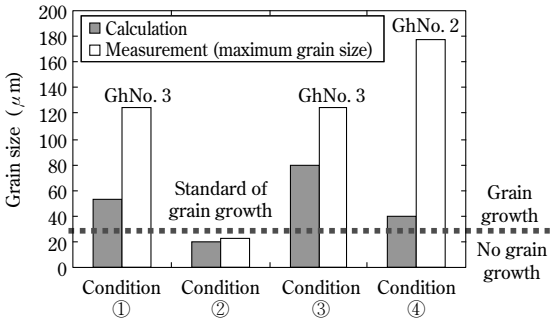

Fig. 8 Comparison of measurement value and calculation in grain size around 400 μm from surface

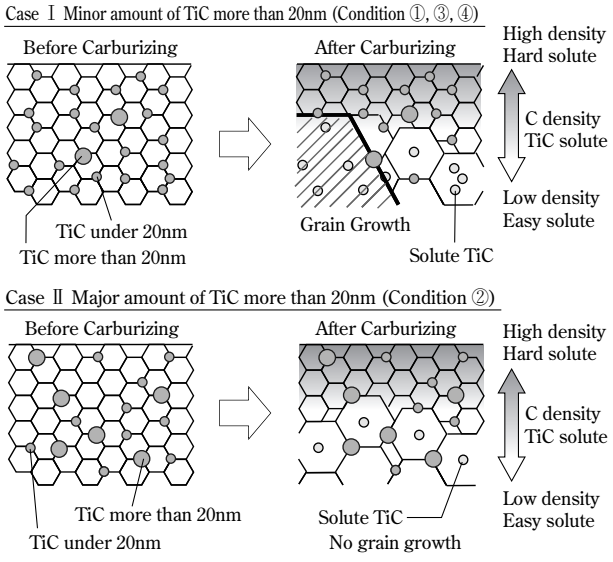

Fig. 9 Schema of relation of TiC and grain size by carburization

precipitates stably regardless of their sizes, which prevents the crystal grain from coarsening. Meanwhile, in the interior, the C concentration becomes low, causing TiC precipitates smaller than 20nm to dissolve into the matrix to form a solid solution, which decreases the number of particles contributing to the pinning and causes crystal grain coarsening. On the other hand, in Case Ⅱ, the surface layer has a C concentration high enough to maintain TiC precipitates stably regardless of their sizes, which prevents crystal grain coarsening; this is the same as in Case I. However, in the interior, C concentration becomes so low that TiC precipitates smaller than 20nm dissolve into the matrix to form a solid solution. Meanwhile, TiC precipitates larger than 20nm remain undissolved, ensuring the number of particles contributing to the pinning, which serves to prevent crystal grain coarsening.

Conclusions

A study was conducted with the aim of developing a steel for cold forged gears that has decreased deformation resistance and the effect of preventing crystal grain coarsening. The following results were obtained:

(1) Conditions ① to ④, applied for varying precipitation states without changing the composition, resulted in no significant difference in the deformation resistance.
(2) Conditions ① to ④ yielded different grain size distributions after carburization following compression. Crystal grain coarsening was prevented effectively in the surface layer under all of the conditions; however, only condition ② was effective in preventing the grain from coarsening at a depth of around 400 μm from the surface layer.
(3) For conditions ①, ③ and ④, grain coarsening occurred at a depth of about 400 μm from the surface. This is attributable to the lower density of TiC precipitates larger than 20nm, compared with the case of condition ②.

References

1) E. Fujita, *Kinzoku-Butsuri*, AGUNE GIJUTSU CENTER (2004), p.659.
2) T. Nishizawa et al., *Thermodynamics of microstructure*, Japan Institute of Metals (2005), p.140.
3) W. C. Leslie, *Ferrous material*, Maruzen (1985), p.213.
4) H. Ohtani et al., *Proceedings of Japan-Canada Seminar on Secondary Steelmaking* (1985), p.1.

Low Alloy Steel for Fracture Splitting Connecting Rod

Akihiro MATSUGASAKO*1
*1 Wire Rod & Bar Products Development Department, Research & Development Laboratory, Iron & Steel Business

To reduce vanadium content in the steel for fracture splitting connecting rods, the effect of titanium addition on the splitting property was investigated. The results indicate that Ti addition effectively reduces the impact value of the steel. This is considered to be attributable to the decrease in the volume fraction of ferrite and in the precipitation strengthening of the ferrite. Furthermore, Ti was also found to have no adverse effect on machinability. Based on these results, a new steel was developed for fracture splitting connecting rods.

Introduction

Among the characteristics required for automobiles, "low environmental burden" and "safety" are two key features gaining increasing recognition. The environment, in particular, is receiving much public attention, and automakers are actively moving forward to develop low-emission and fuel-efficient cars[1), 2)].

Automobiles must be manufactured at a low cost while achieving the above objectives. To reduce the cost, low alloy steel is being pursued, as is a simplified manufacturing process. With this background, a method of production according to the fracture splitting process was developed to reduce the cost of manufacturing connecting rods, which are automobile engine parts[3)]. The conventional process for making a connecting rod includes forging and rough-machining the rod portion and cap portion separately, providing these portions with dowels and coupling them before finishing. On the other hand, according to the fracture splitting process, the rod and cap portions are forged and rough-machined as a unified body and notches are machined on the body along a plane, which later becomes the coupling surface. In the subsequent step, the forged body is fractured along these notches to split the rod and cap portions, and finish machining is performed on these split portions (**Fig. 1**). This production method improves the material yield of the forged body and eliminates the need for processing cap portions, dowel pins and the holes. Since the fracture splitting method was implemented in the 1990s, it has prevailed in Europe and US, and an increasing number of Japanese manufacturers have introduced this method[3) - 6)].

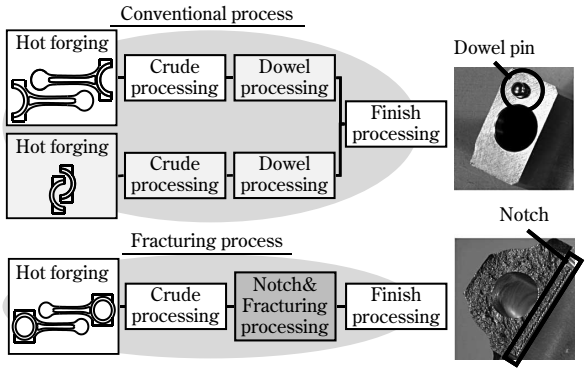

Fig. 1 Manufacturing process of connecting rods

Steel for fracture splitting connecting rod must be split with minimum deformation (fracture splittability), in addition to possessing the characteristics required for conventional steel used in connecting rods. In Europe, a steel, C70S6, according to the DIN standards, is widely used. This steel has a microstructure that is almost entirely occupied by pearlite to ensure fracture splittability. Kobe Steel also developed a steel for fracture splitting connecting rod with high-strength. The steel ensures fracture splittability by the increased addition of P and V, as well as spheroidized MnS[7)].

To avoid the risk of relying on scarce resources, Kobe Steel pursued a technique for improving the fracture splittability with less addition of V and has newly developed a steel for fracture splitting connecting rod based on newly acquired knowledge. This paper outlines that development.

1. Study on alternative means for low alloying

Although C70S6 steel contains no alloying element with a high availability risk, it suffers from a lack of machinability because it contains a large amount of hard cementite. On the other hand, non-heat-treatment steel, consisting of ferrite and pearlite, has fewer problems with machinability; however, the toughness of its proeutectoid ferrite (hereinafter simply referred to as "ferrite") must be reduced to improve its fracture splittability. This is clear from the fact that reduced impact strength improves fracture splittability[7)]. A method is being developed to reduce its impact resistance by adding V and/or P to increase the strength and thus to embrittle the ferrite.

Because Vanadium is produced by a limited number of countries and is a scarce resource with availability risk[8], an alternative element has been sought. Thus, Kobe Steel has focused on Titanium, which is considered to have a large output with less risk of unavailability, and which forms carbide as in the case of V. The company conducted a study on the effect of Ti addition on impact resistance and machinability to determine the feasibility of substituting Ti for V.

2. Experimental procedure

2.1 Materials tested

Table 1 shows the chemical compositions of the materials tested. Four types of steels were tested, i.e., two types of steels (Steel A and Steel B), with or without Ti, to study the effect of Ti, a steel (Steel C) equivalent to C70S6 as a reference for evaluating fracture splittability, and a steel (Steel D), equivalent to the conventional steel used for connecting rod, as a reference for evaluating machinability. The steels were melted in a laboratory scale vacuum melting furnace, and hot forged at 1,200℃ into a predetermined shape before the testing.

2.2 Impact test

To study the effect of Ti on impact strength, Steel A and Steel B were subjected to a Charpy impact test. A hot forged cylinder having a diameter of ϕ30mm was hot pressed in a diametrical direction to produce a plate having a thickness of 15mm, from which a U-notched specimen was prepared.

2.3 Machinability test

Drill life was evaluated to study the machinability. A hot forged cylinder having a diameter of ϕ80mm was provided as a work material whose cross-section was subjected to drilling for drill life evaluation. The tool used was a high-speed steel drill with a diameter of ϕ10mm. The test was conducted under dry conditions with a feed rate of 0.21mm per revolution. The total cutting length until the drill broke was taken as the drill life.

Table 1 Chemical compositions of samples (mass%)

Sample	C	Si	Mn	P	S	Cr	V	Ti
Steel A	0.38	0.25	1.07	0.051	0.050	0.18	0.170	0.051
Steel B	0.38	0.24	1.08	0.049	0.050	0.18	0.160	—
Steel C	0.70	0.23	0.54	0.011	0.058	0.11	—	—
Steel D	0.41	0.26	1.06	0.019	0.060	0.23	0.099	—

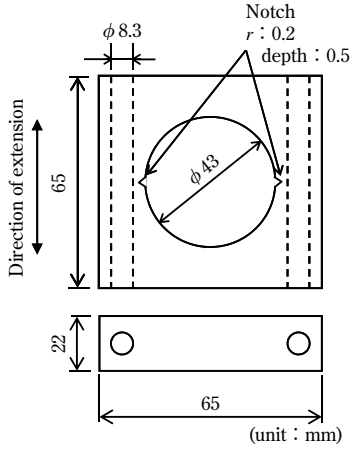

Fig. 2 Fracture splitting test piece

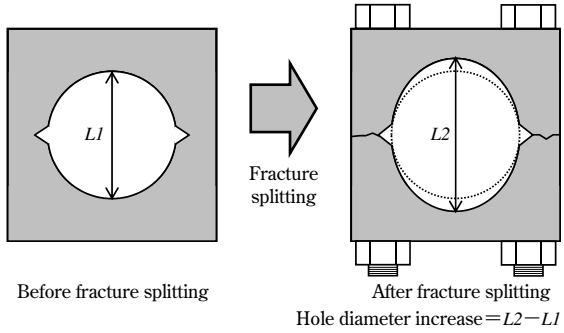

Fig. 3 Measuring method of hole diameter increase

2.4 Fracture splitting test

The fracture splittability was evaluated by a fracture splitting test. A hot forged round bar with a diameter of ϕ65mm was hot pressed in a diametrical direction to produce a plate having a thickness of 25mm. The plate was machined into a fracture splitting specimen as shown in **Fig. 2**. The notches were provided in a direction vertical to the forging direction such that the fracture split would occur at positions that simulate actual connecting rods. The fracture splittability was evaluated by the change in the hole diameters before and after fracture splitting. In other words, as shown in **Fig. 3**, the hole diameter was measured before the fracture splitting and was measured again after the split parts were fastened by bolts. The difference in the hole diameter was taken as an index of fracture splittability.

3. Experimental results and discussions

3.1 Impact test

Fig. 4 shows the results of the Charpy impact tests. It has turned out that the addition of Ti decreases the impact resistance significantly. The fracture surfaces and microstructures of impact

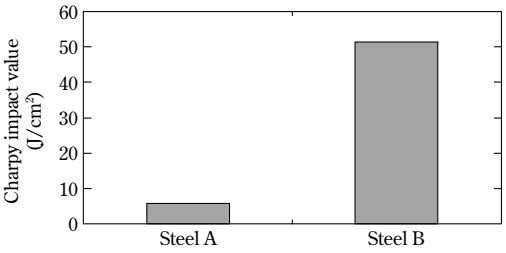

Fig. 4 Result of Charpy impact tests

specimens Steel A and Steel B were observed in detail to elucidate the phenomena that occurred during the impact test.

3.1.1 Fracture surface observation

Fig. 5 shows the SEM micrographs of fracture surfaces. Steel A exhibits cleavage throughout almost the entire surface without any of the dimpling that is a feature of ductile fracture. The partially observed grain boundaries indicate that the fracture, to put it more exactly, is caused by quasi-cleavage. Steel B, on the other hand, exhibits dimples throughout almost the entire surface of the specimen at the notch bottom where the initial crack was introduced. It should be noted that the cleavage fracture surface is located more than about 300 μm inside the fracture surface.

This indicates that the decrease in impact resistance brought about by the addition of Ti is attributable to the suppression of ductile fracture accompanying dimples. These dimples are generated by the plastic deformation of matrix surrounding inclusions, and in a ferrite-pearlite structure, the plastic deformation is mainly governed by ferrite[9]. Thus it is highly possible that the addition of Ti serves to embrittle the ferrite.

3.1.2 Microstructure

Microstructures were observed to study the change in the ferrite. **Fig. 6** shows the results of the study. The addition of Ti has turned out to decrease the ferrite fraction from 29% to 20%, while increasing the hardness from 272.0HV to 294.7HV. The decreased ferrite fraction raises the ductile-brittle transition temperature[9], lowers the upper shelf energy[10] and lowers the impact resistance value. These effects are considered to be the cause of the lowered impact value.

Now, a detailed study was carried out to elucidate the cause of the ferrite fraction's being decreased by the addition of Ti. Continuous cooling transformation (CCT) diagrams were prepared to study the transformation behaviors. The heating temperature was set to 1,200℃ to simulate the

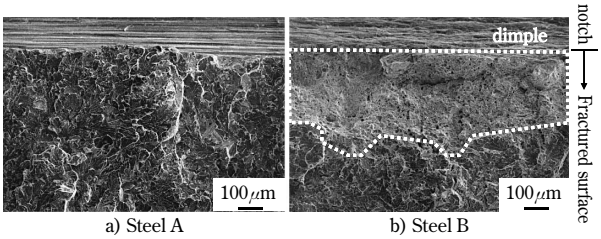

Fig. 5 SEM images of fractured surface

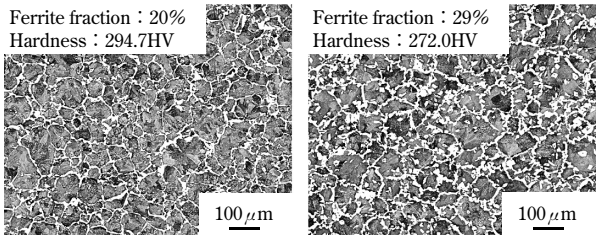

Fig. 6 Microstructures and hardness of Steel A and B

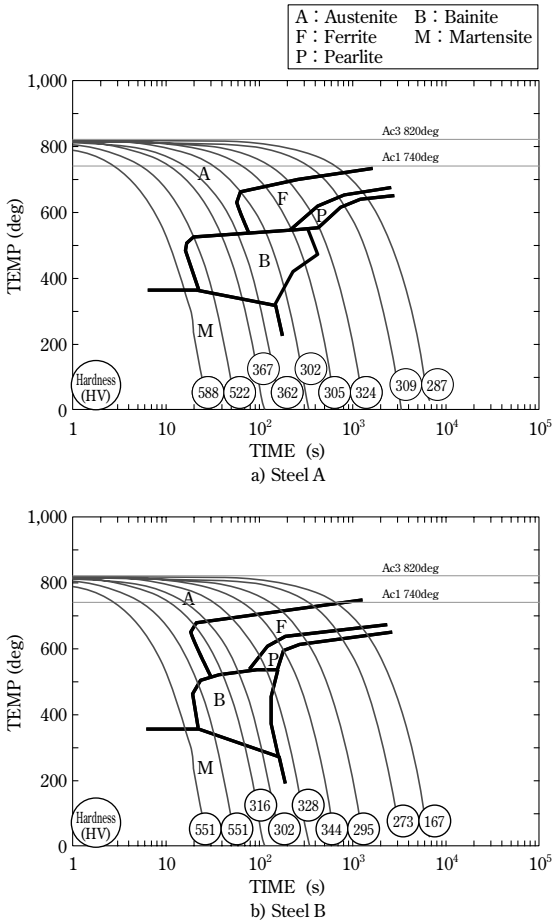

Fig. 7 Continuous cooling transformation diagram

behavior during hot forging. The results are shown in **Fig. 7**. The results indicate that the addition of Ti delays the initiation of diffusion transformation (ferrite transformation), shifting the curves toward longer times and lower temperatures.

The following discusses the reason why the Ti addition delays the initiation of ferrite transformation.

Firstly, Ti is an element having a strong affinity with C, forming carbide. Another carbide forming element, V, has been known to decrease the diffusion rate of C[11]. Thus, Ti is assumed to decrease the diffusion rate of C, as in the case of V. The decreased diffusion rate is considered to suppress diffusion transformations such as ferrite transformation and pearlite transformation.

Next, a detailed study was conducted on the increase of hardness. The hardness increase is attributable both to the precipitation hardening effect of TiC and the decrease in the ferrite fraction. To verify the effect of the ferrite fraction on the hardness change, a mixing rule was adapted for hardness. The mixing rule for hardness is given by the following relationship[12]:

$$HV = f_\alpha^{1/3} HV_\alpha + (1 - f_\alpha^{1/3}) HV_p \quad \cdots\cdots(1)$$

in which HV represents overall hardness, f_α represents the ferrite fraction, HV_α represents ferrite hardness and HV_p represents pearlite hardness.

The effect of the ferrite fraction was calculated for the ferrite fractions shown in Fig. 6, assuming HV_α = 235 and HV_p = 295. According to the calculation, a 9 percent decrease in ferrite fraction increases the hardness by about 5HV. Thus, in the total hardness increment of about 23HV, shown in Fig. 6, approximately 18HV is attributable to precipitation hardening by TiC. This precipitation hardening is considered to have caused the ferrite to harden and embrittle.

3.1.3 Embrittlement mechanisms by Ti addition

From the above, the following is proposed to be the mechanism of Ti addition decreasing the impact resistance.

The addition of Ti serves i) to decrease the ferrite fraction, raise the ductile-brittle transition temperature and lower the upper shelf energy; and ii) to cause precipitation hardening, to increase the strength of ferrite and to decrease the plastic deformability.

These effects cause cleavage fracture to occur while suppressing the ductile fracture that accompanies dimples, leading to reduced impact resistance. Particularly in this study, the ferrite fraction had a significant effect, which can be exploited in improving the fracture splittability by reducing the impact resistance value.

3.2 Machinability test

Fig. 8 shows the results of the machinability test. The machinability of Steel C (C70S6 equivalent) was dramatically degraded, while Steel A, Steel B and Steel D exhibit almost equal tool lives, indicating no adverse effect of Ti addition on machinability. Steel D is the steel equivalent of conventional connecting rod.

3.3 Fracture splitting test

Based on the knowledge obtained in Sections 3.1 and 3.2, compositions were determined for low alloy steel for fracture splitting connecting rod. The low alloy steel has a strength (proof strength of about 600MPa) equivalent to that of the conventional connecting rod steel (Steel D). **Table 2** shows a sample composition of the newly developed steel. This steel contains Ti in about the same amount as in Steel A, in which the effect of Ti addition has been sufficiently confirmed. It also contains V in about the same amount as in Steel D to achieve the same level of strength. The newly developed steel contains V in an amount reduced by about 60% compared with the conventional steel made by Kobe Steel for fracture splitting connecting rod.

Fracture splitting tests were conducted on the five steels; i.e., Steels A-D and the newly developed steel. **Fig. 9** shows the test results. The newly

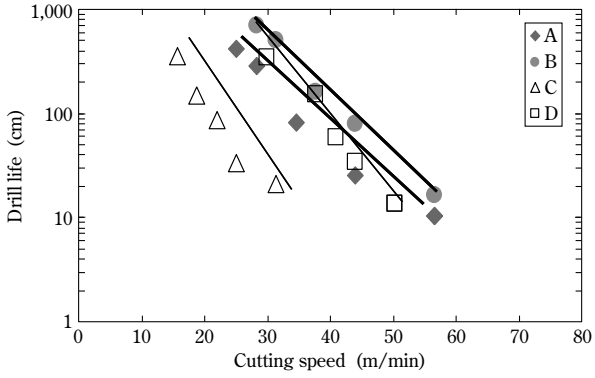

Fig. 8 Results of drill life test

Table 2 Chemical compositions of developed steel

(mass%)

Sample	C	Si	Mn	P	S	Cr	V	Ti
Developed steel	0.37	0.25	1.12	0.047	0.062	0.29	0.106	0.043

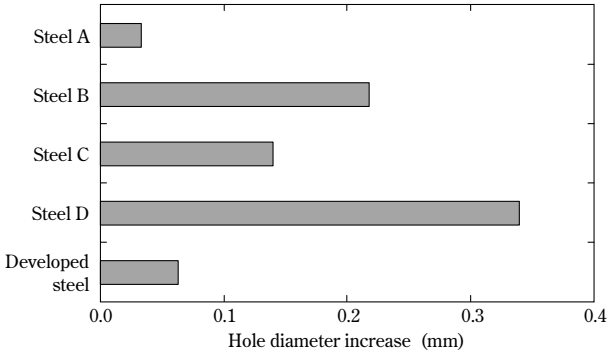

Fig. 9 Hole diameter increases

developed steel and Steel A, both containing Ti, exhibit a fracture splittability that significantly exceeds that of Steel B and Steel D without Ti addition and is better than that of Steel C, the C70S6 equivalent. The results confirm that the addition of Ti enables the improvement of fracture splittability with a decreased addition of V.

Conclusions

With the aim of developing a low alloy steel for fracture splitting connecting rod, a new technique was devised to improve the fracture splittability, in which Ti is substituted for V. It has turned out that the addition of Ti decreases the ferrite fraction, induces the precipitation hardening of the ferrite, facilitates cleavage fracture and reduces the impact resistance value. Furthermore, the Ti addition has been found to ensure favorable fracture splittability without sacrificing machinability. Based on the new knowledge, a new steel, containing much less V, was developed for fracture splitting connecting rods.

References

1) Edition by Society of Automotive Engineers of Japan, Inc., *Material Technology for Automobiles*, 5 (1996), p.2, Asakura Publishing Co., Ltd.
2) Edition by Society of Automotive Engineers of Japan, Inc., *Automobile Technology Handbook*, 1 (2008), p.1, Society of Automotive Engineers of Japan.
3) Z. Gu et al., *The International Journal of Advanced Manufacturing Technology*, Vol.25, No.9-10 (2005), pp.883-887.
4) T. Kubota et al., *YAMAHA MOTOR TECHNICAL REVIEW*, No.39 (2005), pp.80-87.
5) S. Koganemaru et al., *Proc. of Annual Conference of JSAE*, No. 20-06 (2006), p.7.
6) N. Kyotoku, *Society of Automotive Engineers of Japan, Symposium, Newly Developed Engine*, No.19-07 (2008), p.19.
7) G. Anan, et al., *R&D KOBE STEEL ENGINEERING REPORTS*, Vol.56, No.3 (2006), pp.44-47.
8) Japan Oil, Gas and Metals National Corporation, *Mineral Resources Material Flow* 2009, (2009), pp.147-152.
9) T. Araki, *Materials Engineering for Steel* (1970), p.102, Maruzen.
10) S. Okamoto : *Steel Materials* (1960), p.167, Corona Publishing Co., Ltd.
11) S. N. Tewari et al., *Journal of Materials Science*, Vol.17, No.6 (1982), pp.1639-1648.
12) T. Gladman et al., *Journal of The Iron and Steel Institute*, Vol.210 (1972), pp.916-930.

Production Technology of Wire Rod for High Tensile Strength Steel Cord

Kazuhiko KIRIHARA*1
*1 Wire Rod Production Department, Kakogawa Works, Iron & Steel Business

The wire rod for steel cord is designed for high tensile strength. The steel cord is typically used to reduce tire weight. For several years, such steel cord has also been used as saw wire to cut silicon ingots. The saw wire is more highly tensile and has a smaller diameter. Therefore, an appropriate wire rod is required for manufacturing such saw wire. This report describes the technology to control non-metallic inclusions and the wire rod with superior drawingability needed for manufacturing the high strength wire used for steel cord and saw wire.

Introduction

Steel cord, with its excellent strength and resilience, is used in various industrial applications such as reinforcing materials for tires and conveyor belts.

The steel cord used for automobile tire reinforcement is a strand of fine wires of ultrafine drawn steel, called filaments. The downside of steel cord is its specific strength, lower than that of other reinforcing materials consisting of chemical fibers such as rayon, nylon and polyester; this is a downside that increases the weight of tires. On the other hand, steel cord has the advantages of a high modulus of rigidity, as well as excellent thermal conductivity, which prolongs the life of tires significantly and provides automobiles with superior traveling performance and driving stability.

With the proliferation of automobiles in newly developing countries, the use of steel cord is expected to increase dramatically. To meet the market needs for lighter tires, improved fuel economy and a simplified manufacturing process, there is a demand for steel cord that can be produced in larger quantities and with even higher strength.

Meanwhile, the market for solar energy generation has been rapidly growing in the last several years, since it emits no CO_2 during power generation and is in accord with the global effort to reduce the environmental burden. The silicon wafers used for solar panels are sliced from silicon ingots using saw wires (**Fig. 1**). To improve the yield of the material to be sliced, a saw wire must have a fine diameter. A sliced wafer, on the other hand, is required to have a cut surface with strain suppressed in order to achieve high efficiency in power generation. As a means for suppressing the strain on the cut surface, it is effective to increase the strength of the saw wires. Here again, high strength wires are demanded, as in the case of steel cord.

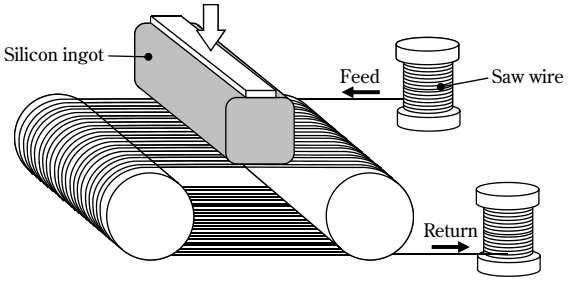

Fig. 1 Schematic of cutting of silicon ingot

This paper describes some approaches taken to reduce the diameter of steel cord and to simplify the production process. Also described is the projected future of the wire rods used for steel cord.

1. Qualities required of steel cord

Table 1 shows typical chemical compositions of wire rods produced by Kobe Steel for steel cords. **Fig. 2** shows the trend toward increasing the strength of steel cord [1]. The tensile strength of a filament with a diameter of 0.20mm was 2,800MPa in the 1970s, 3,300MPa in the 1980s, and reached a high-strength of 3,600MPa in the early 1990s and 4,000MPa in the late 1990s [2, 3]. Steel cord strengthened by wire drawing

Table 1 Chemical compositions of wire rod for steel cord

(mass%)

Steel grade	C	Si	Mn	P	S	Cr
KSC72	0.70-0.75	0.15-0.30	0.40-0.60	≦0.020	≦0.020	≦0.05
KSC82	0.80-0.85	0.15-0.30	0.40-0.60	≦0.020	≦0.020	≦0.05
KSC90	0.88-0.93	0.15-0.30	0.40-0.60	≦0.020	≦0.020	≦0.05
KSC92-E	0.90-0.95	0.10-0.25	0.30-0.50	≦0.020	≦0.020	0.10-0.30
KSC105-E	1.02-1.07	0.15-0.30	0.20-0.40	≦0.020	≦0.020	0.10-0.30

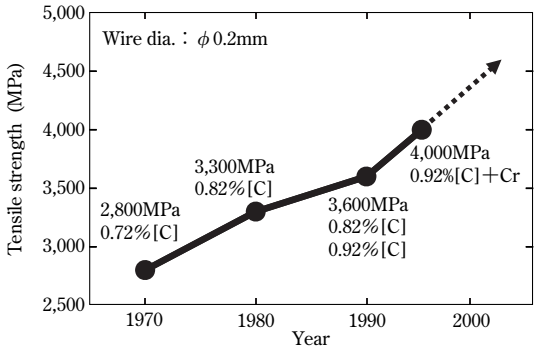

Fig. 2 Trend of high tensile strength of tire cord

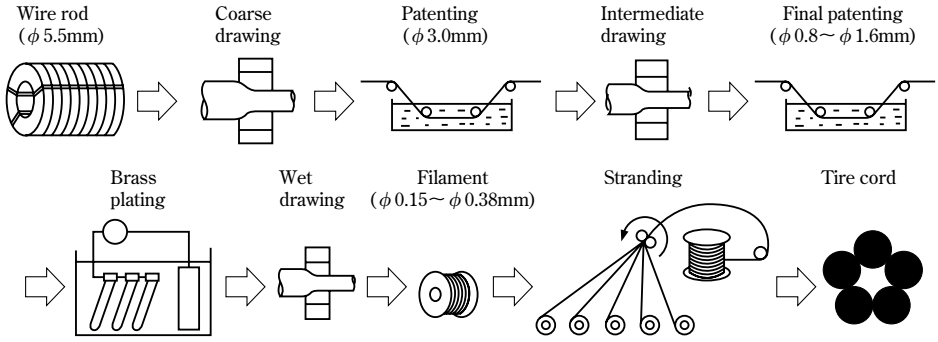

Fig. 3 Manufacturing process of tire cord[2)]

follows the microstructure of pearlitic steel which has a layered structure of ferrite and cementite. Steel cord has the highest strength among the mass produced materials in practical use. To make it stronger, the carbon content in the wire rod has been increased from 0.7% C (hypoeutectoid steel) to 0.8%C (eutectoid steel) and then to 0.9%C (hypereutectoid steel).

Fig. 3 depicts a typical manufacturing process of steel cord used for tire reinforcement[2)].

A hot-rolled wire rod with a diameter of φ5.5mm is processed according to the steps of dry wire drawing, intermediate patenting, brass plating and wet wire drawing, up to which point both the steel cord and saw wire are produced by almost the same process. The filaments that constitute steel cord have extremely small diameters of φ0.15 - φ0.38mm and are subjected to strong torsional stress during the wire-stranding step after the wet wire drawing. This can cause the filament to break, decrease productivity and degrade the filament quality. Therefore, stringent quality is required throughout the entire length of each filament.

A saw wire, on the other hand, is used as a solid filament and does not include a stranding step in its manufacturing process. The wire has an ultrafine diameter of φ0.08 - φ0.20mm to improve the yield of the material to be cut. In addition, the wire is repeatedly subjected to bending stress and tensile stress during cutting. Thus the tensile strength of a saw wire can reach as high as 4,000MPa (**Fig. 4**).

Fig. 5 shows the relationship between the tensile strength of a filament for steel cord and the wire breakage frequency (index) during the stranding step, showing a rapid increase in the breakage frequency as the strength increases.[3)] The cause of the breakage, attributable to the wire rod, includes surface scratches, centerline segregation and inclusions. In particular, an inclusion as small as several tens of microns can not only become the starting point for wire breakage (**Fig. 6**), but also affect the fatigue characteristics[4)]. Thus, the cleanness of the steel definitely affects the quality of wire

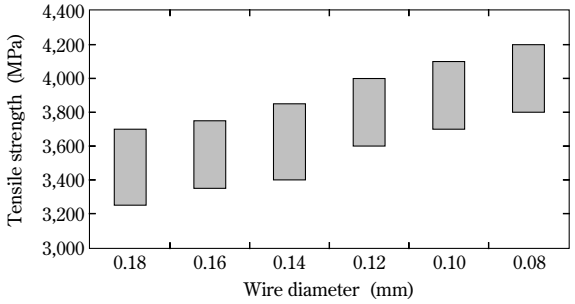

Fig. 4 Tensile strength of saw wire

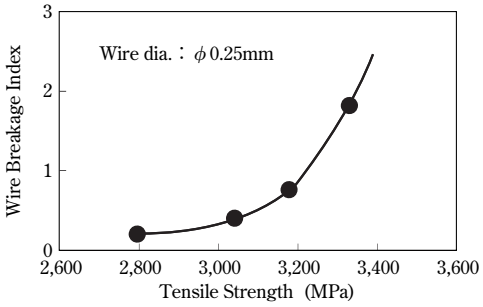

Fig. 5 Relationship between tensile strength of filament and wire breakage index during stranding process

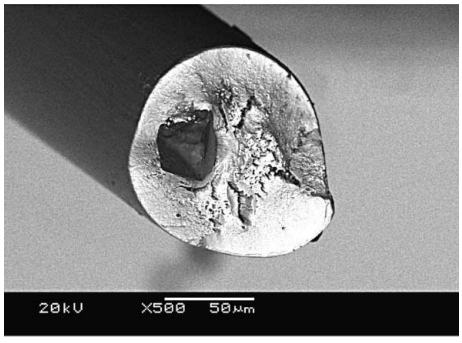

Fig. 6 Fracture surface of steel cord

rods for steel cord, and non-metallic inclusions must be further reduced to prevent the wire breakage associated with increased strength.

2. Challenge to attain zero-breakage

An inclusion that can cause wire breakage mainly consists of hard alumina, in particular, corundum (Al_2O_3) and spinel ($MgO \cdot Al_2O_3$), which are unlikely

to elongate and likely to fracture during hot rolling and cold working [5) - 7)].

Alumina can either crystallize out from molten steel, or originate from refractories. To avoid this, various measures have been implemented, including the prevention of Al from mixing into the molten steel, modification of the slag refining method and improvement of refractories.

(1) Prevention of Al adulteration

The concentration of dissolved Al in molten steel in equilibrium with a target composition is as low as several ppm. Therefore, the adulteration of Al, e.g., from alloy iron, must be controlled or restricted. Kobe Steel not only uses alloys with restricted Al concentration, but also has established a technology for suppressing Al in molten steel to a very low concentration by using a slag composition controlling technology during slag refining, as described later.

(2) Slag refining

Kimura et al. studied the fracture behavior of alumina, zirconia, zircon and silica, all of which are hard and have high melting points, during hot rolling and cold wire drawing [9)]. The micrographs in **Fig. 7** show the fracture behaviors of alumina and silica in hot rolled wire rods (ϕ5.5mm) and in the subsequent cold drawn wires [9)]. No significant difference appears in the fracture behavior of the hot rolled materials; however, in the cold drawn wire, silica, having lower compressive strength, is fractured into smaller pieces. Inclusions that are crystallized out from molten steel, or are adulterated from refractories, should be modified into glassy compositions with a lower melting point such that they can be fractured more easily.

Inclusions in wire rods for steel cord are roughly classified into a $CaO\text{-}SiO_2\text{-}Al_2O_3$ type having its origin in slag and a $MnO\text{-}SiO_2\text{-}Al_2O_3$ type having its origin in deoxidation products. **Fig. 8** shows the phase diagrams of the $CaO\text{-}SiO_2\text{-}Al_2O_3$ and $MnO\text{-}SiO_2\text{-}Al_2O_3$ systems. In both systems, the composition range in which the melting point becomes low enough for the compound to elongate during hot rolling, and thus become harmless, lies in the vicinity of the eutectic line between anorthite and pseudowollastonite and in the area surrounding the primary phase of spessatite. Kobe Steel has succeeded in preventing hard alumina from being crystalized out and in rendering the inclusions harmless by establishing a production technology for accurately controlling slag so that it meets a target composition during slag refining.

(3) Improvement of refractories

Refractories are indispensable for treating molten steel at high temperatures. However, refractories can cause wire breakage. Kobe Steel has established a technology for using refractories as materials for receiving molten steel so that the molten steel is maintained at maximum cleanness while retaining their strength and corrosion resistance.

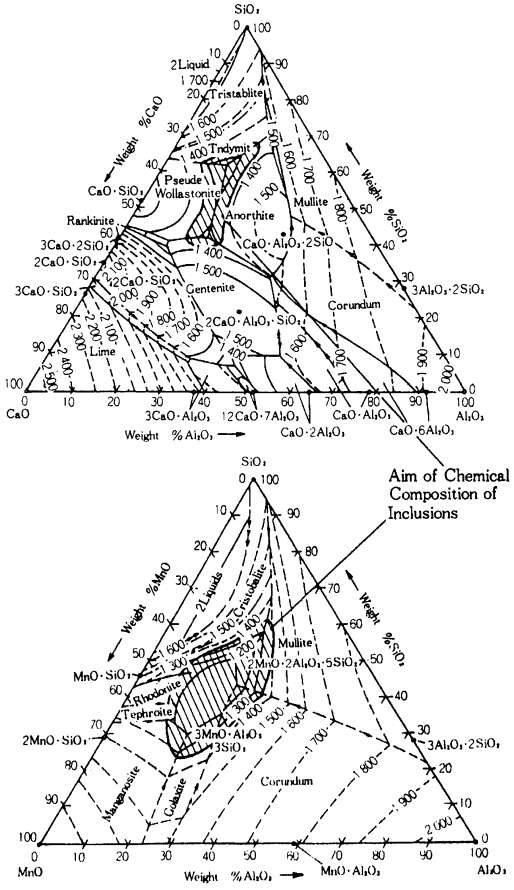

Fig. 8 Aim of chemical compositions of inclusions

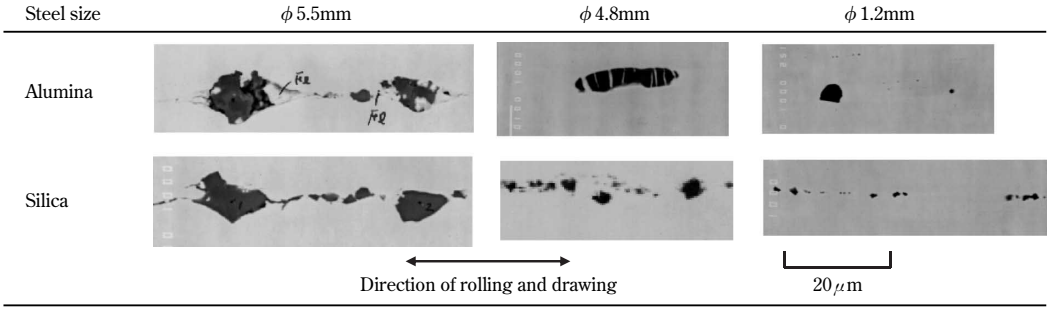

Fig. 7 Typical examples of change in shape of oxide inclusions appeared on longitudinal section of steel wire during drawing [9)]

3. High drawability - Development of new product

As described above, there is an increasing demand for stronger steel cord. Research and development in pursuit of the ultimate high strength are being done on steel cord with strength exceeding 4,000MPa.

On the other hand, for the purpose of reducing the production costs incurred by cord manufacturers, new methods are being developed for direct drawing and for improving the life of dies. Direct drawing does away with the intermediate patenting that exists in the primary wire drawing of conventional materials.

Kobe Steel has been pursuing wire rods with higher strength as well as with excellent drawability, which enables direct drawing and improves the life of dies.

An index for evaluating the drawability of a wire rod is the reduction of the area of the wire rod, in which a higher reduction of area is more suitable for wire drawing. It is also indispensable to decrease the tensile strength of wire rod by increasing the interval distance of lamellar pearlite, which enlarges the critical zone for wire drawing and increases the life of dies.

In general, the tensile strength and reduction of area of a wire rod are in a proportional relationship, in which the lower the strength is, the lower the reduction of area becomes. By combining controlled rolling and controlled cooling, Kobe Steel has developed a wire rod having excellent drawability with reduced tensile strength, while maintaining a high reduction of area.

A torsion test is performed to evaluate the soundness of wire, in which vertical cracking, called delamination, occurs when a wire embrittled by the wire drawing is twisted.

Fig. 9 compares the relationship between the true strain and the critical strain for delamination generation in a conventional steel to that of the newly developed steel. The newly developed steel exhibits no delamination at a higher wire drawing strain, demonstrating its excellent drawability.

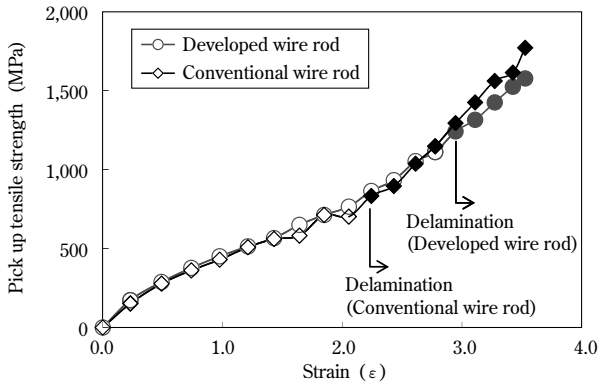

Fig. 9 Relationship between strain and delamination

4. Future prospects

With its excellent characteristics, steel cord for tires has been playing an important role in traveling performance with its features including driving stability and weight reduction, which improves fuel economy. As the world focuses on the reduction of the global environmental burden, exhaust gas regulation in automobiles will become even more stringent, requiring higher strength steel cord that enables a further weight reduction in tires.

Increasing the strength of steel cord is an effective means for reducing the weight of tires; however, increasing the strength of a material increases its defect sensitivity. Thus, further reduction is required for defects such as non-metallic inclusions, segregation and surface scratches.

On the other hand, competition in the manufacturing of steel cord has become increasingly intense, requiring materials that contribute to cost reduction and productivity improvement.

In addition, the market for solar energy generation will continue to grow, which will further enhance competition among saw wire manufacturers and ingot cutting manufacturers. Cuttability, assured by high strength, and cutting yield, assured by small wire diameter, require a wire rod with high strength and fewer defects that can cause wire breakage, as in the case of steel cord application.

Conclusions

Kobe Steel will strive to develop materials meeting the market needs and thus contribute to the growth of industries related to tires, automobiles and solar energy generation.

References

1) Y. OKI, *Bulletin of The Iron and Steel Institute of Japan*, Vol.8, No.9(2003), pp.627-632.
2) T. Minamida et al., *R&D Kobe Steel Engineering Reports*, Vol.50, No.3(2000), p.32.
3) Y. Yamada et al., *R&D Kobe Steel Engineering Reports*, Vol.36, No.4(1986), p.71.
4) M. Tomioka et al., *R&D Kobe Steel Engineering Reports*, Vol.23, No.3(1975), p.39.
5) A. Yoshimochi et al., *Wire Journal Int*., Sep(1983), p.224.
6) H. SATO et al., *SEITETSU KENKYU*, Vol.320 Jan., 1986, p.35.
7) E. Stampa et al., *Wire Journal Int*. Mar(1987), p.44.
8) T. Mimura, *183th Nishiyama Kinen Gijutu Koza*, 2004, pp.11-12.
9) S. Kimura et al., *Tetsu-to-Hagane*, Vol.88, No.11(2002), pp.755-762.

Characteristics of Brittle Crack Arrest Steel Plate for Large Heat-input Welding for Large Container Ships

Masahito KANEKO*1, Dr. Tokutaka TANI*1
*1 Plate Products Development Department, Research & Development Laboratory, Iron & Steel Business

Once it happens, brittle fracture in the hatch coaming parts around the deck openings of container ships causes serious structural damage that could potentially result in both fatalities and environmental damage. With this in mind, ships are designed and constructed so as to ensure that brittle crack does not occur. Further, if by chance it does occur, having a back-up function for arresting brittle crack included in the steel plate is essential. This report describes the characteristics of KE36 class brittle crack arrest plates. Improvement in brittle crack arrestability was achieved by the refinement of crystal grains, which is a result of strictly temperature-controlled TMCP (Thermo Mechanical Control Process).

Introduction

With the recent increase in the volume of marine transport, container ships are becoming larger. Now, very large ships that can carry more than ten thousand containers have been built. A container ship has a structure with a large opening on its upper deck and its hull girder constructed with an open cross-section. This requires container ships to have the highest longitudinal strength among large merchant ships. In order to ensure longitudinal strength while upsizing its hull, each container ship has a hatch side coaming surrounding its deck and an upper deck, both thickly built adopting steel plates no thinner than 50mm[1].

The interior of a thick plate, however, is in a plane strain state with the plastic region decreased in size. As a result, a stress greater than its yield stress is generated, and cracks propagate more easily. Brittle fractures, once occurring in the hatch coaming part around the deck openings of a container ship, can cause serious structural damage, with the potential for both fatalities and environmental damage. With this background, ships are designed and constructed so as to ensure that brittle crack does not initiate. Furthermore, in case a brittle crack should be initiated by chance, it is essential that a back-up brittle crack arresting function be included in the steel plates[2]. Many studies have been conducted on the crack-arrestability of steels. It is reported that a brittle fracture test, performed on a model test body simulating a T joint for a hatch side coaming and upper deck, gave a result indicating that a steel plate having a thickness of 60mm can serve as an effective crack arrester if it has a K_{ca} value (brittle crack propagation-arrest toughness) no smaller than 6,000N/mm$^{1.5}$ at a test temperature of -10℃ [3, 4].

However, only a few reports refer to the methods for producing such a heavy thickness in steel plates for hull structures, i.e., a plate thicker than 50mm and having high arrestability with a K_{ca} value (-10℃) exceeding 6,000N/mm$^{1.5}$.

In this development work, heavy-thickness steel plates were control rolled under optimum conditions with stringent roll control in the temperature zones that respectively cause recrystallization and non-recrystallization. As a result, a technique was established for producing a steel plate with a high arrestability with a K_{ca} value (-10℃) exceeding 6,000N/mm$^{1.5}$. This paper outlines an overview of the production technique and introduces the characteristics of the newly developed steel plate.

1. Development target

Table 1 shows the target properties to be achieved by this development work. The target mechanical properties for the base metal and welding joint are to meet the requirements of the Nippon Kaiji Kyokai (NK) standard, KE36.

The arrest characteristics of the base metal aim to satisfy the minimum brittle crack-arrest toughness at the test temperature of -10℃, K_{ca} (-10℃), to be no lower than 6,000N/mm$^{1.5}$, according to the "Guidelines on Brittle Crack Arrest Design" proposed by Class NK[4].

Table 1 Target properties

Grade	Thickness (mm)	Base metal properties				Arrestabilty	Properties of welded joints		
		YP (MPa)	TS (MPa)	EL (%)	vE$_{-40}$ (J)	K_{ca}(−10℃) (N/mm$^{1.5}$)	Welding method	TS (MPa)	vE$_{-20}$ (J)
KE36	60	≧355	490～620	≧21	≧34(Ave.) ≧24(Each)	≧6,000	1pass EGW*	490～620	≧34(Ave.) ≧24(Each)

*EGW (Electrogas welding)

2. Development concept

Improvement of arrest characteristics is known to be achieved by several techniques including: 1) refining the grain size of the surface layer to 1 - 3 μm [5]; and 2) balancing the grain refining and the deformation texture of ferrite [6].

This development work aims to establish a technique for producing a steel plate having arrestability with a K_{ca} value (-10℃) exceeding 6,000N/mm$^{1.5}$ by fully exploiting the capacity of the existing facilities.

As shown in **Fig. 1**, K_{ca} is reported to correlate with the toughness of a base metal at $t/4$ portion (fracture surface transition temperature $vTrs$)[7]. If there is no slip deformation, cracks in a steel material generally propagate along a crystal plane with a low surface energy before causing fracture[8]. Therefore, the toughness of the base metal can be effectively improved by increasing the grain boundaries having misorientation angles greater than 15 degrees. Such grain boundaries serve as resistance against brittle cracks [9]. Grain boundaries with misorientation angles greater than 15 degrees are here referred to as "high angle grain boundaries." It is important to refine grains surrounded by high angle boundaries to improve the toughness of the base metals, because such refinement is considered to result in the improvement of the arrest characteristics (K_{ca}≧ 6,000N/mm$^{1.5}$). In the case of heavy-thickness steel plates, however, the applicable rolling reduction is so limited and the temperature deviation in the thickness direction is so large that the conventional rolling technique will not allow rolling in the required temperature zones, making refinement difficult.

To resolve this issue, a technique called thermo mechanical control process (TMCP) was introduced. This technique enables an adequate control of the rolling reduction in the recrystallization and non-recrystallization temperature zones [10]. The technique was fine tuned for the rolling temperature regions and rolling reduction. More specifically, the conventional technique involves rolling continuously across the high temperature regions from the recrystallization temperature zone to non-recrystallization temperature zone. This conventional method is modified by incorporating steel plate cooling during the rolling to allow tighter temperature control. A study was conducted on the rolling in the low temperature region at a non-recrystallization temperature immediately above the Ar3 transformation point. The temperature is considered to facilitate grain refinement by effectively introducing strain (nucleation sites) to austenite grains.

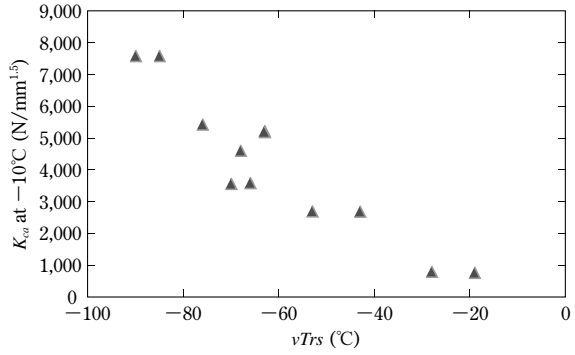

Fig. 1 Relationship between K_{ca} at −10℃ and $vTrs$ ($t/4$)

3. Features of newly developed steel

3.1 Chemical composition and mechanical properties of base metal

The chemical composition of the newly developed steel is shown in **Table 2**. To ensure toughness at low temperatures in the heat affected zone (HAZ) caused by high heat input welding, the C content is limited to 0.08% in order to prevent the toughness deterioration caused by island-shaped martensite. For this purpose, C_{eq} is maintained as low as 0.34%. A small amount of Ti is added to prevent the toughness deterioration caused by the coarsening of prior austenite grain. Furthermore, a small amount of Nb, which expands the non-recrystallization temperature zone, is added in order to promote the refinement of the grains surrounded by high angle boundaries.

The relation between the size of grains surrounded by high angle boundaries and K_{ca} (-10℃) was studied under various TMCP conditions. The result is shown in **Fig. 2**. As predicted, K_{ca} is

Table 2 Chemical compositions of developed steel

(mass%)

	C	Si	Mn	Ti	Others	C_{eq}
Developed Steel	0.08	0.12	1.55	0.012	Nb, B, Ca	0.34

C_{eq}=C+Mn/6+(Cr+Mo+V)/5+(Cu+Ni)/15

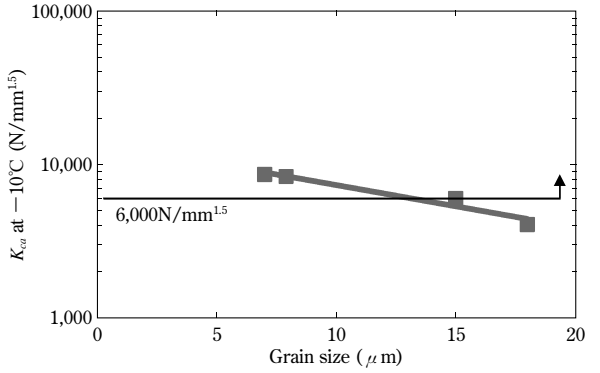

Fig. 2 Relationship between high angle grain size and K_{ca} at −10℃

improved by refining grains surrounded by high angle boundaries. By making these grains no larger than 10 μm, the target of K_{ca} (-10℃)≧6,000N/mm$^{1.5}$ was achieved.

Now, a study was conducted to establish a production technique for decreasing the grain size to under 10 μm while maintaining high angle boundaries to ensure arrest characteristics. **Fig. 3** shows micrographs and electron backscattering diffraction (EBSD) patterns mapping the crystal orientations at grain boundaries of newly developed and conventional steels[11]. The grains mapped are those surrounded by high angle boundaries with crystal misorientation greater than 15 degrees. The conventional steel has a structure mainly consisting of upper bainite. By introducing an adequate amount of strain in a low temperature range between the recrystallization temperature and non-recrystallization temperature, the newly developed steel is changed so as to have a structure mainly consisting of polygonal ferrite in which grains surrounded by high angle boundaries with crystal misorientation greater than 15 degrees are refined. This is attributable to the strain introduced at a low temperature between the recrystallization temperature and non-recrystallization temperature, which serves to form ferrite nuclei in the austenite grains and to promote the generation of polygonal ferrite[12].

Table 3 shows the base metal properties of the steel tested. The newly developed steel plate exhibits the mechanical properties that satisfy the target with vE$_{-40}$, greater than 340J, sufficiently exceeding the target value (34J). As shown in **Fig. 4**, the developed steel plate exhibits a favorable fracture surface transition temperature of lower than -90℃.

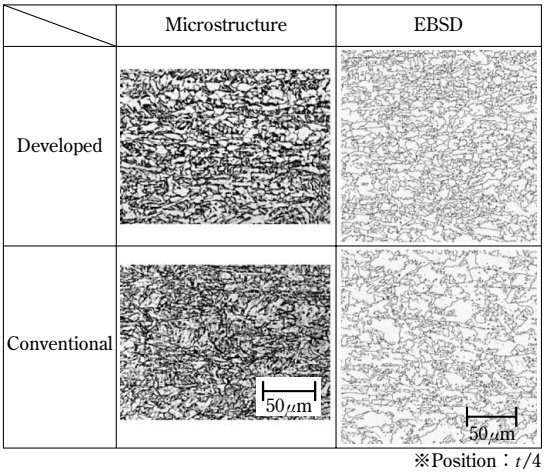

Fig. 3 Microstructure and grain boundary map with EBSD

3.2 Brittle crack propagation-arrest characteristics

Brittle crack propagation-arrest characteristics were evaluated by K_{ca} values, calculated from the results obtained by an ESSO test[5] specified by the Guidelines on Brittle Crack Arrest Design. **Fig. 5** shows the result of the ESSO test. By extrapolating the fitted line, the developed steel is expected to have K_{ca} exceeding 8,000N/mm$^{1.5}$ at the lowest use temperature (-10℃), which sufficiently satisfies the minimum brittle crack arrest toughness value K_{ca} (-10℃)≧6,000N/mm$^{1.5}$ specified by the Guidelines on Brittle Crack Arrest Design.

Fig. 6 shows an example of the fracture surface,

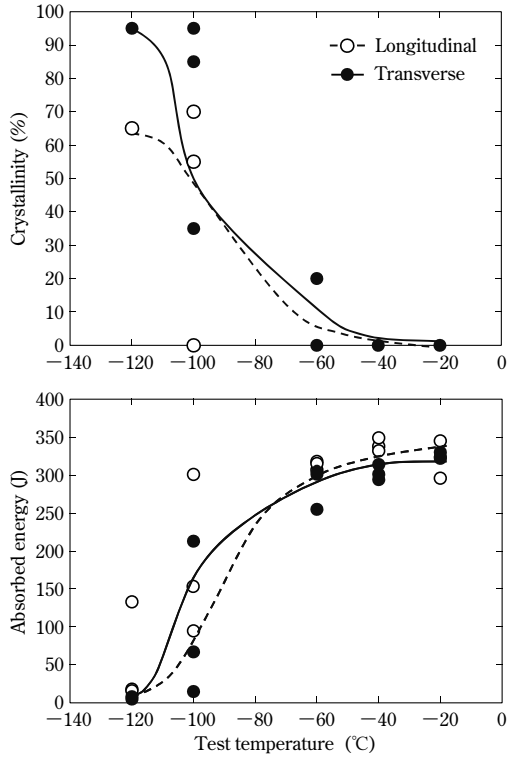

Fig. 4 Charpy transition curve of developed steel plate

Table 3 Mechanical properties of developed steels

	Thickness (mm)	Base metal properties				
		YP*1 (MPa)	TS*1 (MPa)	EL*1 (%)	vE$_{-40}$ (J)*2	*vTrs* (℃)
Developed Steel	60	425	538	31	340 (Ave.) 338, 332, 349 (Each)	−100
Conventional Steel	60	499	615	23	231 (Ave.) 235, 230, 229 (Each)	−60
KE36 Target properties	60	≧355	490～620	≧21	≧34 (Ave.) ≧24 (Each)	—

*1 Round tensile specimen：NK14A *2 Charpy test specimen：NKU4

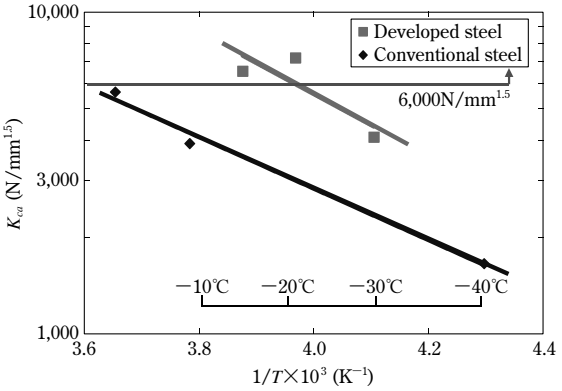

Fig. 5 Results of ESSO test

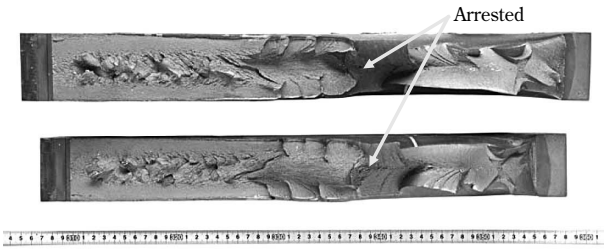

Fig. 6 Fracture surface of specimen after ESSO test

in which brittle crack is arrested as a result of toughness improvement associated with the temperature gradient. It is considered that, as a shear-lip extends from the surface layer to the interior ($t/8$ - $t/4$) of the steel plate, the driving force of brittle fracture becomes smaller than the kinetic fracture toughness value at the center of plate thickness. This serves to arrest the brittle crack[8]. The developed steel exhibits fracture surface having a shear-lip extending to $t/8$ - $t/4$. The plastic deformation at the shear-lip is considered to absorb energy for crack propagation, improving the arrest characteristics.

3.3 Characteristics of high-heat-input welding joint

High-heat-input welding is performed for assembling the hatch side coaming and upper deck of a container ship to assure high construction efficiency. To simulate the work done at these portions, electro-gas welding (EGW) with a single electrode was performed with high heat input. The welding conditions for the developed steel plate are shown in **Table 4** and the welding joint characteristics are shown in **Table 5**. The welding was performed with a high heat input of 450kJ/cm. The joint strength satisfies the target value. In addition, positive results were obtained regarding the joint toughness: a Charpy absorbed energy of 34J or more was achieved at all notch positions in the V-notch Charpy impact test at a test temperature of -20℃.

Table 4 Conditions of EGW

Thickness (mm)	Groove angle(°)	Root gap (mm)	Welding consumable	Number of passes	Welding current (A)	Welding voltage (V)	Welding speed (cm/min)	Heat input (kJ/cm)
60	20	8	Wire：DWS-1LG (ϕ1.6mm) Shielding gas：CO_2	1	400	43	2.3	449

Table 5 Mechanical properties of EGW welded joint

Thickness (mm)	Properties of welded joints					
	TS*1 (MPa)	Broken location	vE_{-20}min*2 (J)			
			Position	Depo	Bond	Bond+ 1mm
60	583	HAZ	Surface $t/2$ Back	113 91 108	208 204 207	199 203 182
KE36 Target properties	490 ～620	—	≧34(Ave.) ≧24(Each)			

*1 Round tensile specimen：NKU2A *2 Charpy test specimen：NKU4

Conclusions

An adequate amount of strain was introduced at a low temperature in the range between the recrystallization temperature and non-recrystallization temperature to produce a microstructure mainly consisting of fine polygonal ferrite. As a result, grains surrounded by high angle boundaries were successfully refined in a heavy- thickness steel plate having a thickness exceeding 50mm.

The results satisfy the minimum brittle crack arrest toughness value K_{ca} (-10 ℃)≧6,000N/mm$^{1.5}$ specified in the Guidelines on Brittle Crack Arrest Design. The developed steel responds to the need for larger and safer container vessels, which continue to be built. The demand for the newly developed steel is expected to grow rapidly.

References

1) H. SHIRAKIHARA, *Technology and Challenge in Application of Steel Material in Shipbuilding, NISHIYAMA KINEN GIJUTSU KOZA*, 2007-06.
2) Y. YAMAGUCHI, *KANRIN* (in Japanese), No.3, 2005, p.70.
3) E. TAMURA, CAMP-ISIJ, Vol.20, 2007, p.469.
4) Nippon Kaiji Kyokai, *Guidelines on Brittle Crack Arrest Design*, 2009.
5) T. Ishikawa, *Tetsu-to-Hagane*, Vol.85, No.7(1999), pp.544-551.
6) K. NISHIMURA, JFE GIHO, No.18, 2007, p.19.
7) E. TAMURA, CAMP-ISIJ, Vol.22, 2009, p.1315.
8) S. AIHARA, *NISHIYAMA KINEN GIJUTSU KOZA*, 177th, 2002, pp.159-160.
9) M. KANEKO, ISOPE, 2010.
10) M. KANEKO et al., CAMP-ISIJ, Vol.22, 2009, p.1315.
11) S. SUZUKI, *Materia Japan*, Vol.40, No.7(2001), p.612.
12) The Iron and Steel Institute of Japan, *Recent study on the banitic structure and its transformation behavior of (ultra) low carbon steel (in Japanese)*, 1994-07-30.

Effect of Steel Toughness on Brittle Crack Arrest Behavior of T-weld Joint Structure Using Thick Plates

Dr. Eiichi TAMURA*1, Dr. Tomokazu NAKAGAWA*2, Kazuyuki TSUTSUMI*2, Naohiro FURUKAWA*3
*1 Materials Research Laboratory, Technical Development Group
*2 Mechanical Engineering Research Laboratory, Technical Development Group
*3 Plate Products Marketing & Technical Service, Iron & Steel Business

Brittle crack arrest properties in ship construction have become more important as shipbuilding steel plates become thicker and stronger. There have been indications that steel toughness can have the effect of arresting brittle crack initiating in a welded joint; however the T-weld joints of an actual large structure have not been well investigated. This report describes how the brittle crack length and steel toughness were found to affect brittle crack arrest behavior. Furthermore, it was suggested that brittle crack could be arrested by using a horizontal plate of K_{ca} that would be sufficient even for the T-weld joint of an actual large structure.

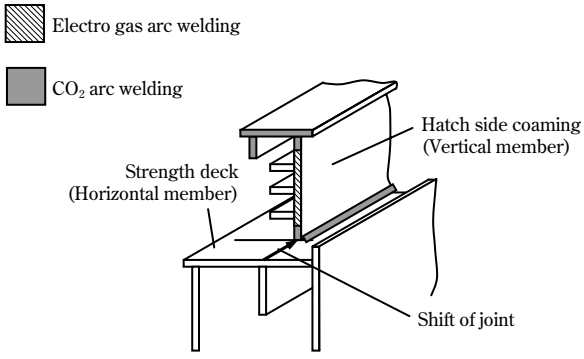

Fig. 1 Construction around hatch coaming

Introduction

The upsizing of container ships not only increases the allowable load and income per passage, but also decreases the number of crossings, which leads to the reduction of CO_2 emissions and contributes to the lessening of the environmental burden. The demand for marine transport is increasing with the recent rapid growth of East Asian economies such as that of China. This upsizing trend is more apparent for transport vessels such as container ships [1].

A container ship has an upper deck provided with a large opening and employs ultra-thick plates for the longitudinal strength members of its hull. As the ships are upsized, they require steel plates that are stronger and thicker [2]. According to an experimental result [1], a brittle crack, initiated in a high-heat-input welded portion of a thick plate, propagates straight along the welded portion. This poses a challenge when adopting thick plates and joining them to hull structures by high-heat-input welding. To satisfy the recent upsizing requirement for container ships while assuring safety, brittle cracks must be arrested without fail before they propagate along the high-heat-input welded portions of thick plates.

As shown in **Fig. 1**, a container ship has an upper deck (strength deck), a hatch side coaming and a T-weld joint that connects the hatch side coaming (a part of the longitudinal stiffening member) with the upper deck. In this construction, a brittle crack propagating straight along a welded portion of the hatch side coaming can be arrested by the base material of the upper deck, if the base material has sufficiently high crack-arresting performance (brittle crack arrestability), and if the positions of welded joints are shifted away from each other in such a way that the crack collides directly with the base material of the deck. Several studies have been conducted on this possibility [3)- 6)]. Studies conducted by the authors indicate that brittle cracks can be arrested by constructing the strength deck with a steel plate having a brittle crack arrestability (K_{ca}) exceeding a certain level [5), 6)]. These studies, however, have been conducted on small dimensional scales simulating the actual hull structure, leaving unclear the K_{ca} for steel plates that can arrest the long and large cracks that may occur in actual hull structures.

Hence, large specimens were prepared, each simulating a T joint between a hatch side coaming and strength deck. Brittle fracture tests were performed on these specimens while varying the specimen dimensions and the K_{ca} of the plate simulating the strength decks. The performance of arresting long and large brittle cracks was studied, as reported in this paper.

1. Testing procedure

1.1 Specimen shape

Three types of specimens (specimens 1 - 3, as shown in **Fig. 2** (a)-(c)) were prepared by welding steel plates having a thickness of 60mm. Each specimen had a horizontal member simulating a strength deck and a vertical member simulating a hatch side coaming. Full penetration welding was performed to join the vertical member with the horizontal member to simulate a T joint between a hatch side coaming and strength deck. Experiments

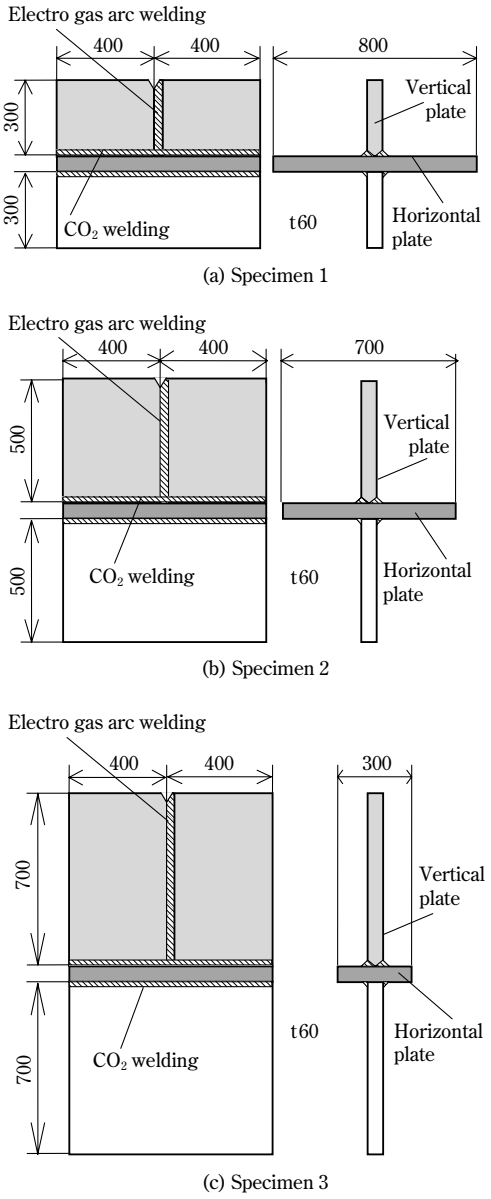

Fig. 2 Dimension of specimens (Unit：mm)

were conducted on these three types of specimens, each having different dimensions, so as to study the effect of crack length reaching the horizontal plate. Each vertical member was made of two steel plates butt-welded by electrogas arc welding (EG welding). The vertical members were welded to the horizontal members by CO_2 welding with full penetration. **Table 1** summarizes the welding conditions, and **Fig. 3** shows a typical cross-sectional macro structure of the full-penetration welded joint.

1.2 Steel plates used for testing

The vertical member was made of the same steel (steel plate A) as reported previously (YS = 520MPa, TS = 619MPa)[6]. In this study, two types of steel plates (Steel plates B and C), having different K_{ca}, were used

Table 1 Welding condition for specimen 1

Electro gas arc welding	Welding method	Electro gas arc welding
	Welding consumables	DWS-1LG/ ϕ 1.6mm, CO_2
	Welding conditions	Heat input：35kJ/mm
Full penetration welding	Welding method	CO_2 arc welding
	Welding consumables	DW-55E/ ϕ 1.2mm, CO_2
	Welding conditions	Welding current：190～236A Welding voltage ：23～29V Welding speed：18～60cm/min

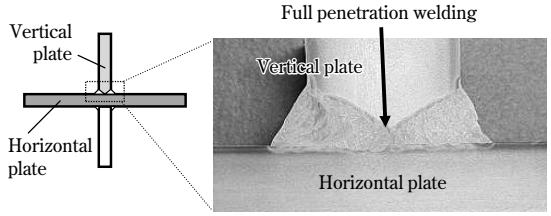

Fig. 3 Cross section of T-weld joint of specimen 1

Table 2 Steels used for the specimen (Steel A was used for vertical plate)

Specimen	Dimension of Specimen	Horizontal plate (Upper deck)
		K_{ca} at −10℃ (N/mm$^{3/2}$) (Material)
1	Fig.2(a)	4,200 (N/mm$^{3/2}$) (Steel B)
2−1	Fig.2(b)	
2−2		7,360 (N/mm$^{3/2}$) (Steel C)
3	Fig.2(c)	

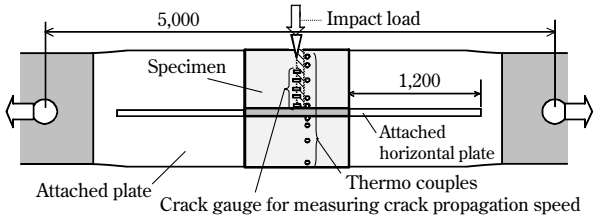

Fig. 4 Schematic illustration of experiment for T-weld specimen

for horizontal members to study the effect of the K_{ca} values of the horizontal steel plates. The K_{ca} values at -10℃ of the steel plates B and C were 4,200N/mm$^{3/2}$ and 7,360N/mm$^{3/2}$, respectively. Steel plates B and C are both in the same strength class. **Table 2** shows the specimen numbers and the steel plates used for each specimen.

1.3 Testing method

A tensile testing machine with a maximum load of 30MN was used for the test. **Fig. 4** illustrates the testing method. A jig was disposed between the testing machine and a specimen to apply homogeneous stress to the specimen. The temperature of each specimen was monitored using thermocouples

affixed to it at several locations. Each specimen was homogenized at a set temperature of -10℃ for more than 30 minutes before the test. The tensile load was controlled so as to make the average strain, determined by strain gauges affixed to several location of the horizontal plate, become 257MPa (i.e., the design stress of a strength deck).

Under the above conditions of temperature and loading, an impact load was applied to the notched portion on the top of each specimen to initiate a brittle crack.

In a case where the propagation rate of brittle crack is not high enough, the load applied to the specimen may decrease after the initiation of the brittle crack, which affects the test result. Therefore, an additional strain gauge affixed to the jig was used for this test, so that the load behavior after brittle crack initiation could be monitored by measuring the strain on the jig.

2. Test results

2.1 Brittle crack propagation behavior in vertical member

In all of the above tests, brittle cracks propagated along the EG weld portions immediately after the cracks were initiated. The crack propagation rate, immediately before the brittle cracks reached the T joint, was measured to be 500-700m/s. The strain gauges placed on the jig showed no load reduction that affected crack propagation.

2.2 Brittle crack arrest behavior of horizontal plate

Fig. 5 (a)-(d) shows the fracture surfaces after the tests. It should be noted that, in the case where the horizontal member did not break, it was ductile-fractured forcefully by applying a tensile load after the test.

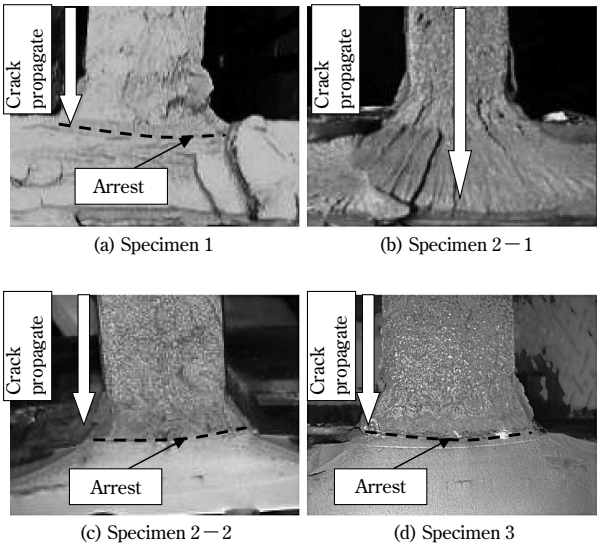

(a) Specimen 1 (b) Specimen 2－1

(c) Specimen 2－2 (d) Specimen 3

Fig. 5 Test results (fracture surface)

In the case of Specimen 1 (vertical plate height (H)=300mm: horizontal plate, Steel plate B), the brittle crack propagated along the EG weld portion of the vertical plate and propagated further into the horizontal plate via the T joint portion, as shown in Fig. 5(a); however, the extent of the propagation was small compared with the thickness of plate B, showing that the brittle crack was arrested immediately after its propagation into steel plate B.

In the case of Specimen 2-1 (H = 500mm: horizontal plate, Steel plate B), the brittle crack propagated to the end of the horizontal member without being arrested (Fig. 5(b)).

In the case of Specimen 2-2 (H = 500mm: horizontal plate, Steel plate C), the brittle crack propagated about 6~8mm into Steel plate C via the T joint and was arrested (Fig. 5(c)).

In the case of Specimen 3 (H = 700mm, horizontal plate: Steel plate C), the brittle crack propagated about 6~8mm into Steel plate C via the T joint and was arrested (Fig. 5 (d)).

3. Factors affecting brittle crack arrest characteristics

3.1 Discussion on the effect of K_{ca} of steel plate for horizontal plates

Specimen 2-2 arrested the crack, unlike Specimen 2-1, despite the fact that they both have the same shape (H = 500mm). This is attributable to the K_{ca} of the horizontal steel plate of Specimen 2-2 being higher than that of Specimen 2-1. The K_{ca} of the horizontal steel plate significantly affects the brittle crack arrest characteristics at the T joint of the horizontal plate.

3.2 Discussion on the effect of specimen dimensions (brittle crack length)

3.2.1 Comparison of Specimens 1 and 2-1

The brittle crack propagated in Specimen 1 (H = 300mm) was arrested as soon as it collided with the horizontal plate. On the other hand, the brittle crack in Specimen 2-1 (H = 500mm) was not arrested, although its horizontal plate had the same K_{ca} as that of Specimen 1. The difference is considered to be due to the difference in the height H of the vertical plates. Specimen 2-1 had a vertical plate with a larger H, which made the stress intensity factor at the crack tip, K value, larger than that of Specimen 1 when the crack reaches the horizontal plate. The stress

intensity factor exceeded the K_{ca} of the horizontal plate, causing the crack to propagate.

3.2.2 Comparison of specimens 2-2 and 3; possibility of arresting even longer and larger brittle crack

In the case of Specimen 3, the crack was arrested despite the fact that the crack, when it reached the horizontal plate, was longer than the crack in Specimen 2 - 2. This is considered to be caused by the K value at the crack tip still being smaller than the K_{ca} of the horizontal plate even under the conditions of the crack in Specimen 3.

According to Machida et al.[7], a rapidly propagating brittle crack suppresses the formation of a plastic region, making the K value almost constant for the increase of the crack length (a saturation phenomenon). If the K value of Specimen 3 is saturated, exhibiting the same saturation phenomenon, there should be no increase in the K value even for longer and larger cracks. If this is the case, cracks should be arrested by using Steel C for the horizontal member. The behavior of the crack in this saturation phenomenon in K value, however, has not been fully understood because of the difficulty in evaluating the K value at the tip of the brittle crack. This study attempts to evaluate this saturation behavior in K value of a brittle crack that propagates in a vertical member during the T joint test. Measurements were conducted using a strain gauge to discuss the characteristics required for a horizontal member arresting a long and large brittle crack.

4. Steel plate characteristics required for arresting long and large brittle cracks

4.1 Study on the saturation behavior of K value

To study the saturation behavior of K value during brittle crack propagation, a strain gauge is affixed in the vicinity of the weld portion (i.e., the crack propagation path) of Specimen 3 to evaluate the strain when the crack passes (**Fig. 6**). The strain distribution in the vicinity of a crack tip is considered to vary corresponding with the K value at the crack tip. So the behavior of the K value is discussed from the aspect of strain behavior.

Fig. 7 shows an example of the values measured by the strain gauge. Also included in this figure is the time period (evaluated by a crack gauge measurement) during which the brittle crack passed right beside the strain gauge. This figure indicates that the strain value reached a maximum immediately before the brittle crack passed right beside the strain gauge. This is considered to be caused by strain that is

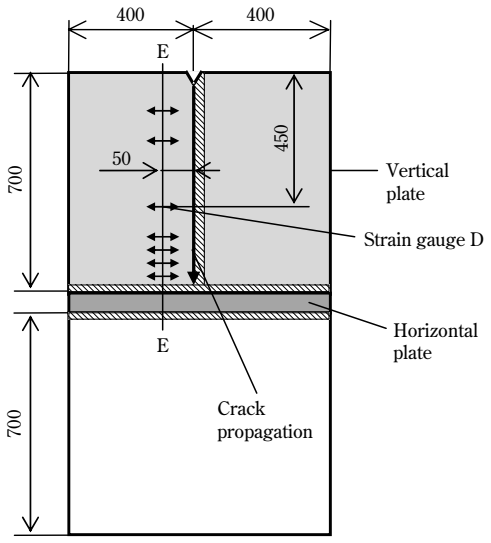

Fig. 6 Schematic illustration of strain gauge measurement along crack path

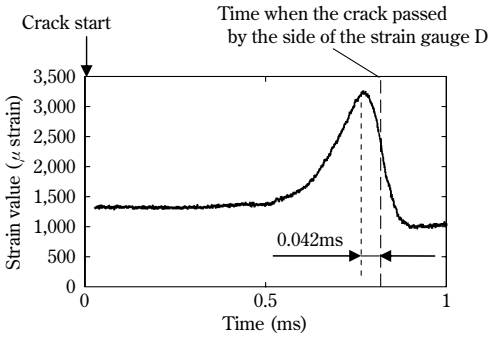

Fig. 7 Strain behavior of strain gauge D in Fig.6

higher diagonally in front, rather than right beside, the crack in the vicinity of a crack tip. As shown in Fig. 7, the difference between the time when the strain reached a maximum and the time when the crack passed right beside the strain gauge was about 0.042ms, which corresponds to a crack propagation length of 26.7mm, considering the crack propagation rate (636m/s for an equivalent crack length) measured simultaneously. The distance between the crack tip and the position where the strain maximizes is calculated, according to the linear fracture mechanics, to be 20mm in the crack propagation direction, assuming the positional relationship of this study (i.e., the strain measured at a point 50mm from the side of the crack path). This calculated value is essentially the same as the measurement result, verifying the validity of the evaluation, using strain measurement, of the strain distribution in the vicinity of a crack tip.

Here, the maximum strain value was first determined from the values measured by the strain gauges, then, the crack length which gives the maximum strain was estimated from the strain

propagation rate to establish the relationship between the maximum strain and crack length.

4.2 Results of strain measurement

Fig. 8 shows the relationship between the maximum strain measured and the crack length. Fig. 8 shows a tendency for the maximum strain measured to become almost constant when the crack length exceeds about 500mm. Also shown is a phenomenon in which the strain drops rapidly at a point right before (about 50mm before) the crack reaches the horizontal plate.

These measured results were compared with a finite element method (FEM) analysis performed on Specimen 3. **Fig. 9** shows the analysis model. Here, a 1/2 (half) structure in z-direction was modeled using solid elements. The horizontal plate was divided into three elements, and the vertical plate into six elements, in the plate thickness direction. The adjacent area of the crack propagation was segmented with meshes as small as 5mm at the minimum, to improve the accuracy of the calculation. A model crack (crack length, 0-700mm: crack tip, linear) was introduced, penetrating the plate thickness at the upper end of the vertical plate.

It should be noted that brittle cracks propagate at high velocities (maximum 700m/s in Specimen 3), making the materials through which the cracks propagate deform very rapidly. As a result, the yield strength of the material surrounding a crack tip becomes very high due to the effect of strain rate dependence, and the crack opening becomes very

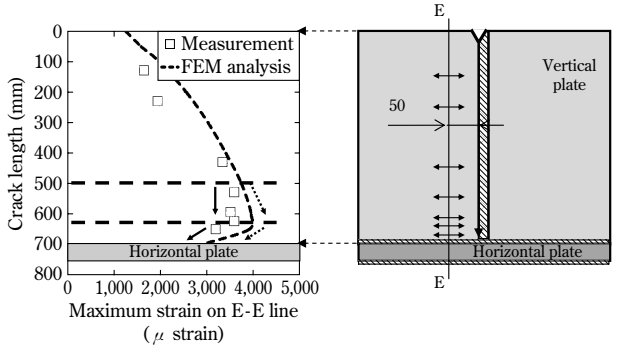

Fig. 8 Relationship between crack length and maximum strain on E-E line in Fig.6

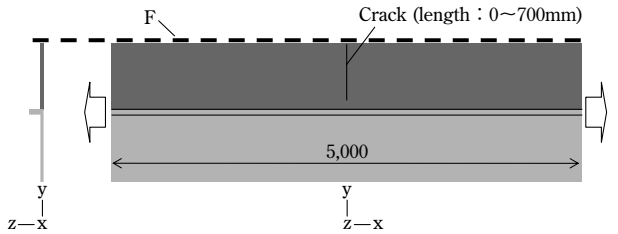

Fig. 9 FEM analysis model for specimen 3

small. To statically simulate this condition, in many cases the original single-edge cracked specimen is converted into a center-cracked specimen for elastic calculation. In this study, a static elastic analysis was conducted on the specimen converted into a center-cracked one with the symmetry boundary condition at the F portion in Fig. 9 (corresponding to the upper end of the specimen). This calculation assumes that a constant load is applied in the arrow direction at the end of the analysis model as shown in the figure, such that the nominal stress becomes 257MPa. The specimen length in the load direction was 5,000mm, which matches the distance between the loading points at the time of experiment illustrated in Fig 4. An analysis solver, ABAQUS6.5[8], was used.

The maximum values for strain in the x direction at each point / position corresponding to the location where a strain gauge was affixed (on the line E-E in Fig 6) were determined from the analysis result in order to examine their relationship with the crack length. The results are shown by the dashed line in Fig 8. As described previously, this study conducted a static elastic analysis for a high speed deformation behavior, and the analysis result did not quantitatively match the measured result. However, the analysis is considered to allow a qualitative comparison with the measured result. As shown in Fig. 8, the analysis result shows a rapid decrease in strain immediately before (about 50mm before) the crack reaches the horizontal plate, the same decrease as measured, indicating that the rigidity in front of the crack tip is increased by the horizontal plate. On the other hand, no strain saturation phenomenon, as observed in the actual experiment, exists in the simulated result in the crack length range of 500mm or longer.

The strain distribution at a crack tip is significantly affected not only by crack length, but also by the crack propagation rate. The strain saturation behavior observed in this study might also have been affected by the rapid crack propagation. To clarify the effect of the propagation rate of a brittle crack, the relation between the brittle crack propagation rate (measured by a crack gauge) and crack length in Specimen 3 is summarized in **Fig.10**. This figure indicates that a brittle crack longer than about 200mm propagates stably at a high rate of about 630-720m/s. In Fig. 8, the measured strain value becomes almost constant in the crack length range of about 500-620mm. In Fig.10, no significant change in the crack propagation rate is observed in the same crack length range, indicating no significant change occurring in the crack propagation behavior itself. In Fig.10, the crack propagation rate increases by about 50m/s for a crack length of 630mm, implying some effect on the periphery of the crack tip, however, no significant

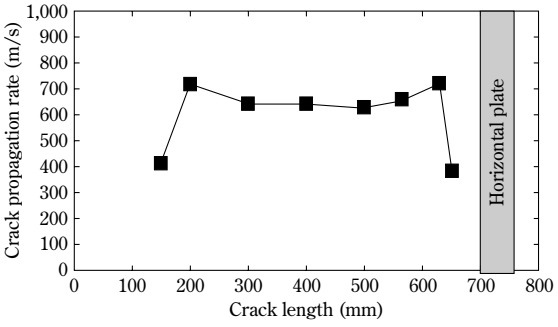

Fig.10 Relationship between brittle crack propagation rate and crack length

increase in the crack propagation rate is observed for the a crack length of 566mm. As shown in Fig. 8, strain saturation behavior is observed for a crack length of 500mm-620mm. The change in the crack propagation rate, observed in the same region in Fig.10, is not considered to affect the strain saturation behavior.

4.3 Saturation behavior of *K* value and the characteristics required for steel

From the previous results, it can be concluded that the strain saturation phenomenon observed in the actual measurements does not correlate with the change in the brittle crack propagation rate and has no link to brittle crack propagation behavior. Kinetic effect, which cannot be taken into account in FEM static elastic analysis, is considered to have affected the result. As described above, the strain distribution in the vicinity of a crack correlates well with the *K* value of the crack tip, and thus the *K* of the crack tip in Specimen 3 may also have been saturated. Assuming that this agrees with the above mentioned comment by Machida, *K* values will saturate to the same value for longer and larger cracks, meaning that brittle cracks can be arrested by using Steel plate C for the horizontal plate (e.g., strength deck) as in the case of Specimen 3.

Conclusions

A study was conducted using large joint specimens, each simulating a joint between a hatch side coaming and strength deck. The focus was put on the effect of the properties of a horizontal plate (simulating a strength deck) on the arrest characteristics of brittle cracks generated in the weld portion of a vertical plate (simulating a hatch side coaming), taking into account the size of the specimen.

The following describes the knowledge obtained:

- For the horizontal steel plate, K_{ca} and specimen dimension (brittle crack length) significantly affect the crack arrest performance. Steel C (K_{ca} = 7,360N/mm$^{3/2}$) exhibits crack arrest even for the largest specimen used in this study.
- A strain measurement conducted during the testing of Specimen 3 confirmed that the strain in the vicinity of a crack tip crack becomes saturated during crack propagation once the crack reaches a certain length.
- The strain in the vicinity of crack tip is considered to correlate with the *K* value. The brittle crack propagation test conducted on Specimen 3 indicates that the *K* value can possibly be saturated during crack propagation.
- From the above, cracks longer and larger than the ones studied this time can possibly be arrested by a horizontal plate (e.g., strength deck) made of a steel having adequate brittle crack arrest characteristics.

References

1) Y. YAMAGUCHI, *Kanrin*, No.3, (2005), p.70.
2) S. OHKITA, *Welding Technology*, 2007-3, (2007), p.65
3) T. INOUE et al., *Conference Proceedings JASNAOE*, Vol.3 (2006), p.359.
4) T. HANDA et al., *Conference Proceedings JASNAOE*, Vol.4 (2007), p.459.
5) E. TAMURA et al., *Conference Proceedings JASNAOE*, Vol.4 (2007), p.455.
6) E. TAMURA et al., *R&D KOBE STEEL ENGINEERING REPORTS*, Vol.58, No.1(2008), p.8.
7) S. MACHIDA et al., *Journal of the Society of Naval Architects of Japan*, Vol.131, (1972), p.367.
8) *ABAQUS/Standard User's Manual*, Hibbit, Karlsson & Sorensen, Inc., 1999.

Effects of Ca Addition on Formation Behavior of TiN Particles and HAZ Toughness in Large-Heat-Input Welding

Taku KATO*1, Shinsuke SATO*2, Dr. Hiroki OHTA*2, Toyoaki SHIWAKU*3
*1 Plate Products Development Department, Research & Development Laboratory, Iron & Steel Business
*2 Ironmaking & Steelmaking Development Department, Research & Development Laboratory, Iron & Steel Business
*3 Shinko Research Co., Ltd.

A new process technique, Kobe super toughness (KST), enables maintaining excellent toughness in heat affected zones (HAZs) formed by large heat input welding. In order to improve the KST treatment, the effect of Ca addition on HAZ toughness was studied with focus on TiN particles. It was found that Ca addition inhibits the crystallization of coarse TiN particles and increases the number of fine TiN particles precipitated. Consequently, a fine-grained microstructure of HAZ was achieved and HAZ toughness was improved significantly.

Introduction

Heavier gauge steel plates are more and more being used, with the recent increase in the size of steel structures such as container vessels and buildings. Welding such heavy gauge steel plates requires increased number of passes, making conventional multi-pass welding highly inefficient. Therefore, ultra-high-heat-input welding, such as electrogas arc welding and electroslag welding, which enable one-pass welding, is being increasingly used. The increased welding heat input, however, keeps the heat-affected zones (HAZs) of the welds at a high temperature for an extended period of time, as well as decreasing the cooling rate. This coarsens the microstructure and significantly decreases toughness.

To resolve such issues, Kobe Steel developed a process technique, Kobe Super Toughness (KST).[1] This technique enables the refinement of microstructure with a minor addition of Ti to disperse fine TiN particles, which suppress the coarsening of austenite (γ) grains in HAZs and serve as transformation nuclei for intragranular ferrite (α). This ensures favorable toughness in ultra-high-heat-input welded joints in HAZs, providing steel with a high degree of safety.

The requirement for HAZ toughness, on the other hand, is becoming increasingly stringent, which calls for further improvement of the KST technique. There are reports that HAZ toughness can be improved by utilizing CaO and CaS, along with TiN, as transformation nuclei for intragranular α[2), 3)]. Kobe Steel has also confirmed that the addition of Ca improves HAZ toughness[4]. However, not much detailed study has been done on the effect of Ca addition on HAZ toughness and on TiN particles, leaving much unknown. Therefore, a detailed study was conducted to ascertain how Ca addition affects particle size and the number of TiN particles. Based on the knowledge obtained, the amount of Ca to be added was optimized for HAZ toughness and the improvement effect was verified. The following is an outline of this study.

1. Experimental procedure

Table 1 shows the chemical compositions of the steels tested in this study. Calcium mainly serves to form oxide. The addition of Al, another oxide-forming element, which is similar to Ca, was varied to vary the amount of dissolved oxygen which affects oxide formation. Each composition was melted in a 150kg vacuum melting furnace and was cast in an ingot having a diameter of 250mm and a height of 400mm. Each ingot was heated to 1,100℃ and hot rolled into a plate 50mm thick. The temperature at the completion of the hot rolling was adjusted so as to be 850℃.

Inclusions in each ingot were observed to study the effect of Ca addition on the crystallization of TiN. The observations were conducted at intermediate positions between the ingot surface and the center. A field emission electron probe micro-analyzer (FE-EPMA) was used to observe the inclusions, to analyze the composition of inclusions larger than 2μm and to determine the particle size of TiN. Each particle size of TiN was given by the diameter of a circle whose area is equal to the area occupied by the TiN in each inclusion.

To study the effect of Ca addition on the precipitation of TiN in a HAZ, a heat cycle test, called a synthetic weld thermal cycle, which reproduces and simulates ultra-high-heat-input welding, was conducted on rolled steels with the additive amount of Al fixed at 0.03%. The heat cycle was applied to specimens, each of which was taken from the mid-

Table 1 Chemical compositions of steels (mass%)

C	Si	Mn	Al	Ti	Ca	N	others
0.08	0.35	1.55	0.013～0.058	0.015	0～0.0022	0.0060	Cu, Ni, B

plane between the rolled surface and the center plane of a plate. To reproduce the welding conditions, these specimens were heated to 1,400℃, held at that temperature for 30 seconds and then cooled in such a way that the temperature went from 800℃ to 500℃ in 730 seconds.

After the synthetic weld thermal cycle, inclusions larger than 2μm were measured for their TiN content by the FE-EPMA. The number density of TiN precipitates smaller than 300nm was determined using a transmission electron microscope (TEM).

2. Experimental results

2.1 Effect of Ca addition on crystallization of TiN in ingots

Fig. 1 shows typical inclusions observed by the FE-EPMA. Steel with no addition of Ca exhibits coarse TiN particles with sizes of around several microns, which have been nucleated from Al_2O_3. The steel with added Ca, on the other hand, exhibits complex oxides consisting of Al and Ca, with CaS surrounding the complex. Almost no crystallization of TiN was observed.

Fig. 2 shows the relation between the CaO content in the oxides and the size of TiN particles

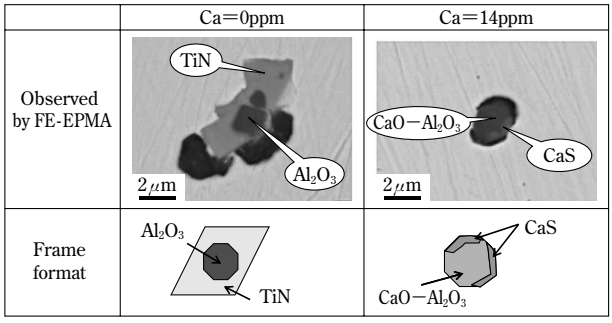

Fig. 1 Effect of Ca on inclusion morphology [5)]

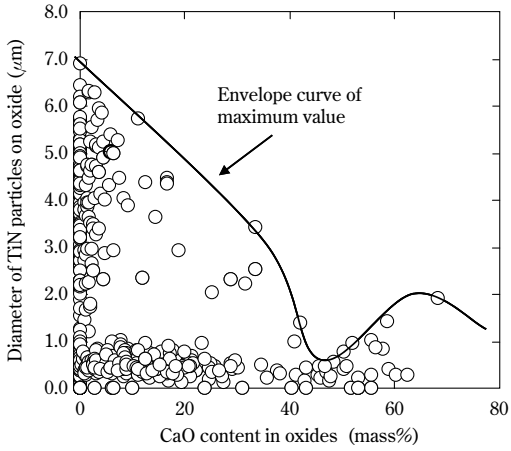

Fig. 2 Effect of CaO content in oxides on diameter of TiN particles

crystallized on these oxides. It should be noted that all the oxides in these compositions consist essentially of CaO and Al_2O_3, or in other words, the remainder of CaO is almost entirely Al_2O_3. As a whole, the particle size of TiN decreases with the increase in CaO content. The size of TiN particles rapidly decreases in the CaO concentration range of about 40-60% and reaches a minimum at about 50%.

Fig. 3 shows the relationship between the CaS content and the TiN content in the inclusions. The TiN content decreases rapidly with the increase in CaS content, and almost no TiN crystalizes out in the CaS content range higher than 20%.

2.2 Effect of Ca addition on TiN precipitation in HAZ

Fig. 4 shows the effect of Ca addition on the TiN content in the inclusions larger than 2μm and on the number density of fine TiN smaller than 300nm. With the increase in the amount of Ca added, the TiN content in the inclusions larger than 2μm decreases, while the number density of fine TiN increases. This is considered to be caused by the increased addition

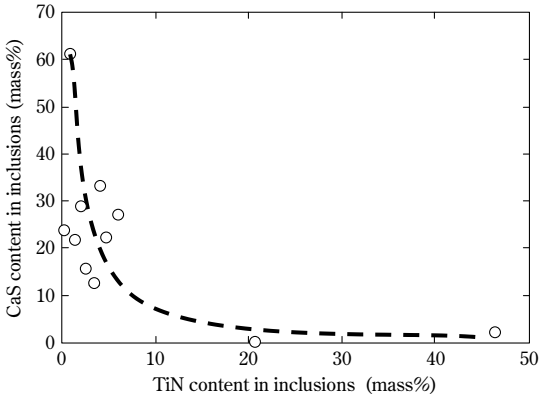

Fig. 3 Relationship between TiN content and CaS content in inclusions

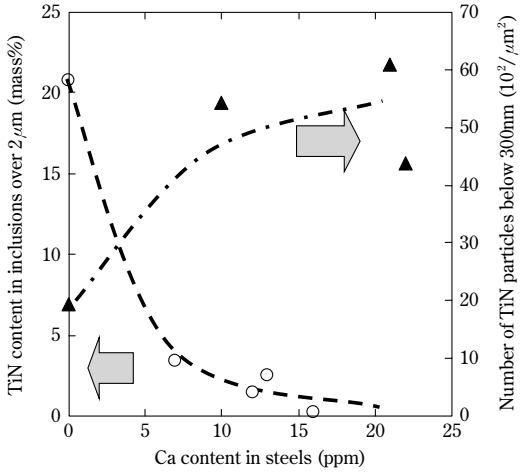

Fig. 4 Effect of Ca content in steels on coarse TiN particles and fine TiN particles

of Ca suppressing the crystallization of coarse TiN on the oxides, resulting in a large portion of TiN finely precipitated.

3. Discussion

As shown Fig. 1, TiN crystallizes out preferentially on Al_2O_3, but not on CaS or on CaO-Al_2O_3. In order to evaluate how easily TiN can crystallize out, the lattice misfits agsinst TiN and critical nucleus formation energies of CaO, CaS and Al_2O_3 were calculated according to the method proposed by Aaronson, J.H.Van Der Merwe, Jimbo and Morikage et al.[6) - 8)] The results are shown in **Fig. 5** and **Fig. 6**. Here, the critical nucleus formation energy is standardized by the nucleus formation energy of Al_2O_3 for comparison. Moreover, for the calculation, the interface energy was assumed to be the same as the structural energy. The result indicates that CaS has the largest lattice misfit against TiN, while Al_2O_3 and CaO have almost the same level of lattice misfit. The critical nucleus formation energy was the largest for CaS and the smallest for CaO. Therefore, from the aspects of lattice misfit and critical nucleus formation energy, CaS is least likely to become the nucleus for the crystallization of TiN. This is considered to have caused the rapid decrease of TiN content with the increase of CaS content, as shown in Fig. 3. Among the three compounds, CaO is the most likely to become the nucleus for the crystallization of TiN. However, as shown in Fig. 2, the particle size of TiN tends to decrease as the CaO content increases. This is considered to be caused by the increased addition of Ca, which not only increases the CaO content, but also increases the concentration of CaS, which is unlikely to become the nucleus for the crystallization of TiN. This is considered to have caused CaS, having critical nucleus formation energy smaller for CaO than for TiN, to be formed around the oxide as shown in Fig. 1, decreasing the area of contact between the molten steel and CaO.

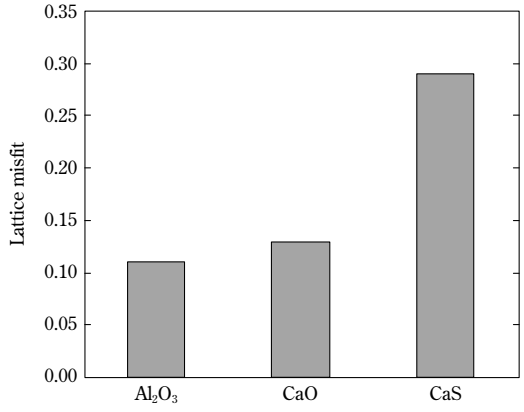

Fig. 5 Lattice misfit between TiN and inclusions

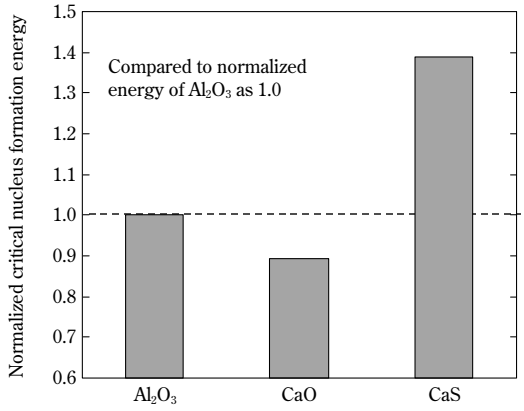

Fig. 6 Critical nucleus formation energy between TiN and inclusions

The following discusses the phenomenon, as shown in Fig. 2, in which the particle size of TiN decreases rapidly in the CaO concentration range of 40-60%. In order for oxides to serve as the nuclei for the crystallization of TiN, it must exist as a solid in molten steel. Taking this into account, our research focused on the melting point of oxides. It is generally known that, when the CaO content in an oxide reaches 40-60%, the melting point of the oxide becomes 1,413-1,600℃ and is minimized at the CaO content of 49%[9)]. Assuming the temperature of molten steel during casting to be 1,600℃, the region where the content of CaO becomes 40-60% coincides with the region where the melting point of the oxide becomes lower than the temperature of the molten steel. In other words, as the CaO concentration approaches 49% in this region, the oxide in the molten steel remains as a liquid at lower temperatures, lowering the crystallization temperature of TiN and shortening the time from the start of crystallization until the completion of the solidification of molten steel. This is considered to have suppressed the coarsening of TiN.

4. Verification of improvement in HAZ toughness

Based on the above, the effect of Ca addition on TiN particles is summarized as follows. From the aspects of the melting point of oxides, lattice misfit and critical nucleus formation energy, an increase in Ca addition not only suppresses the formation of coarse TiN, which becomes the origin of brittle fracture, but increases the fine TiN which contributes to the refinement of γ grain and the generation of intragranular α. All of these are considered to be effective in improving the HAZ toughness of ultra-high heat-input welds.

In order to verify this, the chemical compositions shown in Table 1 were modified such that they

have an additive amount of Al set at 0.03%. The steels were cast, rolled and subjected to the synthetic weld thermal cycle, as described previously; then Charpy tests were conducted to evaluate their HAZ toughness. The fracture surfaces of the specimens after the Charpy test were observed. Also observed were micro structures of the specimens etched by NITAL (an etching solution consisting of alcohol and nitric acid).

Fig. 7 shows the relationship between the amount of Ca added to the steel and the transition temperature at which fracture appears (*vTrs*). The increase in the amount of Ca has been verified to lower the *vTrs*, significantly improving the HAZ toughness of ultra-high heat input welds. The fracture surfaces of the Charpy test specimens clearly show that coarse TiN particles in steel without the Ca addition originate brittle fracture as shown in **Fig. 8**. Furthermore, the steel without Ca added exhibits coarse ferrite grains larger than 100 μm, as shown in **Fig. 9**, while the steel with Ca added exhibits a fine and homogeneous dispersion of ferrite with a grain size of around 20 μm, a result of the promotion of intragranular α generation. These results verify that the addition of Ca suppresses the formation of coarse TiN while increasing fine TiN, thus refining the microstructure in the HAZs of ultra-high heat input welds and improving their toughness.

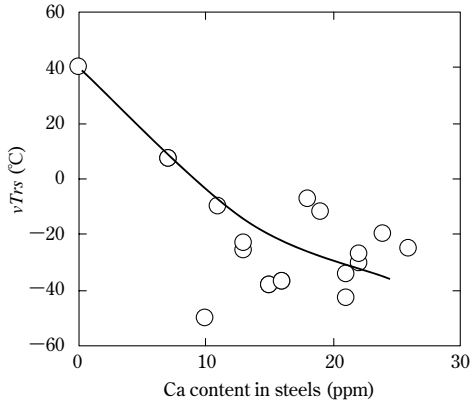

Fig. 7 Effect of Ca content on HAZ toughness

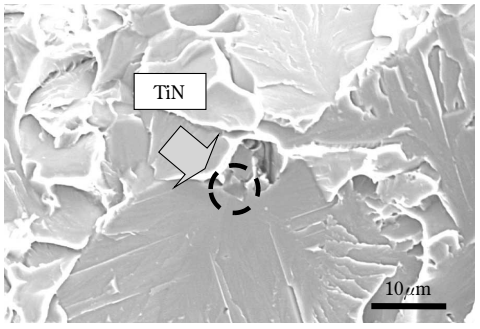

Fig. 8 Crystallized TiN at originating point of brittle fracture in Ca free steel

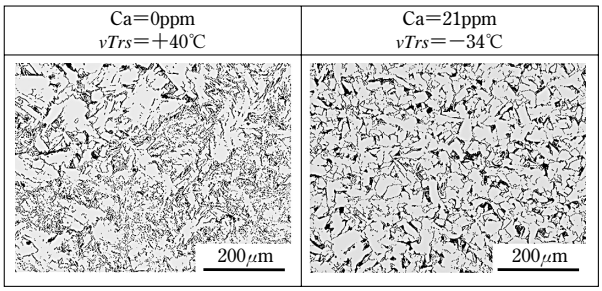

Fig. 9 Effect of Ca content on microstructure of HAZ

Conclusions

Kobe Super Toughness (KST), a process technique for finely dispersing TiN particles, was further improved by the addition of Ca. This technique is applicable to a wide variety of steel plates used in various fields including shipbuilding and construction, contributing not only to the improvement of welding efficiency, but also to the improvement of the safety of steel structures, and to the benefit of the entire society.

References

1) Y. KASAMATSU et al., *Tetsu-to-Hagane*, Vol.65, No.8 (1979), p.1222.
2) S. KITAMURA et al., *Tetsu-to-Hagane*, Vol.73, No.6 (1987), p.677.
3) S. SUZUKI et al., *JFE Technical Report*, No.5 (2004), p.19.
4) M. YAMAUCHI, *R&D KOBE STEEL ENGINEERING REPORTS*, Vol.50, No.3 (2000), p.16.
5) T. KATO et al., *Japan Welding Society Preprints of the National Meeting of JWS*, No.86 (2010), p.92.
6) Iron and Steel Institute of Japan, *Use of Fine Inclusions in Microstructure Control of Steels*, 1995, p.75.
7) Y. MORIKAGE et al., *Tetsu-to-Hagane*, Vol.84, No.7 (1998), p.510.
8) I. Jimbo et al., *Trans of the ISS*, 1989, p.43.
9) Verein Deutsher Eisenhuttenleute, *SLAG ATLAS 2nd Edition*, 1995, p.39.

Characteristics of Highly Formable 590-980MPa Grade Hot-dip Galvannealed Steel Sheets for Automobiles

Dr. Yuichi FUTAMURA*1, Masaaki MIURA*1, Michitaka TSUNEZAWA*2
*1 Sheet Products Development Department, Research & Development Laboratory, Iron & Steel Business
*2 Sheet Products Development Department, Research & Development Laboratory, Iron & Steel Business (currently with Sheet Products Marketing & Technical Service, Iron & Steel Business)

A series of 590-980MPa grade hot-dip galvannealed steel sheets has been developed in order to improve the formability of automotive body frame parts, such as lower pillars. These are either DP or TRIP-aided steel sheets, designed 1) to have homogeneous microstructures, 2) to inhibit the precipitation of carbide, 3) to maintain ferrite as much as possible, 4) to harden the ferrite to prevent degradation of local deformability, and in TRIP-aided steel sheet, additionally, 5) to obtain a large amount of retained austenite. The above microstructural controls are mainly accomplished by the addition of silicon, which can be adopted through a special surface preparation technology. The developed steel sheets have not only excellent formability, but also meet practical performance requirements, including good spot weldability and high coating.

Introduction

In recent years, high-strength steel sheets are more and more being used for automotive structural members to make auto bodies strong enough to meet increasingly stringent collision safety standards and light enough to meet the emission reduction requirements for environmental protection [1]. Among these sheets, galvannealed (hereinafter referred to as "GA") steel sheets are applied to parts that require corrosion resistance. In particular, high-strength GA steel sheets with excellent workability, are proactively adopted for lower parts of pillars and other structural members. With the recent increase in the number of parts employing high-strength steel sheets, the demand for further improved workability is growing [2, 3].

In response to these needs, Kobe Steel has developed a high tensile-strength GA steel, in the strength grade of 590 - 980MPa, which has an elongation 1.3 times higher than that of conventional materials [4]. This paper describes the concept of its microstructure control and major characteristics.

1. Concept of microstructure control

The developed materials include a dual-phase (DP) steel sheet, consisting of ferrite and martensite, and a transformation-induced plasticity (TRIP) aided steel sheet, consisting of ferrite, bainite and retained austenite. Both kinds of steel sheets ensure high ductility under the design concepts of ① homogenized microstructure, ② inhibited carbide precipitation, ③ the maximum amount of ductile ferrite, and ④ ferrite with its own strength increased by solid solution strengthening to prevent the deterioration of local deformability. In addition, ⑤ the TRIP-aided steel sheet is designed with its microstructure controlled so as to secure a large amount of retained austenite.

As a means for achieving the above objectives, the DP steel sheets adopt the technology developed by Kobe Steel for 590 - 980MPa grade GA steel sheets [5-12] and have compositions that largely suppress the bainite transformation during the cooling after annealing (②, ③). Furthermore, both the DP steel sheet and TRIP-aided steel sheet developed this time contain silicon (Si), an additive element playing an important role in stabilizing the ferrite and significant solid solution strengthening (③, ④). For some time, Si has been known to be effective in improving workability [13]; however, its application to GA steel sheet was difficult because the element tends to deteriorate coating quality. To resolve this issue, Kobe Steel developed a special surface modification which enabled GA steel sheet to contain above 1.0% of Si, as in the case of cold-rolled steel sheet, leading to this development.

The addition of Si can significantly increase elongation. On the other hand, Si addition facilitates the precipitation of ferrite in the microstructure during cooling, which decreases the yield ratio, leading to a significant reduction of yield strength for a given tensile strength. Thus, when producing a steel sheet containing Si, the microstructure is controlled while focusing on the recovery and recrystallization behaviors of the cold-rolled structure, in which the cold rolling reduction is optimized for each composition and for sheet thickness by adjusting the yield strength so as not to cause the deterioration of elongation during annealing. This control method offers a technique that is effective in obtaining a homogeneous composite structure regardless of sheet thickness (①). TRIP-aided steel sheets, on the other hand, adopt a microstructure control which maximizes the amount of retained austenite. Typically, a TRIP-aided steel sheet is austempered to increase carbon concentration in untransformed austenite. When producing a GA steel sheet, the steel sheet is exposed to an elevated

temperature in galvannealing treatment, which induces a phenomenon, unique to GA steel sheet, involving a structural change in which the austenite decomposes (precipitating carbide). The newly developed steel sheet contains retained austenite, whose amount is maximized by an optimized austempering (⑤). This new austempering includes galvannealing, unlike conventional austempering which simply condenses carbon.

Fig. 1 shows typical microstructures of the newly developed steel sheets: (a) DP steel sheet of 980MPa grade and (b) TRIP-aided steel sheet of 780MPa grade. Both the steel sheets contain large amounts of ferrite with no carbide precipitate observed. Furthermore, the DP steel sheet has a homogeneous and fine composite structure, while the TRIP-aided steel sheet is predominantly massive retained austenite with needle-like retained austenite (indicated by the arrows in the figure) between the laths of bainitic ferrite. **Fig. 2** shows the grain boundary distribution inside the 980MPa grade DP steel sheet obtained by a crystal orientation analysis based on an electron backscattering pattern (EBSP) measurement. In the grain boundary distribution diagram (Fig. 2 (b)), the black solid lines represent large angle grain boundaries with crystal misorientation of 15 degrees or larger, while the gray solid lines represent small angle grain boundaries with crystal misorientation smaller than 15 degrees. The figure indicates that the ferrite structure contains many small angle grain boundaries, which are remainders of a cold-rolled structure that has been annealed and is subgrained. The newly developed materials make use of such subgrain structures to adjust strength characteristics so as to achieve the high elongation described later. **Fig. 3** shows cross-sectional SEM micrographs of the newly developed 590MPa grade and 980MPa grade DP steel sheets, both having the quality of exhibiting homogeneous coating layers with favorable powdering resistance.

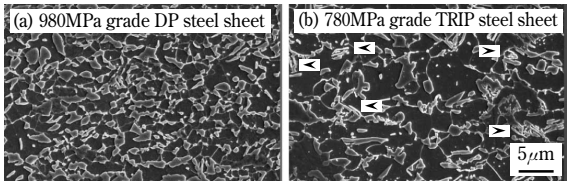

Fig. 1 SEM images of microstructure in developed steel sheets ((a)980MPa grade DP and (b)780MPa grade TRIP)

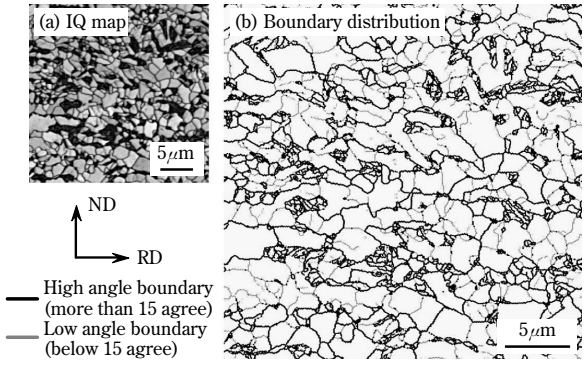

Fig. 2 Image Quality map (a) and Crystal orientation image map with boundary distribution (b) in developed 980MPa grade DP steel sheet

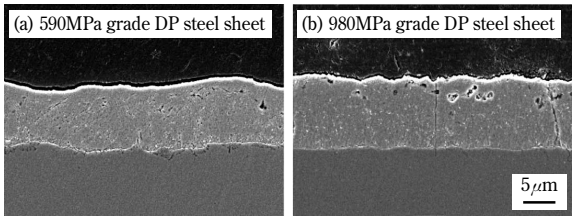

Fig. 3 SEM images of coating layer in developed steel sheets ((a)590MPa grade, (b)980MPa grade DP steel)

2. Main characteristics of newly developed materials

2.1 Formability

Table 1 summarizes the typical tensile properties of the newly developed materials (thickness 1.6mm). Also included in this table are the typical values of 590 - 980MPa grade cold-rolled steel sheets, in which the reference values of the 980MPa grade cold-rolled steel sheet are represented by those of a conventional Kobe Steel DP steel sheet that was developed for higher elongation[14]. All the newly developed materials exhibit elongations equivalent to those of the reference cold-rolled steel sheet in the same strength grade. **Fig. 4** compares the tensile strengths (*TSs*) and elongations (*ELs*) of the newly developed sheets of 980MPa grade DP steel and 780MPa grade TRIP-aided steel with those of the conventional materials. As the result of the composition design and microstructure control described previously, both of the newly developed sheets realize elongations up to 1.3 times greater than that of Kobe Steel's conventional materials. A

Table 1 Tensile properties of developed GA (Galvannealed) steel sheets and reference CR (Cold-Rolled) steel sheets

Steel	TS grade	Category	*YP* (MPa)	*TS* (MPa)	*EL* (%)
Galvannealed (GA) steel (Developed)	590MPa	Dual Phase	387	613	34
	780MPa	Dual Phase	481	828	23
		TRIP	478	823	29
	980MPa	Dual Phase	619	1,037	18
Cold-rolled (CR) steel	590MPa	Dual Phase	388	633	33
	780MPa	Dual Phase	509	838	22
	980MPa	Dual Phase	635	1,032	18

・Specimen thickness : 1.6mm
・Tensile test : JIS Z2241 (JIS Z2201 #5 specimen in Transverse direction)

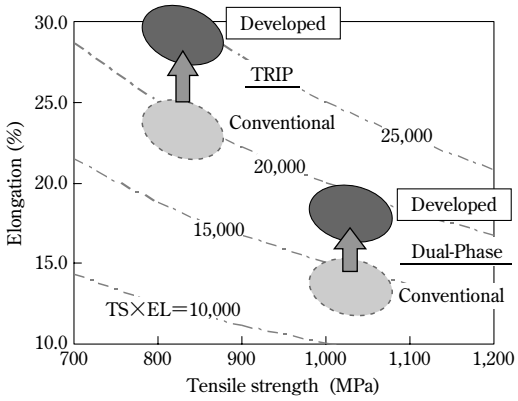

Fig. 4 Relationship between tensile strength and elongation in developed 980MPa grade DP and 780MPa grade TRIP steel sheets

stretch forming test confirmed that the TRIP-aided steel sheet exhibits extremely high strain dispersibility with less likelihood of local thickness reduction and achieves a limit-forming height comparable with that of a conventional 590MPa grade DP steel sheet which is one grade lower in terms of strength.

Table 2 shows the typical values of the hole expansion ratio (λ value), an index for stretch-flangeability, and the minimum bending radii in a 90 degree V-bending test. The minimum bending radius was determined from the smallest bending radius that causes no crack in a tested material bent by a 90 degree punch with a tip radius (R) of 0 - 5.0mm. The direction of bending was vertical to the direction of rolling. Also included in the table are the typical values for conventional 590 - 980MPa grade GA steel sheets. The newly developed materials have λ values that are all equivalent to those of the conventional materials in the same strength grade, with suppressed deterioration of local deformability, and as a result have superior balances of EL and λ compared with conventional materials. In general, bendability is known to correlate with stretch-flangeability as well as with local ductility [15), 16)]. Thus the minimum bending radius is regarded to correlate favorably with λ. The newly developed material, however, exhibits an excellent bendability despite its λ comparable to that of the conventional materials. This indicates that the bendability is not necessarily determined by λ. In other words, there may be effects other than the generally-known one of the addition of Si decreasing the difference in hardness between ferrite and martensite, improving the local deformability. However, the detailed mechanism has not been clarified yet, and a study is being conducted to elucidate the details. **Fig. 5** shows the forming limits for (a) the newly developed material of 590MPa grade and (b) 980MPa grade DP steel sheet (both having a thickness of 1.2mm). The scribed

Table 2 Hole expansion ratio and Minimum bending radius of developed and conventional steel sheets

Steel	TS grade	Category	Thickness (mm)	λ-value (%)	Minimum bending radius 〈Transverse direction〉
Developed steel	590MPa	Dual Phase	1.6	74	0.0
	780MPa	Dual Phase	1.6	27	0.0
		TRIP	1.4	29	0.0
	980MPa	Dual Phase	1.6	27	0.0
Conventional steel	590MPa	Dual Phase	1.6	68	0.0
	780MPa	Dual Phase	1.6	31	0.5
	980MPa	Dual Phase	1.6	25	2.0

・Stretch flanging (Hole expanding) test :
Hole expansion ratio : λ-value obtained by method of JFST1001
・Bending test : V-block method (90 degree angle) according to JIS Z2248 (JIS Z2203 #3 specimen in transverse direction)

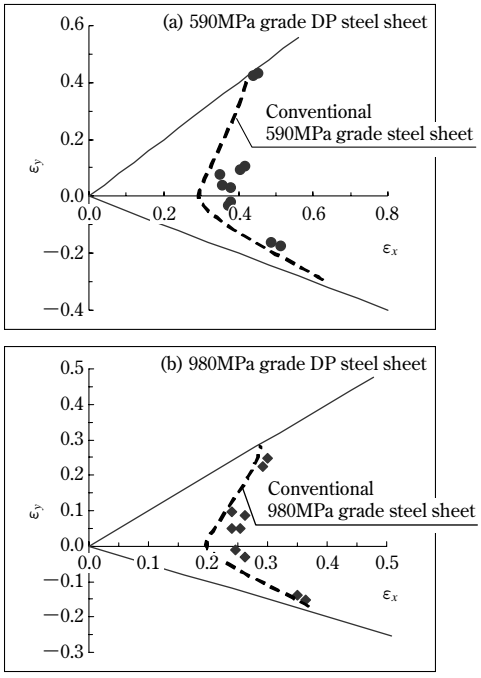

Fig. 5 Forming limit diagrams of developed steel sheets ((a)590MPa, (b)980MPa grade DP)

circle diameter is 0.25inch, and the dashed lines represent the forming limits for the conventional materials in the same strength grade for comparison. It has been shown that both of the newly developed materials have forming limits higher than those for conventional materials in a plane strain state, which is the most stringent forming condition. The high forming limit is attributable to the previously described composition design and microstructure control, both having an effect of improving elongation.

2.2 Spot weldability

Fig. 6 (a) and (b) respectively show the tensile shear strength (*TSS*) and cross tensile strength (*CTS*) of the 590MPa grade and 980MPa grade DP steel sheets, both newly developed, for varying welding

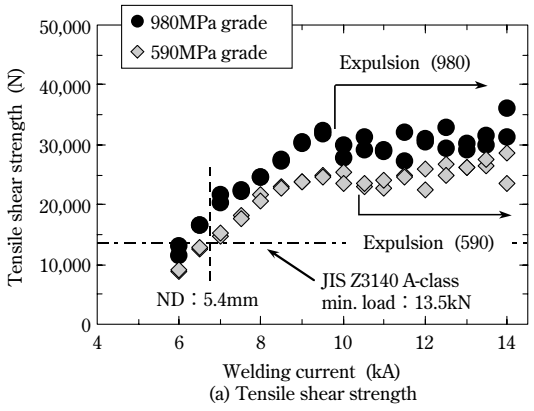

Fig. 6 Relationship between welding current and (a)tensile shear strength, (b)cross tensile strength in developed 590MPa and 980MPa grade DP steel sheets

current. Each sample sheet has a thickness of 1.6mm welded under the conditions shown in **Table 3**. Both the 590MPa grade and 980MPa grade steel sheets newly developed, have tensile shear strengths exceeding the requirement of JIS-A grade; i.e., 13.5kN, with a nugget diameter of 5.4mm. A suitable current range, not causing expulsion, is confirmed to be as large as 2.5kA or wider. On the other hand, cross tensile strength may decrease as an effect of the composition[17]. However, the newly developed materials exhibit no noticeable deterioration in strength. The newly developed materials of 590MPa grade and 980MPa grade result in a ductility ratio, the ratio between the tensile shear strength and cross tensile strength (*CTS/TSS*), of 0.65 or higher and 0.48 or higher, respectively, in the suitable welding current range. **Fig. 7** shows the relationship between the tensile shear strength and sheet thickness for a nugget of the newly developed 980MPa grade material that has a diameter of 5.4mm. For the thicker sheets, the electrode diameter and applied pressure were increased and the current period was extended. As a result, a favorable joint strength with a tensile shear strength greatly exceeding the load specified by JIS-A class was obtained.

Table 3 Spot welding conditions for Fig.6

Electrode tip	Dome type Cu-Cr
Tip diameter	8mm
Electrode force	4,950N
Welding time	28cycle (60Hz)
Welding current	6-14kA
Cooling water (Upper, Lower)	1.5L/min

Thickness	1.2mm	1.6mm	2.0mm
Tip diameter	6mm	8 mm	8mm
Electrode force	3,750N	4,950N	6,450N
Welding time (60Hz)	23 cycle	28 cycle	29 cycle

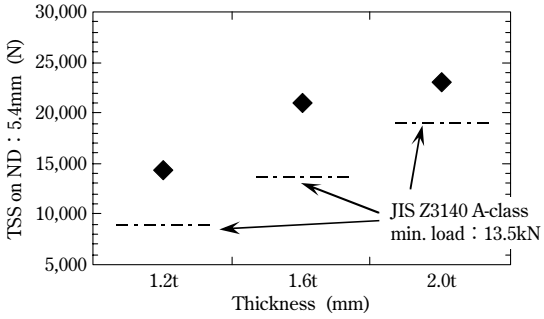

Fig. 7 Relationship between tensile shear strength and sheet thickness in developed 980MPa grade DP steel sheet

Table 4 Spot weldability in developed 590MPa and 980MPa grade DP steel sheets welded with/without gap (1mm) between sheets

TS grade (steel)	Gap between sheets	Welding current		
		ND:5.4mm	A-class TSS: 13.5kN	Expulsion
590MPa (Developed steel)	0mm	6.5kA	6.5kA	9.0kA
	1mm	6.5kA	6.5kA	9.0kA
980MPa (Developed steel)	0mm	6.0kA	5.5kA	8.0kA
	1mm	6.0kA	5.5kA	8.0kA

Table 4 summarizes the results of tests aimed at evaluating the practical spot weldability, in which the newly developed 590MPa grade and 980MPa grade materials were welded under the conditions of a smaller electrode tip diameter (6mm) and lower applied pressure (3,430N), compared with the conditions shown in Table 3. In addition, the welding was performed with or without a gap (1mm) in between the welded sheets. The table also includes the current values for the specified nugget diameter (5.4mm), JIS-A grade specification (13.5kN) and for expulsion. For all the cases, the electric current range in which both the specified nugget diameter and JIS-A grade specifications are satisfied without causing expulsion is above 1.5kA. This indicates that the newly developed materials not only have favorable workability, but also produce high welding joint strength in a consistent manner.

Conclusions

New galvannealed steel sheets of 590 - 980MPa grade with elongations as high as 1.3 times those of the conventional materials have been developed. The concepts of their microstructure control and main properties have been introduced. The newly developed materials are characterized not only by their excellent elongations, but also by superior bendability, spot weldability and coating quality, which are sufficient to satisfy customer needs. Kobe Steel regards these newly developed materials as a high-elongation type among the high-strength GA steel sheets. In response to customer needs, Kobe Steel has a lineup of products including, in addition to the above, steels with improved weldability and steels of high YS type. On the other hand, recent customer requirements for material properties have become much more stringent than they were several years ago, so Kobe Steel will continue striving to improve the characteristics of materials to resolve issues that the customers may have and thus expand the application of high-strength steel sheets.

References

1) Y. KURIYAMA et al., *Journal of Society of Automotive Engineering of Japan*, Vol.55, No.4 (2001), p.51.
2) S. KOBUKI, *TOYOTA Technical Review*, Vol.52, No.1 (2002), p.8.
3) K. SHIBATA, *NISSAN Technical Review*, No.50 (2002), p.26.
4) Y. FUTAMURA et al., *R&D Kobe Steel Engineering Reports*, Vol.57, No.1 (2007), p.109.
5) M. NAKAYA et al., *R&D Kobe Steel Engineering Reports*, Vol.50, No.1 (2000), p.75.
6) Y. OMIYA et al., *R&D Kobe Steel Engineering Reports*, Vol.52, No.3 (2002), p.10.
7) M. KAMURA et al., *R&D Kobe Steel Engineering Reports*, Vol.51, No.2 (2001), p.79.
8) M. KAMURA et al., *IBEC2002, Proceedings of the 2002 IBEC and ATT Conferences on CD-ROM*, (2002), 2001-01-3094.
9) M. KAMURA et al., *SAE Technical Paper* (2003), 2003-01-0522.
10) X. M. CHEN et al., *SAE Technical Paper* (2004), 2004-01-1048.
11) X. M. CHEN et al., *SAE Technical Paper* (2005), 2005-01-0354.
12) Y. FUTAMURA et al., *R&D Kobe Steel Engineering Reports*, Vol.57, No.2 (2007), p.11.
13) M. MIYAHARA et al., *R&D Kobe Steel Engineering Reports*, Vol.35, No.4 (1985), p.92.
14) T. TAMURA et al., R&D Kobe Steel Engineering Reports, Vol.52, No.3 (2002), p.6.
15) Y. TANAKA et al., *R&D Kobe Steel Engineering Reports*, Vol.42, No.1 (1992), p.20.
16) J. IWAYA et al., *JOURNAL OF THE JAPAN SOCIETY FOR TECHNOLOGY OF PLASTICITY SOSEI-TO-KAKO* (Journal of JSTP), Vol.35, No.404 (1994), p.1122.
17) S. NOMURA et al., *Technical Commission on Resistance Welding* (1981), RW-192-81.

Formability of TRIP Type Banitic Ferrite Steel Sheet

Takayuki KIMURA*1
*1 Process Engineering Development Department, Research & Development Laboratory, Iron & Steel Business

In recent years, cold rolled steel sheets of 980MPa grade have been increasingly used for automotive parts to improve collision safety (crashworthiness) and to reduce body weight. Kobe Steel has developed a new 980MPa cold rolled steel sheet with elongation properties that are an improvement over conventional dual-phase (DP) steel sheets. This article focuses on the press formability of the newly developed steel sheet. Press formability testing was performed using a small-sized model die and a large-sized actual part die. The result clearly indicates that the developed steel sheet has a significantly improved press formability when compared with conventional DP steel sheets.

Introduction

The latest automobiles are required to have both improved collision safety and weight reduction and make wide use of high-strength steel sheets. However, steel sheets with higher strength tend to have poor elongation characteristics and are more prone to crack during press forming. Therefore, some auto parts must be made in separate pieces for ease of forming. To resolve the issue, several methods have been proposed, including multiple process steps for improving deep-drawing formability[1] and dual punching to improve stretch flangeability[2]. So far as the materials are concerned, the steel sheets that have been developed are of high strength and superior formability. Kobe Steel has developed a cold-rolled, transformation-induced-plasticity (TRIP) type, banitic-ferrite steel sheet of 980MPa grade (hereinafter referred to as the "developed steel"), which is suitable for auto body frames, with elongation characteristics that are an improvement over those of conventional dual phase (hereinafter referred to as "DP") steel sheets[3), 4)].

This paper describes the features of the developed steel and reports the results of formability tests conducted using a small laboratory scale die and a large die simulating actual parts.

1. Microstructure and mechanical properties of developed material

1.1 Microstructure

Steel sheets with improved workability have been needed as the applications of high tensile strength steel of 980MPa grade increase. In response, Kobe Steel aims at improving elongation characteristics, while maintaining stretch-flangeability in comparison with the conventional 980MPa grade DP steel sheet of a type focusing on elongation (hereinafter referred to as "980DP steel"). **Fig. 1**[3] shows micrographs of the developed steel and 980DP steel. The developed steel contains a large amount of retained γ, which is morphologically controlled so as to be finely dispersed in elongated shapes to ensure elongation characteristics. The purpose of this is to increase the stability of retained γ such that the TRIP effect continues until the late stage of deformation.

1.2 Tensile properties

To evaluate the mechanical properties of the developed steel, tensile tests were conducted on specimens prepared according to JIS 5, using a 100kN autograph manufactured by Shimadzu Corporation. The cross-head speed was kept constant at 10mm/min. Comparisons were made with 980DP steel, as well as with 780MPa grade DP steel (hereinafter referred to as "780DP steel"). As shown in **Table 1**, the developed steel exhibits an elongation comparable to that of the 780DP steel and greatly exceeds that of the 980DP steel, implying its excellent formability. In addition, the developed

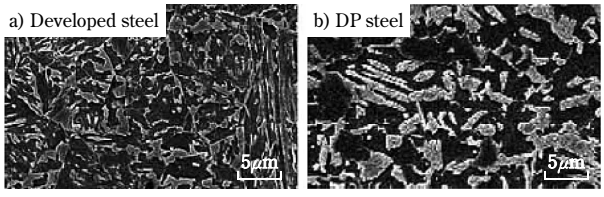

Fig. 1 Microstructure of 980MPa grade cold rolled steel sheets
a) developed steel, b) conventional DP steel[3]

Table 1 Mechanical properties of sample steels

(t : 1.4mm)

		YS (MPa)	*TS* (MPa)	*EL* (%)	*n* value 2-6%
a)	980 Developed steel	631	1,062	20	0.22
b)	980 DP steel	642	1,060	16	0.15
c)	780 DP steel	527	831	20	0.13

steel exhibits a n value (work hardening index) which is much higher than those of the reference steels, an indication of superior strain dispersibility. Thus, the developed steel advantageously suppresses the local reduction of thickness during press forming and is expected to enhance collision performance when used for parts in automobile body frames.

In order to verify the superior strain dispersibility of the developed steel, strain measurement using a non-contact strain measuring machine, ARGUS, manufactured by GOM mbH, was conducted in the longitudinal direction of the tensile specimens. A pattern of equally-spaced dots was provided on each specimen prior to the test. Each specimen was mounted on a tensile machine, elongated, and dismounted as soon as the strain reached 15%. After the deformation, the position relationships in the dot pattern were measured and the image was processed to evaluate the strain distribution. The measurement results, shown in **Fig. 2**, indicate that the developed steel exhibits less local strain concentration when compared with the reference steels, with the strain almost uniformly distributed within the specimen. The distributions in the thickness reduction rates of the specimens (**Fig. 3**) verify that local strain concentration is suppressed for the developed steel.

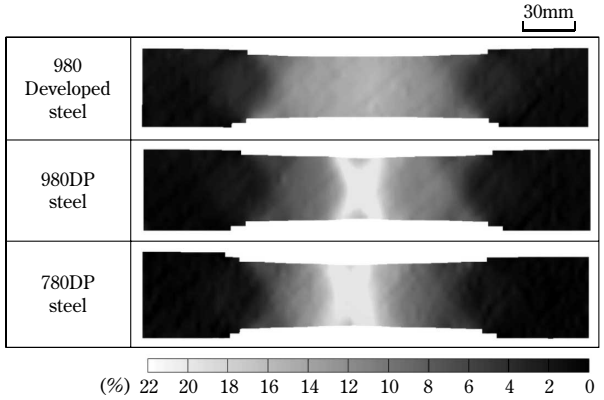

Fig. 2 Longitudinal strain distribution of tensile test specimen (strain：15%)

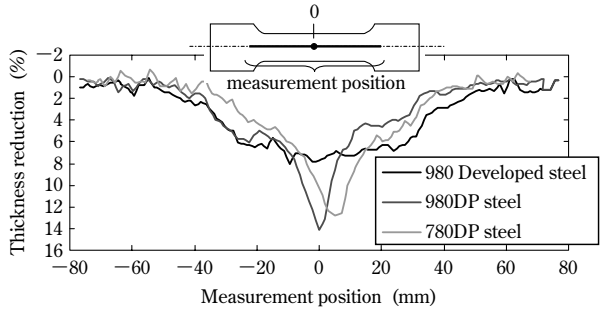

Fig. 3 Distribution of thickness reduction rate in tensile test specimen (strain：15%)

2. Formability of developed steel

The developed steel sheet was studied for its formability in terms of the four major forming modes of stretching, deep drawing, stretch flanging and bending. The thickness of the tested materials was 1.4mm.

2.1 Stretch formability

Fig. 4 depicts the testing apparatus. The stretch formability was evaluated by the maximum forming height, which is determined by the punch stroke, which causes failure with a rapid load drop in the load-stroke diagram. As a reference, the 980DP steel was also tested. The testing apparatus was a 500kN universal deep-drawing tester manufactured by TAKES-GROUP Ltd.

The maximum forming heights shown in **Fig. 5** verify that the developed steel has a formability superior to that of the 980DP steel. This result is as expected from the results of the tensile tests. The stretchability is reported to be affected by the elongation and n values of materials[5].

As in the case of the tensile test, the strain dispersion effect in the stretch formed samples was studied. Thickness reductions were measured on the developed steel and 980DP steel, both formed to a height of 17mm. As shown in **Fig. 6**, the thickness reduction rate for the developed steel is less than 30% even near the top where the reduction reaches the maximum. On the other hand, the 980DP steel exhibits a thickness reduction of about 35% for the same forming height, verifying the superior strain dispersibility of the developed steel in the stretching test.

Punch：ϕ50mm, r_p=25mm
Die：ϕ54.8mm, r_d=10mm
Lubricant：NOX-RUST 530
Blank holding force：118kN
Blank size：150×150mm

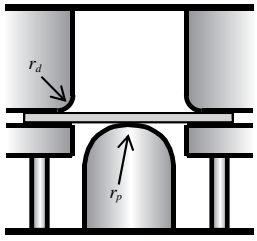

Fig. 4 Experimental apparatus for stretch formability

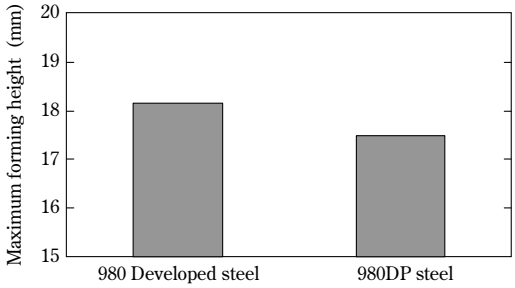

Fig. 5 Maximum forming height

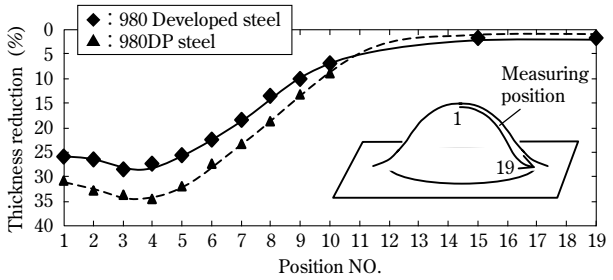

Fig. 6 Thickness reduction rate distribution of stretch test specimen (Forming height：17mm)

2.2 Deep drawing formability

Deep drawing tests were conducted using a punch having a spherical head with a head diameter of 50mm (**Fig. 7**). The maximum forming height at a drawing ratio of 2.0 was used as the evaluation index. The maximum forming height was determined by the punch stroke, which causes failure with a rapid load drop in the load-stroke diagram, just as in the case of the stretch formability test. Both the 980DP steel and 780DP steel were tested as reference materials. The tests were conducted using a 500kN universal deep-drawing tester manufactured by TAKES-GROUP. Ltd.

As shown in **Fig. 8**, the developed steel exhibits the best formability among the three types of steel tested. The difference can easily be seen in the photos of the formed samples (**Fig. 9**). The developed steel exhibits the highest total elongation and *n* value, the combined effect of which is considered to have led to its superior formability. As described above, the developed steel contains retained γ, which is considered to assure excellent strain dispersibility and to increase the strength at the punch shoulder portion by strain-induced transformation as well[6]. In other words, the excellent strain dispersibility is considered to allow the developed steel to have a larger thickness near the vertex in comparison with the DP steel. In addition, the greater strength increased by work hardening is considered to have enabled the developed steel to endure great resistance against the material flow into the flange. Another reason for the excellent formability is that, unlike conventional retained γ steel, the developed steel has finely dispersed retained γ in elongated shapes, such that work hardening continues until the late stage of the deformation. As for resistance against the material flow into the flange, the volume expansion associated with the strain-induced transformation of retained γ suppresses the transformation under the compressive stress generated by the drawn material. Furthermore, the strength increment due to work hardening, which is smaller than in the case of DP

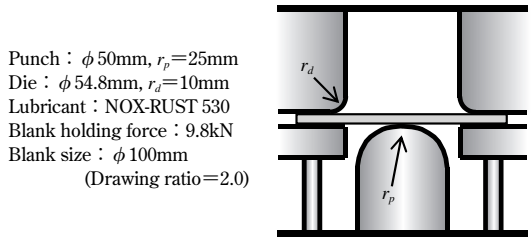

Fig. 7 Experimental apparatus for drawing formability

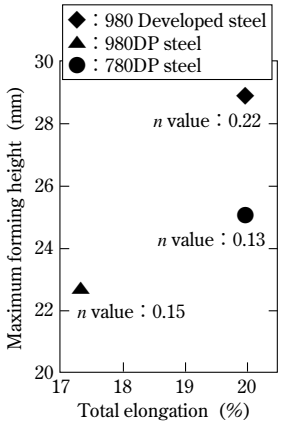

Fig. 8 Maximum forming height (Draw)

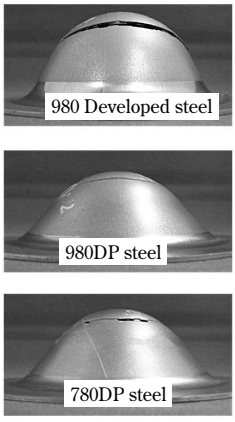

Fig. 9 Drawing test specimen

steel, decreases the flow resistance and contributes to the improved deep drawability of the developed steel.

2.3 Stretch flangeability

The stretch flangeability was evaluated by a hole-expanding test. The test was conducted according to the Japan Iron and Steel Federation Standard, JFST1001. The stretch flangeability of the developed steel is almost equal to that of the 980DP steel, as shown in **Fig.10**. In general, the stretchability and stretch-flangeability of a high-strength steel sheet are in a trade-off relationship. In other words, steel sheet having a superior stretchability tends to have poor stretch-flangeability and vice versa. The reason for the suppressed degradation of stretch-flangeability, despite the superior stretchability, compared with the 980DP steel, is that the developed steel has a fine and homogeneous microstructure that suppresses local cracking.

2.4 Bending formability

Bending formability is evaluated by the existence/nonexistence of a crack on the outer surface of a sample bent by V bending with a punch with a punch angle of 90 degrees. The punch tip radius, *R*, was varied from large to small. In this V bending test, each sample was placed such that the

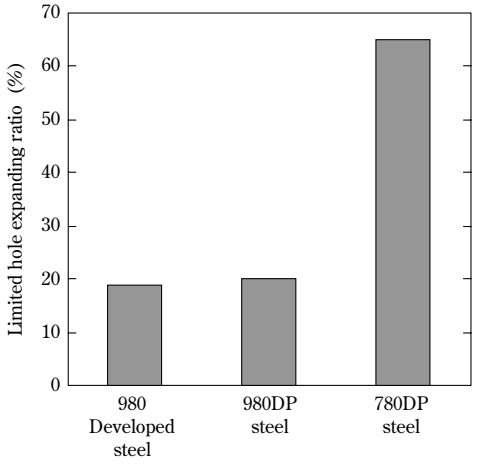

Fig.10 Limited hole expanding ratio of steels

Table 2 Bendability of steels

	90°V		
	R=0mm	R=0.5mm	R=1.0mm
980 Developed steel	△○	○○	○○
980DP steel	△△	○○	○○

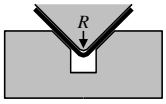

○ : Good △ : Hair crack

rolling direction was parallel to the bending ridge line, and the punch was forced until the applied pressure reached 19.6kN. The test results are summarized in **Table 2**. They confirm that the developed steel has a bending formability almost equivalent to that of the 980DP steel. The developed steel sheet can be bent to the point where it is substantially U-shaped, which is considered to satisfy the bending workability required for body frame parts.

2.5 Formability evaluation using die simulating front pillar

As described above, the developed steel is superior in formability to the conventional type of DP steel sheet in all three of the aspects of stretchability, deep-drawability and bendability. Its stretch-flangeability has been confirmed as almost equal to that of the 980DP steel. To demonstrate the superior formability of the developed steel, an evaluation was conducted using a large-sized die simulating an actual part.

Kobe Steel once evaluated the formability of the developed steel using a die to simulate a B-pillar and confirmed the superiority of the developed steel[3]. The evaluation at that time, however, focused on the formability of deformation elements including only stretching and deep drawing, rather than the formability of an entire part, lacking the deformation element of stretch flanging; so this time the evaluation was conducted based on an A-pillar, which contains the deformation element of stretch flanging. A simulation die was used for evaluating the overall formability of the entire part.

Fig.11 is a photo showing the formed part. The A-pillars, currently in volume production, use steel sheets of either 440MPa grade or 590MPa grade steel sheets, and only a few employ the 980MPa grade. In many cases, this component is constructed in separate blocks, in which the pocket shape in the lower part of the vehicle is separated to avoid cracking during the press forming. The evaluation this time, on the other hand, was conducted by forming the part as a single piece without splitting. As shown in Fig.11, the press-formed shape requires a superb deep-drawability and stretchability, as well as a superior stretch-flangeability at the blank holder portion. As a reference, 980DP steel was also press-formed. The sheet thickness in either case was 1.4mm.

The blank holder force was varied from 800kN to 2,000kN, while checking for the existence/nonexistence of cracks and wrinkles. As shown in **Table 3**, the 980DP steel could be formed up to 1,300kN without cracking; however, wrinkling occurred in the seat surface facing the upper surface of the punch. These wrinkles, occurring inside the part, can be suppressed by increasing the blank holder force. The arrow in the table indicates the direction along which the wrinkle suppression

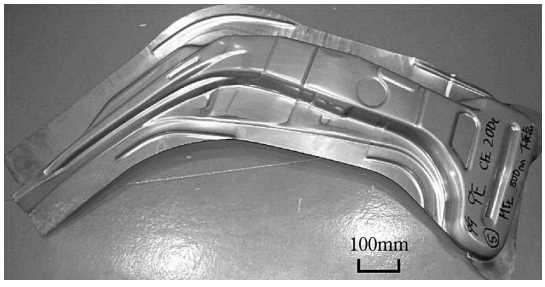

Fig.11 Shape of press test part

Table 3 Results of press test

BHF (blank holding force)	fracture		wrinkle
	980 Developed steel	980DP steel	
800kN	○	○	NG
1,000kN	○	○	
1,200kN	○	○	
1,300kN	○	○	
1,400kN	○	×	
1,500kN	○	×	
1,700kN	○	×	
2,000kN	○	×	Good

○ : Good × : fracture

becomes more advantageous. **Fig.12** shows an example of the wrinkles. A blank holder force greater than 1,400kN resulted in cracking in the stretch flange portion, as shown in **Fig.13**. The developed steel, on the other hand, was formable without causing any cracking up to the equipment capacity limit, a blank holder force of 2,000kN. Thus the developed steel can be used for increasing the strength of parts and for the reduction of production cost by single-piece forming. Furthermore, its excellent formability can be exploited to allow the product design of parts having deeper cross-sections and to improve collision performance.

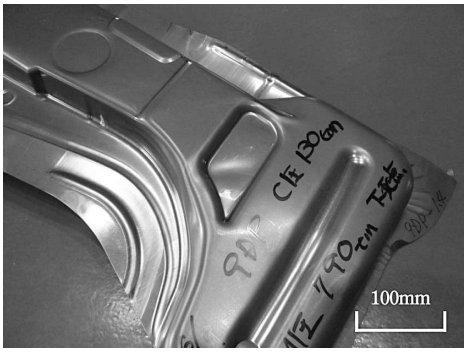

Fig.12 Example of wrinkle in test part (BHF=1,300kN 980DP steel)

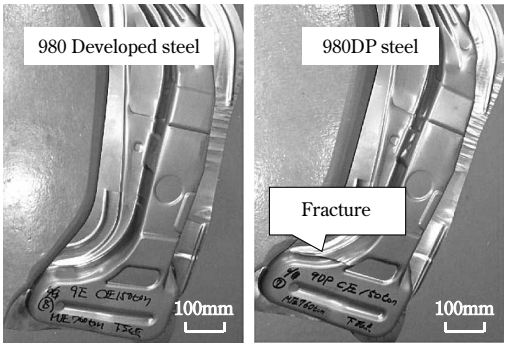

Fig.13 Example of press result (BHF=1,500kN)

Conclusions

A TRIP type, bainitic ferrite, 980MPa grade cold-rolled steel sheet with superior formability was introduced. This sheet has improved elongation characteristics, compared with conventional type DP steel.

The developed steel is superior in elongation characteristics and strain dispersibility compared with the conventional type DP steel and can be applied to body frame parts (forming).

A formability evaluation, using a small laboratory scale die, has confirmed that the developed steel has a formability exceeding that of conventional type DP steel in all the terms of stretching, deep-drawing and bending. It also exhibits a stretch-flangeability almost equal to that of the conventional material.

Dies for large, actual-size parts simulating a B-pillar and A-pillar were used to evaluate the formability of the developed steel. The results confirm that the developed steel has a formability that substantially exceeds that of conventional type DP steel. The developed steel can reduce costs by enabling the single-piece forming of parts which otherwise had been difficult to form and can increase the degree of freedom in improving collision performance.

References

1) J. IWAYA et al., *The Proceeding of The 36th Japanese Joint Conference for the Technology of Plasticity*, (1985), p.309.
2) J. IWAYA et al., *R&D KOBE STEEL ENGINEERING REPORTS*, Vol.47, No.2 (1997), P.33.
3) M. NAKAYA et al., *R&D KOBE STEEL ENGINEERING REPORTS*, Vol.59, No.1 (2009), P.46.
4) M. HAKAYA et al., *R&D KOBE STEEL ENGINEERING REPORTS*, Vol.57, No.2 (2007), P.19.
5) Japan Sheet Metal Forming Research Group, *Press Forming Difficulty Handbook* (in Japanese), Nikkan Kogyo Shimbun Ltd., 2007, p.78.
6) O. MATSUMURA, *Tetsu-to-Hagane*, Vol.79, No.2 (1993), p.209

Integrated Application Method for KOBEHONETSU™ Steel Sheet

Dr. Yasuo HIRANO*1, Tetsuya IGARASHI*1, Haruyuki MATSUDA*2, Makoto NISHIMURA*2
*1 Sheet Products Development Department, Research & Development Laboratory, Iron & Steel Business
*2 Mechanical Engineering Research Laboratory, Technical Development Group

KOBEHONETSU is the trade name for a steel sheet having heat-radiation ability. A method was developed for applying this steel sheet to dissipate heat in high-performance electronic equipment. By applying KOBEHONETSU to both the heat sink and housing simultaneously, the amount of heat transferred out of an electronic device was significantly increased to a level comparable with that achieved by a cooling fan. This cooling effect is enhanced by increasing the heat sink area, which makes KOBEHONETSU more applicable to heat sources such as CPUs. For example, this steel sheet can be machined into heat sinks, while maintaining its area and heat dissipation capability, for cases where heat sinks may interfere with other parts.

Introduction

An increasing number of home electronic and office automation products have become digitally operated. In the digital circuits of these products, most semiconductor devices work as on/off switches. The on/off action of these semiconductor devices consumes electrical energy, but the greater part of the energy supplied escapes as heat. Higher-speed semiconductor devices consume more power, increasing the amount of heat generated and raising the temperature. In other words, improving the performance of a digital instrument is inevitably associated with an increased amount of heat being generated and a rise in temperature.

A rise in the internal temperature of an instrument can cause its semiconductor devices to malfunction, cause the characteristics of its elements, such as resistors, to change, and shorten the overall life of electronic components containing organic insulation. To resolve these issues, heat dissipation technologies have been developed for efficiently inducing the heat generated inside an instrument to move away from the heat source and exit the instrument. The heat dissipation employs various techniques such as heat sinks and fans.

As a manufacturer of steel sheets for the covers and chassis of home electronic appliances and office automation equipment, Kobe Steel supplies KOBEHONETSU, a steel sheet having heat radiation ability[1]. KOBEHONETSU is widely used as steel sheet with increased thermal emission from its surface. When used for the cover of a home electronic appliance or of an office automation apparatus, for example, it efficiently dissipates the internal heat to the outside by radiation heat transfer and lowers the internal temperature of the instrument.

The efficiency of radiation heat transfer is proportional to the fourth power of the absolute temperature. Therefore, the higher the internal temperature of an instrument, the higher the heat radiation efficiency. On the other hand, heat radiation works less efficiently when the ambient temperature is low and the difference between the ambient and internal temperatures is small.

This paper introduces a method of achieving a heat radiation effect comparable to that of a cooling fan, even when the ambient temperature is low and the difference between the ambient and internal temperatures is small.

1. Principle of heat radiation structure

The amount of heat transferred by thermal radiation is considered using a semi-cylinder model consisting of a gray body having a heating element, an enclosure and an outer space, which are located in that order from inside out (**Fig. 1**)[1]. In the figure, the symbols ①, ②, ③ and ④ represent the heat radiation surface of the heating element, the inner surface of the enclosure, the outer surface of the enclosure and the surface facing the outer space, respectively. Their surface areas are represented by A_1, A_2, A_3 and A_4, while their emissivities are represented by ε_1, ε_2, ε_3 and ε_4, respectively. The surface temperature of the heating element is denoted by T_1, the inner surface temperature of the enclosure by T_2, the outer surface temperature of the

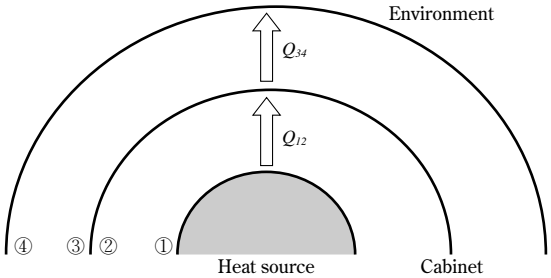

Fig. 1 Calculation model for thermal radiation transfer

enclosure by T_3, and the temperature at the wall surface facing the outer space by T_4. Ignoring the heat transfer by thermal conduction and convection, the radiation amount Q_{12} (W) from the heating element to the enclosure is given by equation (1).

$$Q_{12}=\frac{A_1\sigma(T_1^4-T_2^4)}{\frac{1}{\varepsilon_1}+\frac{A_1}{A_2}(\frac{1}{\varepsilon_2}-1)} \quad \cdots\cdots(1)$$

On the other hand, the amount of radiation Q_{34} (W) from the enclosure to the outer space is given by

$$Q_{34}=\frac{A_3\sigma(T_3^4-T_4^4)}{\frac{1}{\varepsilon_3}+\frac{A_3}{A_4}(\frac{1}{\varepsilon_4}-1)} \quad \cdots\cdots(2)$$

where σ is the Stefan-Boltzmann constant having a value of $5.667\times10^{-8}(W/m^2K^4)$. Assuming that T_2 is equal to T_3 in equation (1) and equation (2), T_1 is given as follows:

$$T_1=\left[T_4^4+\frac{Q_{12}}{A_1\sigma}\left\{\frac{1}{\varepsilon_1}+\frac{A_1}{A_2}(\frac{1}{\varepsilon_2}-1)\right\}+\frac{Q_{34}}{A_3\sigma}\left\{\frac{1}{\varepsilon_3}+\frac{A_3}{A_4}(\frac{1}{\varepsilon_4}-1)\right\}\right]^{\frac{1}{4}} \quad \cdots\cdots(3)$$

equation (3) was used to study the effect on heating element temperature caused by the surface area of the heating element and the emissivity of the enclosure (**Table 1**). Here the following assumptions were made, i.e., the amount of heat generated is 0.3W and the wall surface facing the outer space has an area of $100m^2$, an emissivity of 0.99 and a temperature of 25℃. Case 1 assumes that the enclosure is made of an electrogalvanized steel sheet. The heating element temperature for this case is calculated to be 79℃. Case 2 assumes that the enclosure is made of KOBEHONETSU. The heating element temperature for this case is calculated to be 74℃. Case 3 assumes that the heating element has an emissivity equal to that of KOBEHONETSU and has twice as much surface area. This case also assumes that the enclosure is made of KOBEHONETSU. In Case 3, the temperature of the heating element is lowered to 53℃. Case 4 assumes that the heating element has a surface area three times larger. The heating element temperature for this case is lowered to 44℃.

These results indicate that the temperature can be lowered significantly by increasing the emissivity, as well as the surface area, of the heating element and by increasing the emissivity of the enclosure. The following introduces the demonstration of these analysis results.

Table 1 Influences of surface area and emissivity of heating element and emissivity of housing on temperature of heating element

Case	A_1 (cm^2)	$A_2=A_3$ (cm^2)	ε_1	$\varepsilon_2=\varepsilon_3$	$Q_{12}=Q_{34}$ (W)	T_1 (℃)
1	10	1,200	0.8	0.1	0.3	79
2	10		0.8	0.86		74
3	20		0.86	0.86		53
4	30		0.86	0.86		44

2. Experimental verification of heat radiation structure

An apparatus, shown in **Fig. 2**, was made for experimentally verifying the calculation results obtained in the previous section. The enclosure, having an opening at the front, was made of an electrogalvanized steel sheet and had a dimension of 300mm(W)×88mm(D)×250mm(H). Vent holes, each sized 100mm×30mm, were provided at the top and bottom to allow cooling by natural convection, the cooling method commonly employed by actual instruments. A ceramic heater (1.8W), sized 25×25×2mm, mounted on an electronic board, was provided on the surface at the far end of the enclosure. This apparatus was used to compare the temperatures of the ceramic heater in the following four cases:

1) The opening at the front was closed with an electrogalvanized steel sheet (**Fig. 3** (a))
2) The opening at the front was closed with a KOBEHONETSU sheet (Fig. 3 (b))
3) The opening at the front was closed with an electrogalvanized steel sheet with a fan provided at the center of the sheet so as to cool the ceramic heater directly (Fig. 3 (c)) and

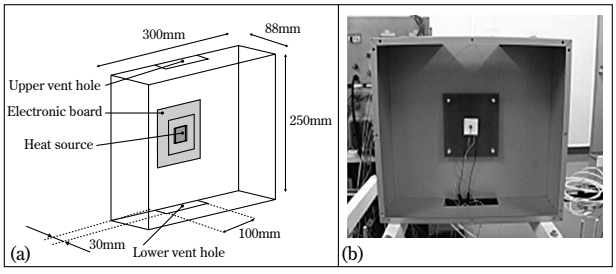

Fig. 2 Experimental apparatus for heat radiation structure

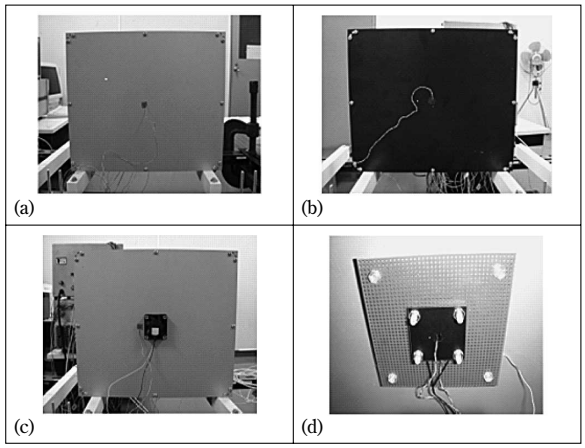

Fig. 3 Cooling method of heat source

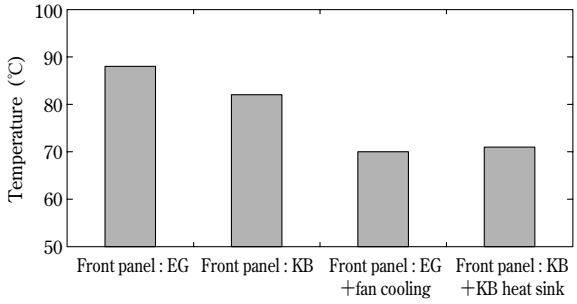

Fig. 4 Effects of heat radiation structure
(EG : Electrogalvanized steel sheet, KB : kobehonetsu)

4) The opening at the front was closed with a KOBEHONETSU sheet, while the ceramic heater was covered by a heat sink (40×40mm) made of KOBEHONETSU (Fig. 3 (d))

As shown in **Fig. 4**, the results indicate that the ceramic heater covered with a KOBEHONETSU sheet exhibited a heat dissipation comparable to that of the cooling fan.

3. Method for effectively utilizing heat radiation structure

As reported in the previous section, a ceramic heater, sized 25×25mm, covered by a piece of KOBEHONETSU, 40×40mm, realizes a temperature reduction of 17℃. The results shown in Table 1 also suggest that increasing the size of the KOBEHONETSU sheet placed on the heater should lower the temperature even further. To verify this and to establish a guideline for the size of a KOBEHONETSU heat sink that will achieve the desired temperature, an analysis was conducted according to the simulation model shown in **Fig. 5**. The results are shown in **Fig. 6**. The heat source temperature decreases with the increasing area of a KOBEHONETSU heat sink. This suggests that the heat sink area can be set up according to the target temperature.

There may be cases where the heat sink area cannot be set up in a desired size, due to other components located near the heat source (**Fig. 7**). In such cases, the heat sink can be adapted to avoid interference with neighboring components. Several examples are shown in **Fig. 8**, and the results of the corresponding temperature calculations are shown in **Table 2**. The heat source temperature can be decreased by increasing the heat sink area, while avoiding interference with neighboring components, as shown by Case (c) and Case (d). Even in a case where a vertical surface exists in the heat source, as in Case (d), a KOBEHONETSU heat sink is effective in lowering the temperature.

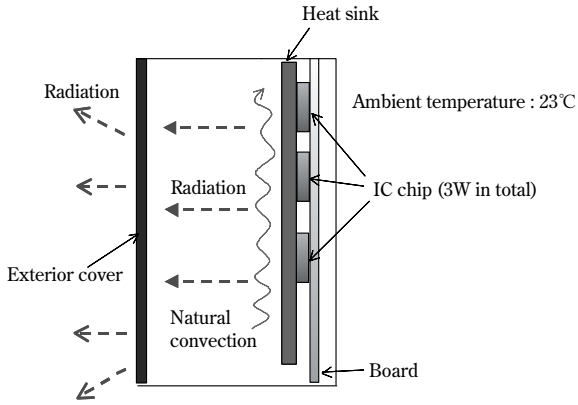

Fig. 5 Simulation model for heat radiation structure

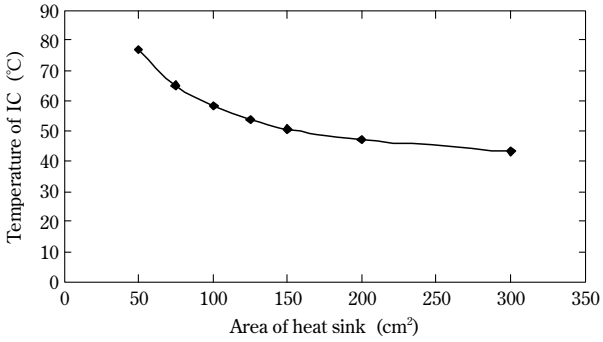

Fig. 6 Effects of heat sink area on heat source temperature

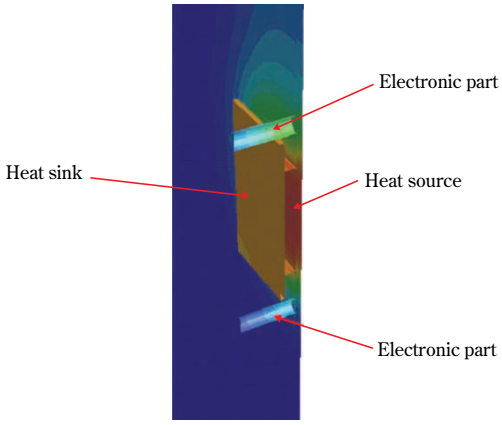

Fig. 7 Constraints on heat sink due to other electronic components

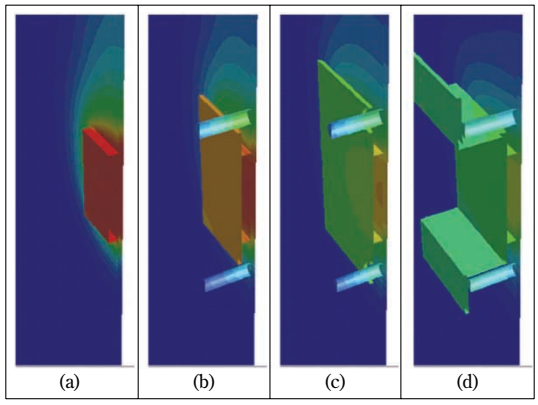

Fig. 8 Cases of setting up heat sink in case of parts close to heat source

Table 2 Temperature reduction by setting up heat sink in case of parts close to heat source

Case	Area of heat sink (cm^2)	Temperature of heat source (℃)
(a)	None	103
(b)	9	79
(c)	16	68
(d)	20	62

Conclusions

The interior temperatures of electronic instruments have come close to the heat resistance limit of arithmetic elements such as CPUs. The life of the precision components is in question. KOBEHONETSU offers a method for lowering the internal temperature of electronic instruments without decreasing the air-tightness of the apparatus. KOBEHONETSU can be used not only for covers, but also for heat sinks, the combination of which decreases the temperature of the heating elements even further, allowing the use of cooling fans with smaller capacities, or even their elimination, which leads to cost reduction. KOBEHONETSU is expected to further contribute to the improvement of instrumental performance, in terms of performance upgrading, downsizing, energy saving and noise reduction.

References

1) Y. HIRANO et al., *R&D KOBE STEEL ENGINEERING REPORTS*, Vol.54, No.1 (2004), p.58.